EXPERIMENTAL INVESTIGATION OF FLOW SEPARATION FROM RIGID WALLS WITH SALIENT EDGES

A THESIS SUBMITTED TO
THE GRADUATE SCHOOL OF NATURAL AND APPLIED SCIENCES
OF
THE MIDDLE EAST TECHNICAL UNIVERSITY

BY

FİKRİ AKÇALI

IN PARTIAL FULFILLMENT OF THE REQUIREMENTS FOR THE DEGREE OF
MASTER OF SCIENCE
IN
THE DEPARTMENT OF AEROSPACE ENGINEERING

JANUARY 2004

Approval of the Graduate School of Natural and Applied Sciences.

Prof. Dr. Canan Özgen
Director

I certify that this thesis satisfies all the requirements as a thesis for the degree of Master of Science.

Prof. Dr. Nafiz Alemdaroğlu
Head of Department

This is to certify that we have read this thesis and that in our opinion it is fully adequate, in scope and quality, as a thesis for the degree of Master of Science.

Assoc. Prof. Dr. Andreas Spohn
Co-Supervisor

Prof. Dr. Nafiz Alemdaroğlu
Supervisor

Examining Committee Members

Prof. Dr. Nafiz Alemdaroğlu

Prof. Dr. Kahraman Albayrak

Assoc. Prof. Dr. Serkan Özgen

Assoc. Prof. Dr. Yusuf Özyörük

Assoc. Prof. Dr. Andreas Spohn

ABSTRACT

EXPERIMENTAL INVESTIGATION OF FLOW SEPARATION FROM RIGID WALLS WITH SALIENT EDGES

AKÇALI, Fikri

M. S., Department of Aerospace Engineering

Supervisor: Prof. Dr. Nafiz ALEMDAROĞLU
Co-Supervisor: Assoc. Prof. Dr. Andreas SPOHN

January 2004, 144 pages

This thesis presents the experimental results on the formation of flow separation from a rigid wall with a salient edge. In the case of automotive vehicles or aircrafts with rear cargo compartment doors, such salient edges are at the origin of separated wake flows resulting in increased drag and other disturbing effects. Recent studies of Ahmed et al. (1984) on simplified geometries showed the strong influence of the slant angle on the flow separations. In this study, the geometry is further simplified to examine the flow separation under two-dimensional conditions. The experimental configuration consists of a fixed horizontal front panel and an attached rear panel with variable slant angle. The experiments were carried out in a low speed water channel to analyze the flow structure by flow visualization techniques. The hydrogen bubble technique and PIV measurements are used to obtain both qualitative and quantitative information on the flow structure. The electrolytic precipitation technique is used to analyze the flow separation in more detail. The slant angle varied between 0 and 35 degrees while the Reynolds numbers of the model was fixed to 24800 and 50500. As a function of slant angle and Reynolds number, two different types of flow separation were observed: boundary layer separation due to adverse pressure gradient and the so called "inertial

separation" at the edge singularity. Future strategies to control the formation of the wake flow highly depend on the very different flow structure of these two types of separation.

Keywords: Car Aerodynamics, Ahmed Body, Flow Separation, Water Channel Measurements, Hydrogen Bubbles, Electrolytic Precipitation, PIV

ÖZ

BELİRGİN KENARLI KATI DUVARLAR ÜZERİNDEKİ AKIM AYRILMASININ DENEYSEL OLARAK İNCELENMESİ

AKÇALI, Fikri

Yüksek Lisans, Havacılık ve Uzay Mühendisliği

Tez Yöneticisi: Prof. Dr. Nafiz ALEMDAROĞLU
Ortak Tez Yöneticisi: Doç. Dr. Andreas SPOHN

Ocak 2004, 144 sayfa

Bu tez, eğimli katı bir duvar üzerindeki akım ayrılmasının oluşmasını deneysel olarak incelemekte ve sonuçlarını sunmaktadır. Otomotiv araçlarında ve kargo kapakları arkada bulunan uçaklarda bu tür eğimli yüzeylere rastlanmaktadır. Bu yüzeyler nedeniyle, söz konusu cisimler üzerinde sürüklenme kuvvetleri artmaktadır. Ahmed ve ekibi, 1984 yılından bu yana basitleştirilmiş otomotiv şekilleri üzerinde çalışmaktadırlar. Özellikle arka tarafta bulunan eğimin, akım ayrılmasına büyük etkisi olduğunu göstermişlerdir. Bu çalışmada, akım ayrılmasını iki boyutlu koşullarda inceleyebilmek için, söz konusu şekil daha da basitleştirilmiştir. Deneysel konfigürasyon sabit, yatay bir ön panel ve bunun arkasına eklenmiş olan eğim açısı değişebilen bir arka panelden oluşmaktadır. Deneyler, akım yapısını, akım görüntüleme teknikleriyle analiz edebilmek için düşük hıza sahip bir su tünelinde yapılmıştır. Hidrojen baloncukları görüntüleme tekniği ve PIV ölçümleri ile akım yapısının niteliği ve niceliği hakkında bilgiler toplanmıştır. Akım ayrılmasını daha ayrıntılı inceleyebilmek için elektrolitik çökertme tekniği kullanılmıştır. Deneyler, 24800 ve 50500 Reynolds sayılarında, 0 ila 35 derece arasında değişen eğim açılarında yapılmıştır. Eğim açısının ve Reynolds sayısının fonksiyonu olarak iki çeşit akım ayrılması gözlenmiştir. Bunlardan ilki artan basınçtan kaynaklanan sınır tabaka

ayrılması ile oluşan akım kopması, diğeri ise belirgin kenardan kaynaklanan ve “eylemsizlik ayrılması” olarak tanımlanan akım ayrılmasıdır. Akım ayrılmalarının kontrolü için ileride geliştirilecek olan stratejilerin bu iki farklı ayrılmanın niteliklerine bağlı olacağı öngörülmektedir.

Anahtar Kelimeler: Araba Aerodinamiği, Ahmed Şekli, Akım Ayrılması, Su kanalı ölçümleri, Hidrojen Balonu, Elektrolitik Tortulaşma, PIV

To My Dear Father

ACKNOWLEDGEMENTS

This thesis is the result of a joint study between *Aerospace Engineering Department* of *Middle East Technical University* and Aerodynamic Studies Laboratories (*Laboratoire d'Études Aérodynamique-LEA*) of *Ecole Nationale Supérieure de Mécanique et d'Aérotechnique (ENSMA).* I would like to thank ENSMA for inviting me into their laboratories and providing me with the facilities to accomplish my studies. Also, I would like to thank my supervisor, Dr. Alemdaroğlu, for providing me to take part in this joint project and giving me the opportunity to enlarge my vision.

For his endless support and encouragement and never ending patience, I would like to thank my supervisor in ENSMA, Dr. Andreas Spohn. By sharing with me the equipments and software of his own creation, he has provided me with enormous professional experience and knowledge. I also feel great appreciation for his hospitality and making me feel comfortable in a foreign country.

Also for their precious assistance, I would like to mention Mme Françoise Tournerie and Mlle Aurelie Cotillon for their aid with all my administrative problems, Mr. Pierro Lacombe, Mr. Patrice Allary for their technical assistance and Mr. Sébastien Courtine, whom we shared the same facilities, for devoting me his precious time.

TABLE OF CONTENTS

LIST OF FIGURES

NOMENCLATURE

$\boldsymbol{A}$	Constant in stream function, related to the flow rate.
$\boldsymbol{A_1}$	Area between the leading edge of the model and the free surface level.
$\boldsymbol{A_2}$	The area between the free surface level and the edge of the displacement boundary layer.
$\boldsymbol{a_1}$	Distance between the chordline and the ground.
$\boldsymbol{a_2}$	Distance between the chordline and the free-surface.
$\boldsymbol{h}$	Distance of the model from the channel ground.
α	Slant angle.
$\alpha_{critical}$	Critical slant angle.
$\boldsymbol{b}$	Span.
$\boldsymbol{l}$	Length.
$\boldsymbol{c}$	Chord.
$\boldsymbol{C_D}$	Total Drag Coefficient.
$\boldsymbol{\Gamma}$	Circulation.
$\boldsymbol{\Gamma_o}$	Circulation without wall interference.
$\boldsymbol{\delta}$	Boundary layer thickness.
$\boldsymbol{\delta_1}$	Boundary layer displacement thickness.
$\boldsymbol{g}$	Gravitational acceleration.
$\boldsymbol{\Phi}$	Potential function.
ψ	Stream function.
η	Non-dimensional coordinate
$\boldsymbol{Re}$	Reynolds Number
$\boldsymbol{Re_x}$	Local Reynolds number.
$\boldsymbol{m}$	Pressure (or velocity) gradient parameter.
$\boldsymbol{\beta}$	Angle dependent on pressure (or velocity) gradient parameter.
$\boldsymbol{\mu}$	Kinematic viscosity.
$\boldsymbol{\upsilon}$	Dynamic viscosity.

p	Pressure.
K(x)	Pressure drop increment.
Q	Volumetric flow rate.
Qmax	Maximum volumetric flow rate.
R	Radius of curvature.
r	Radial component.
x	x distance.
y	y distance.
z	z distance.
θ	Tangential component.
x_s	Separation location in x-direction.
ρ	Density.
T_{air}	Air temperature.
T_w	Water temperature.
τ	Frictional shearing stress.
Vx	x-component of velocity
u	x-component of velocity.
U	External velocity
Ue	Edge velocity.
$U_\infty = U_{inf}$	Free Stream velocity
V_1, V_2	Upstream and downstream velocity.
V2	Downstream .velocity.
Vr	Radial component of velocity.
V_θ	Tangential velocity.
Vt	Terminal velocity.
ε_{tot}	Total error.
ε_{rms}	RMS error.
ε_{bias}	Bias error.
ε_{sys}	Systematic error.
ε_{resid}	Residual error.
n	Number of pixels.
d	Resolving power of the image processing by.
L	The actual size of the object to be pictured.

CHAPTER 1

INTRODUCTION TO SALIENT EDGE FLOW SEPARATION

1.1 Introduction

This thesis investigates flow separation from a salient edge experimentally. The study focuses on a highly two-dimensional configuration to simplify the more complex three-dimensional flow separation conditions, generally observed on the rear part of bluff bodies. In order to facilitate the investigation by flow visualizations and particle image velocity measurements, the experiments were carried out in a low-speed water channel. To examine the influence of different slant angles on flow separation, a model composed of a fixed horizontal front panel and a movable rear panel is installed in the test section. A suction device allows controlling the flow conditions upstream of the salient edge. The experiments indicate the existence of two different types of flow separations. First boundary layer separation due to an adverse pressure gradient, second inertial separation related to the geometrical singularity at the salient edge. Both types of separations are found to be dependent on Reynolds number.

Flow separations from salient edges play an important part in the determination of aerodynamic characteristics of bluff bodies. Figure 1.1 shows two examples of such salient edges along the edges of a cargo compartment of an aircraft and along the edges of the rear slant of an automotive vehicle. They lead to flow separation with formation of an unsteady wake flow causing drag, noise and unsteady forces. In particular, the drag properties of bluff bodies are strongly dependent on the dimension of these separations and its associated vortical flow. In this study, we focus on a simple case of salient edge flow: the salient edge perpendicular to the free stream velocity, such as the one between the roof and rear panel of a simplified automotive vehicle.

(a)

(b)

Figure 1.1: Salient edges of bluff bodies **(a)** cargo compartment door of a CN-235 military cargo aircraft **(b)** rear-roof of a Mercedes A Series automobile.

Indeed, because of the complicated geometries of automotive vehicles, studies of the flow structure over real cars are complicated and difficult to analyze. Hence, simplified geometries, which represent the basic features of an automobile body, such as the Ahmed Reference Model by [Morel, 1978] were introduced for research on car aerodynamics. Figure 1.2 shows such a simplified model, the so-called Ahmed body, at scale 0.28.

Figure 1.2: Ahmed Reference body at scale 0.28.

Ahmed et al (1984) and later Spohn et al (2002) found that this body leads to highly complicated three- and two-dimensional flow structures depending on slant angle. Figure 1.3 gives an idea of the complexity in the three-dimensional case with formation of longitudinal vortices.

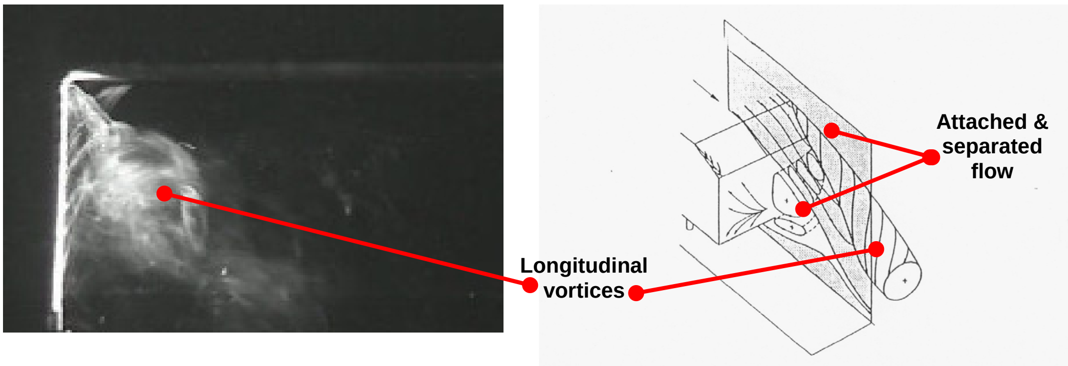

(a) **(b)**

Figure 1.3: (a) Trailing vortex arising at the sidewall of the hatch panel visualized by electrolytic precipitation technique. Only the left side is shown. View from behind in the upstream direction. Illumination by white light [Spohn & Gilliéron, 2002]. **(b)** Wake flow pattern for a large subcritical upper-rear slant angle of fastbacks [Hucho, 1993].

To understand this complicated flow topology and the passage from 3-D to 2-D flow structures, the geometry needs to be decomposed in more elementary systems. The experimental model that we investigate in this research project is designed to investigate only the salient edge perpendicular to the free-stream direction, avoiding the influence of trailing vortices present on the Ahmed body.

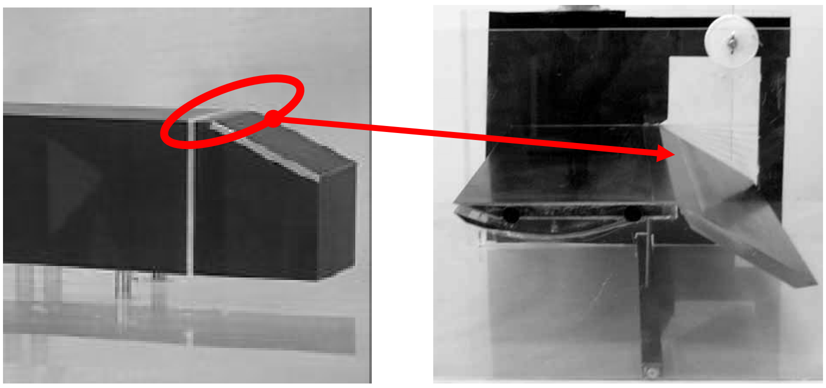

Figure 1.4: The model used in this experimental study simulates the rear part of the Ahmed Body in 2-D.

In the following, we give first an overview over the implications of aerodynamic drag on car fuel consumption, which motivated our study. After underlining the importance of drag in car aerodynamics, the evolution of the automobile drag coefficients in the past is explained briefly. The contribution of the rear part of a car to the total aerodynamic drag, which is closely related to the subject of this thesis, is discussed. Finally, we give an outline of this thesis to guide the reader.

1.2 The importance of aerodynamic drag in car design: a literature survey

Some of the factors that influence the fuel consumption of an automotive vehicle are the engine efficiency, tire rolling resistance and the total aerodynamic drag of the vehicle. For a typical mid-sized American car, the aerodynamic drag is responsible for ~46 % of the total fuel consumption for highway driving schedule and ~14 % for urban driving schedule [Hucho, 1993]. Although the aerodynamic drag is not the major contributor of the total fuel consumption, reducing the fuel consumption by improving the car aerodynamics is still possible.

Design of a car is influenced by many requirements such as fashion, social considerations, competitive environment, traffic policy, economic environment, regulations and technology. Until the last quarter of the past century, aerodynamic requirements played only a minor role in car design. Although it is known for a long time that drag coefficients as low as C_D=0.15 can be achieved for well streamlined cars [see Hucho, 1993], in practice only research vehicles obtained such a low value in the past. It is only since the oil crisis in 1970’s that automobile industry is forced to reduce the drag coefficients significantly, in order to decrease fuel consumption. More recently, increasing danger of global warming due to air pollution and the requirement of reducing the emitted noise levels, underline the need for further aerodynamic improvement of car design.

Figure 1.5 from Hucho (1993) gives an overview of the evolution of C_D of the vehicles of their times in the last decades.

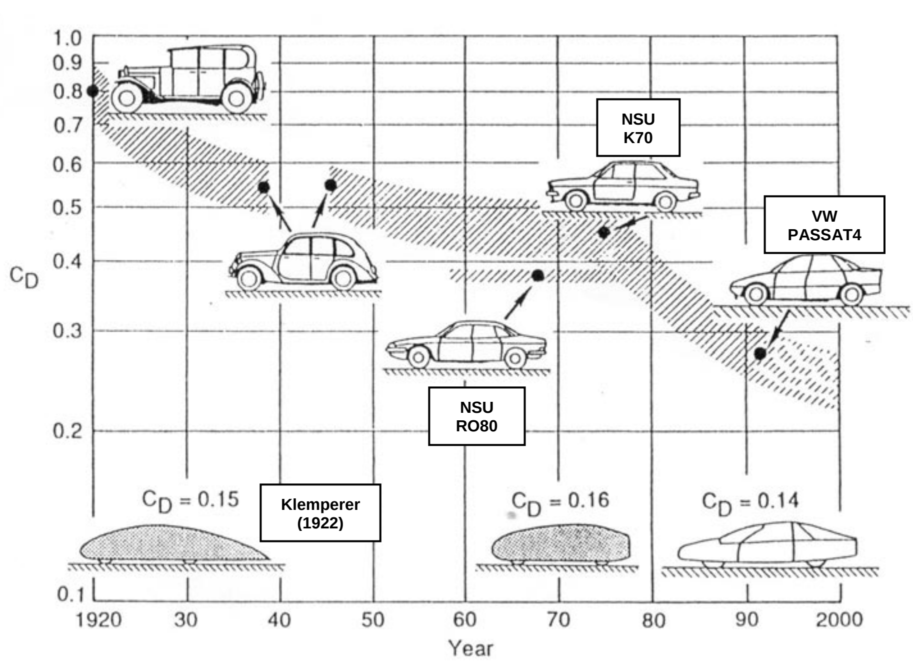

Figure 1.5: The drag history of cars. Using a logarithmic scale for drag emphasizes how difficult it is to achieve very low drag values. Research has been far ahead of what has been realized in production [Hucho, 1993].

Today, the typical modern automobile achieves a drag coefficient between 0.30 and 0.35. Sports utility vehicles (SUV), with their larger, flatter shapes, typically achieve a C_D of 0.35-0.45. Sports cars can achieve C_D's as low as 0.25-0.30. Current trend in automotive market is going through the hybrid cars. The greatest problem of the hybrid cars is their limited driving range which is directly influenced by drag. Drag coefficients less than 0.20 are feasible for hybrid and electrical cars. Hence, the requirement of low drag coefficients will be better understood after the hybrid cars take their place in the market [Hucho, 1993].

Hucho (1993) states that, although it depends on the driving-schedule, when the C_DA of an average midsized American car is changed 1 %, the fuel consumption changes ~0.14 % for urban, ~0.46 % for highway driving schedules. For the Euromix cycle, which is average driving schedule, accepted in Europe, this 1 % change signifies ~0.3 % change for spark-ignition engine cars and ~0.4 % change for diesel engine cars. The benefits of reduced aerodynamic drag are not limited to reduced fuel consumption. If no other changes are made in a vehicle, reduced aerodynamic drag allows increased acceleration capability and increased top speed.

According to Hucho (1993), for any current car that has received aerodynamic attention, the contribution of the fore-body to drag is small (4.2 % to 7.3 % depending on the base slant angle [Ahmed, 1984]). The major aerodynamic problem is at the rear part. However, numerical predictions and experimental studies are difficult in this region because of the complexity of the flow structures. The location at which the flow separates determines the size of the separation zone, and consequently the drag force [Lienhart et al, 2002]. To obtain lower drag coefficients for future car designs, a better formation of these flow separations and the dynamic behavior of the released vortex wake is required. For this objective, future designs should take advantage of active and passive control devices to control the flow separation from the rear part of the car [Spohn & Gilliéron, 2002].

The flow around the rear part of the vehicles and in particular the influence of the slant angle variations on drag has been extensively investigated over years. The nature of the flow behavior in this region is illustrated in Figure 1.6, where the slant angle α is measured from the horizontal [Hucho, 1993].

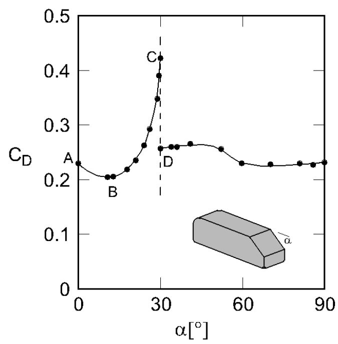

(a)

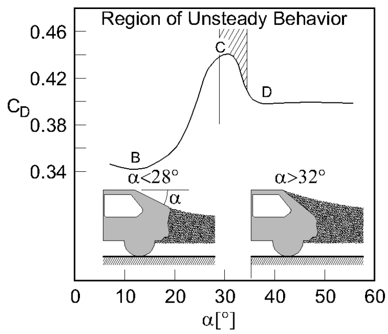

(b)

Figure 1.6: Dependence of drag, C_D, on the slant angle α of the upper-rear surface of fastbacks, and the existence of a critical phenomenon; **(a)** simple body, **(b)** automobile.

As the rear roof of the simple body is progressively inclined beginning from zero angle, (point A, Figure 1.6a), trailing vortices are formed along the lateral edges of the slanted edge. Formation of these vortices increases drag. However, the downwash generated between them promotes attached flow in the central portion of the slant, leading to a pressure recovery which is drag reducing [Hucho, 1993].

As the angle increases the competing mechanisms grow individually, and the net drag reaches a minimum at ~15^o (point B). It is to be noted that vortex drag is not a minimum at this point. At a sufficiently larger angle, the drag increases even though nominally attached flow is maintained on the centerline of the slanted surface [Hucho, 1993].

At point C the drag is maximum and the trailing vortices are of maximum strength. At a slightly greater angle (the critical angle) the vortices lift off and/or burst, and the induced downwash is no longer able to produce attached flow on the centerline. The flow detaches abruptly, and a fully-separated flow develops on the slanted surface (point D). The drag level is comparable to that of the initial square-back (zero angle) configuration. For this simple body (Figure 1.6a) with sharp salient edges, the transition is discontinuous and unidirectional [Hucho, 1993].

The same general behavior is observed for an actual automobile, where it was originally discovered (Figure 1.6b) [Hucho, 1993]. This has rounded edges in the slanted-roof area, and the flow pattern at transition can be bistable, switching slowly (with a period of many seconds) and randomly between that of C and D. As the slant angle increases the bistability eventually disappears and only the D-pattern persists. For angles greater than this, the drag of the D-pattern is relatively insensitive to slant angle [Hucho, 1993].

Although these results create some basic understanding of the flow separation phenomenon from the rear part of the Ahmed body, they do not correlate exactly with the numerical solutions [Gilliéron, 1999]. The rear part separation zone appears to be more complex than previously found by Ahmed et al [Spohn & Gilliéron, 2002]. As a first step to get a better understanding of this complex phenomenon, simplifications by highly two-dimensional configurations are required.

Former studies of McEwan (2001) and Studer (2002) already used a highly two-dimensional model to simulate the flow around a salient edge. However, their model had a major shortcut; it didn't allow controlling the upstream flow conditions for slant angles greater than 20^o. One of the first objectives of this study was to improve the model for a better control of these upstream conditions. The second objective of this study was to analyze the separated flow region in more detail. At this end, we used a complementary approach by flow visualization and PIV measurements. In the following, we give an outline of the chapters in this report.

In order to analyze flow separation at a salient edge with variable slant angle, in chapter 2 we begin with the description of some theoretical background on flow separation.

The test model with the variable slant angle is presented in chapter 3. Furthermore, this chapter describes the water channel facility and different equipments such as the suction system, the illumination system and the data acquisition system.

During the experimental investigations we used the hydrogen bubble technique, the electrolytic precipitation technique and PIV measurements. Basic operating principles of these methods are described in chapter 4.

The shortcuts of the existing model, for the investigation of the flow separation from salient edge were removed before studying the separation problem. This process allowed us to control the upstream conditions more effectively for a wider range of angles and velocities. Details of these improvements are presented in chapter 5.

Chapter 6 and 7 are devoted to the presentation of experimental results of the flow structure around the model. Results concerning the flow conditions upstream of the salient edge are presented in chapter 6. The investigation of flow separation is described in chapter 7. Comparisons between visualizations obtained with electrolytic precipitation technique and PIV measurements are presented in this chapter. All these results are discussed in the light of the theoretical arguments given in chapter 2. To complete the investigation, the influence of slant angle and Reynolds number are examined.

The summary and conclusion of the study is given in Chapter 8.

CHAPTER 2

THEORY OF FLOW SEPARATION

2.1 Introduction

In all real-life applications of Fluid Mechanics, fluids are viscous, leading to the formation of boundary layers along the surface of the streamlined bodies. For bodies which are not sufficiently streamlined, these boundary layers can be at the origin of an additional phenomenon, the so called *“flow separation”*. In this chapter, we will explain the theoretical background of flow separation under the assumption of two-dimensional flow. In the first section, we will explain the boundary layer concept, which is closely related to flow separation. The evolution of the characteristics of the boundary layer with zero pressure gradient, the so called Blasius layer, is also discussed in this part. This evolution is specifically important in our case for the control of the upstream conditions of separation. In the next section, the different origins of flow separation are explained using two different concepts: first flow separation due to a pressure gradient and second separation due to inertia. These two concepts are important in view of the experimental investigation presented in the following chapters since both types of separation can occur on the rear panel of our model. In the last section of this chapter, the separation phenomenon will be investigated more specifically by using the solution of the Falkner-Skan equation concerning wedge flows similar to our experimental arrangement.

2.2 Boundary Layers

This section gives basics of the boundary layer theory. First boundary layer concept will be introduced. Then boundary layer thickness will be defined.

2.2.1 The Boundary Layer Concept

In the case of real fluids, particles adjacent to the body surface do not slip leading to viscous forces inside a thin layer in the immediate neighborhood of the solid wall. Due to the retarding effect of these friction forces the velocity of the fluid inside this thin layer decreases from the external velocity towards zero on the wall. This layer is called the "*boundary laye*r**"** [Schlichting, 1968].

Below, the sketch of a velocity boundary layer on a flat plate is shown in Figure 2.1 with exaggerated dimensions. In front of the leading edge of the plate the velocity distribution is assumed to be approximately uniform. It is observed that, downstream of the leading edge, the fluid is slowed down in the close neighborhood of the wall. With increasing distance from the leading edge in the downstream direction, the thickness of the retarded layer increases continuously, thus increasing the quantity of fluid affected by friction.

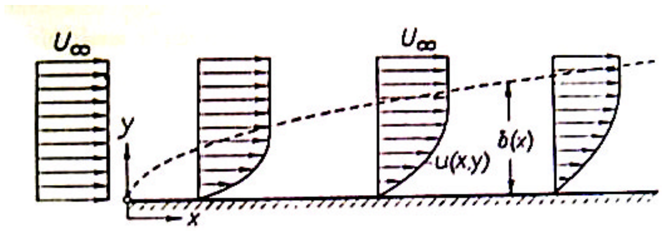

Figure 2.1: Sketch of boundary layer on a flat plate in parallel flow at zero incidence [Schlichting, 1968].

Since the boundary layer results from a viscous diffusion process, the thickness of the boundary layer decreases with decreasing viscosity. However, no matter how small the viscosity is (i.e. how high Reynolds numbers are), the frictional shearing stresses ($\tau = \mu \partial u / \partial y$) in the boundary layer are always present because of the large velocity gradients across the boundary layer. Because of this physical situation, the flow field at high Reynolds number, can be separated into two regions for mathematical analysis; a thin boundary layer, in which forces due to friction must be taken into account and a region outside this boundary layer, where these forces can be neglected. Viscous forces do not influence the motion in the outside region so that the fluid motion can be modeled by potential flow [Schlichting, 1968].

2.2.2 Boundary Layer Thickness

Two different boundary layer thickness definitions are present in Figure 2.2 (δ and δ_1).

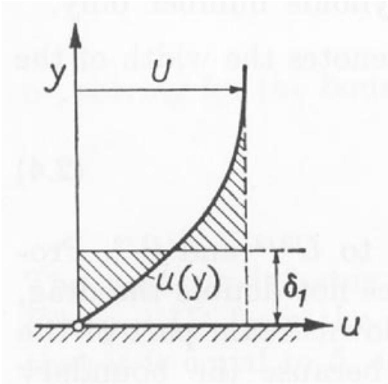

Figure 2.2: Boundary layer thickness δ and displacement thickness δ_1 in a boundary layer *[Schlichting, 1968]*

The boundary layer thickness, δ, is defined as the distance from the wall where the velocity differs by one per cent from the external velocity U [Schlichting, 1968].

The displacement thickness δ_1, indicates the distance by which the external streamlines are shifted towards the interior of the fluid, owing to the formation of the boundary layer. It is defined by the equation

$$U\delta_1 = \int_{y=0}^{\infty} (U-u)dy \tag{2.1}$$

Schlichting (1968) shows that, in the case of a flat plate in parallel flow and at zero incidence, the displacement thickness, δ_1 is about 1/3 of the boundary-layer thickness δ.

For a flat plate without streamwise pressure gradient the thickness of a boundary layer δ can be estimated by carrying out an order of magnitude comparison between the inertial forces and frictional forces, inside the boundary layer [Schlichting, 1968].

The inertia force per unit volume is proportional to $\rho u \partial u/\partial x$. At a streamwise position x of the flat plate, the gradient $\partial u/\partial x$ is proportional to U/x, where U denotes the velocity outside the boundary layer. Hence the inertia force per unit volume is of the order $\rho U^2/x$. On the other hand the friction force per unit volume is equal to $\partial \tau/\partial y$, which, on the assumption of laminar flow, is equal to $\mu \partial^2 u / \partial y^2$. The velocity gradient $\partial u/\partial y$ in a direction perpendicular to the wall is of the order U/δ so that the friction force per unit volume is $\partial \tau/\partial y \sim \mu U/\delta^2$. Since friction and inertia forces must be of the same order of magnitude, we obtain the following relation:

$$\mu \frac{U}{\delta^2} \sim \frac{\rho U^2}{x} \tag{2.2}$$

or, solving for the boundary-layer thickness δ:

$$\delta \sim \sqrt{\frac{\mu x}{\rho U}} = \sqrt{\frac{\nu x}{U}} \tag{2.3}$$

where ν is the kinematic viscosity, μ/ρ.

For an infinitely long flat plate under steady, laminar flow, parallel to its axis without any pressure gradient in streamwise direction ($\partial p/\partial x \equiv 0$), the numerical factor, which can be deduced from the exact solution of Blasius is approximately 5, [Schlichting, 1968].

$$\delta = 5\sqrt{\frac{\nu x}{U}} \tag{2.4}$$

The dimensionless boundary-layer thickness, referred to the streamwise position x, becomes:

$$\frac{\delta}{x} = 5\sqrt{\frac{\nu}{Ux}} = \frac{5}{\sqrt{\mathrm{Re}_x}} \tag{2.5}$$

where Re_x denotes the Reynolds number related to the streamwise position x over the plate. The relative boundary layer thickness δ/x decreases with increasing Reynolds number as

$1/\sqrt{Re}$ so that in the limiting case of frictionless flow, with $Re \rightarrow \infty$, the boundary-layer thickness goes to zero.

2.3 Structure of two dimensional flow separation

If a body is not sufficiently well streamlined, the boundary layer separates from the body surface. In the downstream part of this separation, flow direction is opposite to the main flow, forming a recirculation region (Figure 2.3). The existence of this recirculation region leads to an increase in pressure drag and unsteady vortex shedding. These unsteady effects are present for both two dimensional and three dimensional flow cases. However, in our investigation, the configuration is highly two-dimensional so that we restrict our discussion to this type of flow separation.

Separation is a phenomenon that can occur under two different conditions: firstly, boundary layer separation due to an adverse pressure gradient and secondly, inertial separation due to geometrical singularities which imply strong accelerations transverse to the streamlines. In the following, we study each of these separately.

2.3.1 Separation due to pressure gradients

In general, when fluid flows around a body, the pressure varies along the body surface. The pressure gradient in the streamwise direction can be either adverse or favorable, whereas, the pressure gradient inside the boundary layer, normal to the surface, remains negligibly small within the boundary layer approximations. Hence, the pressure within the boundary layer is imposed by the flow outside of the boundary layer.

Physically, if we consider the fluid in a region with an adverse pressure gradient $dp/dx>0$, particles, moving in the region close to the wall are slowed down by the adverse pressure gradient. Since the momentum of those particles is small, their ability to move forward against the pressure rise is more limited compared to those outside the boundary layer. Such fluid particles are finally brought to rest and start to accelerate in the reverse direction if the pressure gradient is sufficiently high as shown in Figure 2.3 on point S. Because of the flow reversal the boundary layer considerably thickens leading to flow of boundary-layer material towards the interior of the flow region. This thickening of the boundary layer and the reversal of flow is sketched in Figure 2.3.

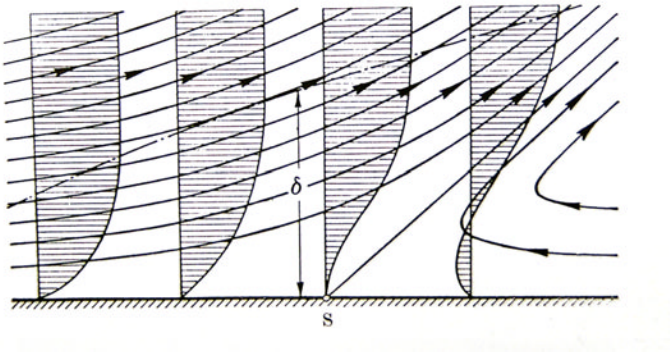

Figure 2.3: Scheme of the flow in the boundary layer near the separation point.
S : separation point [Schlichting, 1968]

Hence, adverse pressure gradient situations can lead to flow separations and thus influence the characteristics of the entire flow.

At the separation point *S*, a streamline intersects the wall at a definite angle. This separation point is determined by the condition that the velocity gradient normal to the wall vanishes at this point [Schlichting, 1968]:

$$\left(\frac{\partial u}{\partial y}\right)_{wall} = 0 \quad \textit{(separation condition)} \tag{2.6}$$

Hence, the difference between $x<x_s$ and $x>x_s$ is in the sign of $(\partial u/\partial y)_{y=0}$.

Finally we should mention that the boundary layer theory breaks down at separation since the thickness of the layer is not small anymore.

2.3.2 Inertial Separation (from a salient edge)

Besides the adverse axial pressure gradient, another cause for separation can be a sudden change in surface geometry.

Before discussing flow separation due to a sudden change in geometry in more detail, we should first explain the forces acting on a fluid element moving on a curved path under the assumption of steady flow. As shown in Figure 2.4, during the motion of fluid element, the centrifugal acceleration V_θ^2 / R is compensated by the acceleration caused by the radial pressure gradient $1/\rho \, \partial p / \partial r$:

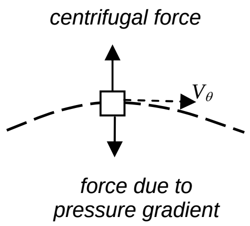

$$\frac{1}{\rho}\frac{\partial p}{\partial r} = \frac{V_\theta^2}{R} \tag{2.7}$$

Figure 2.4: Forces on fluid element on a curved path in steady flow.

where R is the radius of curvature of the streamline and V_θ the velocity tangent to the streamline. Thus less radius of curvature of the streamlines implies a stronger radial pressure gradient for equilibrium.

An extreme example for a small radius of curvature is a body with a salient edge as sketched in Figure 2.5. A salient edge is geometrically a singular point with zero radius of curvature.

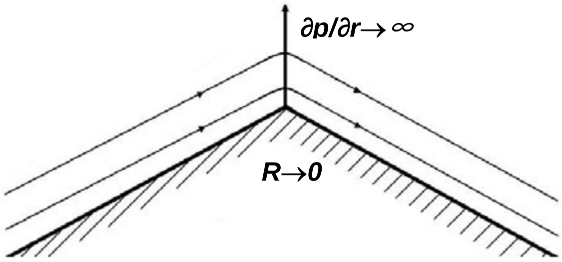

Figure 2.5: Schematic drawing of a body with a salient edge and assumption of flow around the salient edge.

According to equation (2.7), the flow must experience an infinite radial pressure gradient to obtain an infinite acceleration necessary to turn the velocity vector of the fluid element at the corner in the new flow direction. However, for a real fluid particle with inertia, an infinite acceleration and an infinite radial pressure gradient are not physically possible. Hence, the flow separates from the salient edge at point *S* and this type of separation is called inertial separation (Figure 2.6).

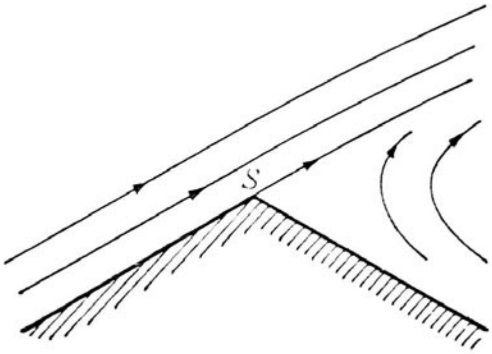

Figure 2.6: Inertial separation from a rigid wall *[Batchelor, 1980]*.

The flow separates from the salient edge almost tangentially. Thus, the radius of curvature *R* of the separated flow goes to ∞ and the centrifugal acceleration becomes zero avoiding radial pressure gradients due to equation (2.7). This separation mechanism has been discussed by Batchelor (1980).

The rotational flow at the lee side of the salient edge, sketched in Figure 2.6, is the result of viscous entrainment. The high velocity flow which leaves the salient edge tangentially creates a circulation inside the separation region. The resulting motion is an eddy circulation downstream of the salient edge.

2.4 Investigation of the separation phenomenon in our case

Up to this point, the mechanisms that produce flow separation were explained. In this section, we will investigate these phenomenons in the case of our model.

2.4.1 Investigation of separation with Falkner – Skan solution

In order to answer the question of whether and where separation occurs, it is necessary to integrate the boundary layer equations which are defined by:

$$u\frac{\partial u}{\partial x}+v\frac{\partial u}{\partial y}=-\frac{1}{\rho}\frac{dp}{dx}+\nu\frac{\partial^2 u}{\partial y^2} \qquad \textbf{(2.7a)}$$

$$\frac{\partial u}{\partial x}+\frac{\partial v}{\partial y}=0 \qquad \textbf{(2.7b)}$$

for steady and incompressible flow in 2D [Schlichting, 1968].

Solutions of these boundary layer equations were studied by Falkner and Skan for the class of flows, where the edge velocity distribution $u_e(x)$ of the boundary layer may be described by:

$$u_e(x)=u_1 x^m \qquad \textbf{(2.8)}$$

Here u_1 and m are constants. This velocity distribution corresponds to the situation of corner flows described by potential flow theory. Many potential flows are of this kind. Figure 2.7 shows some of the physical interpretations of this kind of flows.

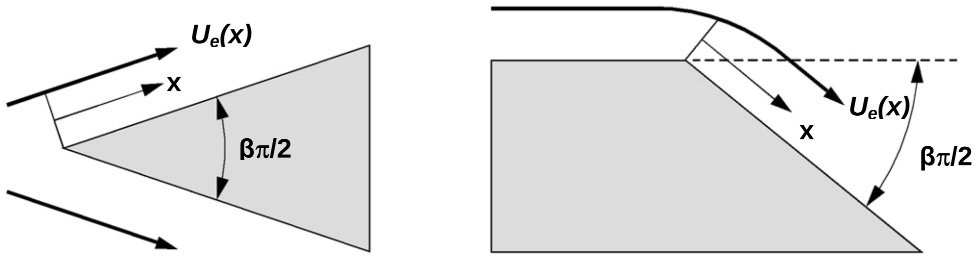

a) 0 ≤ β≤ 2; 0 ≤ m ≤ ∞ ***b) -2 ≤ β≤0; -1/2 ≤ m ≤0***

Figure 2.7: Some examples of the potential flows of type $u_e(x) = u_1 x^m$ a) for positive β b) for negative β.

According to Cousteix (1988), the parameter *m* in equation 2.8 is the parameter of pressure (or velocity) gradient and it is related with angle β in Figure 2.7 by the equation:

$$\beta = \frac{2m}{m+1} \qquad \textbf{(2.9)}$$

The significance of this pressure gradient parameter in some potential flows is given in Table 2.1.

Table 8.1: Physical interpretations of some values of β.

i)	***-2 ≤ β≤0; -1/2 ≤ m ≤0***	Flow around an expansion corner of turning angle β(π/2).
ii)	***β=0, m=0***	Flat plate
iii)	***0 ≤ β≤ 2; 0 ≤ m ≤ ∞***	Flow against a wedge of included angle βπ
iv)	***β = 1, m = 1***	Plane stagnation point (180^o wedge)
v)	***β = 4, m = -2***	Doublet flow near a plane wall
vi)	***β = 5, m = -5/3***	Doublet flow near a 90^o corner
vii)	***β = ∞, m = -1***	Flow towards a point sink
viii)	***β = -0.199***	~18^o wedge (Separation initiates)

For our investigation, case *i* is the most relevant case. In order to find whether and where separation occurs, the stream function $\psi(x, y)$ and the non-dimensional coordinate η are introduced into the boundary layer equations (2.7*a* & 2.7*b*):

$$\psi = \sqrt{\frac{2}{m+1} \cdot \nu u_e x} \cdot f(\eta) \quad \textbf{(2.10a)}$$

$$\eta = y\sqrt{\frac{m+1}{2} \cdot \frac{u_e}{\nu x}} \quad \textbf{(2.10b)}$$

After these transformations, the boundary layer equations reduce into a single ODE which is also known as the Falkner-Skan equation [see Schlichting, 1968]:

$$f''' + ff'' + \beta(1 - f'^2) = 0 \quad \textbf{(2.11)}$$

with the boundary conditions:

$$\eta = 0: \qquad f = 0, f' = 0$$
$$\eta = \infty: \qquad f' = 1$$

This equation was first deduced by Falkner and Skan and its solutions were later investigated in detail by Hartree (1937). Hartree's solution is represented in Figure 2.8.

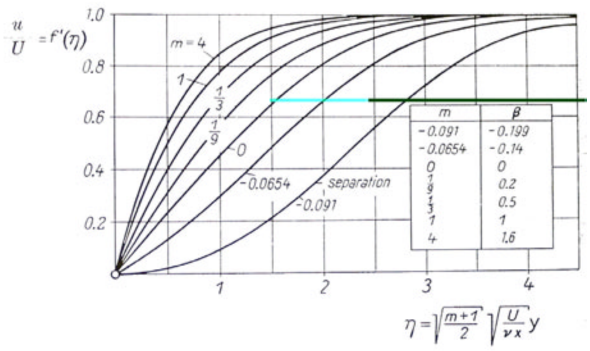

m	β
-0.091	-0.199
-0.0654	-0.14
0	0
1/9	0.2
1/3	0.5
1	1
4	1.6

Figure 2.8: Velocity distribution in the laminar boundary layer in the flow which is described by $u_e(x) = u_1 x^m$ [Schlichting, 1968]

In the case of accelerated flow ($m > 0$, $\beta > 0$) the velocity profiles have no point of inflexion, whereas in the case of decelerated flow, ($m < 0$, $\beta < 0$) they exhibit a point of inflexion. Separation occurs for β = -0.199, i.e. for m = -0.091. For a potential corner flow, this β corresponds to ~18^o of wedge angle (case *viii*). This result shows that the laminar boundary layer is able to support only a very small deceleration without separation occuring. In the case of our model, such small pressure gradients can only be expected at small slant angles and low velocities.

2.4.2 Investigation of the potential flow over the model

The corner flows investigated by Falkner and Skan are very similar to the flow on the upper surface of our model. To see this, we investigate here some particularities of these potential flows in more detail. Figure 2.9 shows the coordinate system which is used for this investigation. The angle α represents the deflection angle of the base slant.

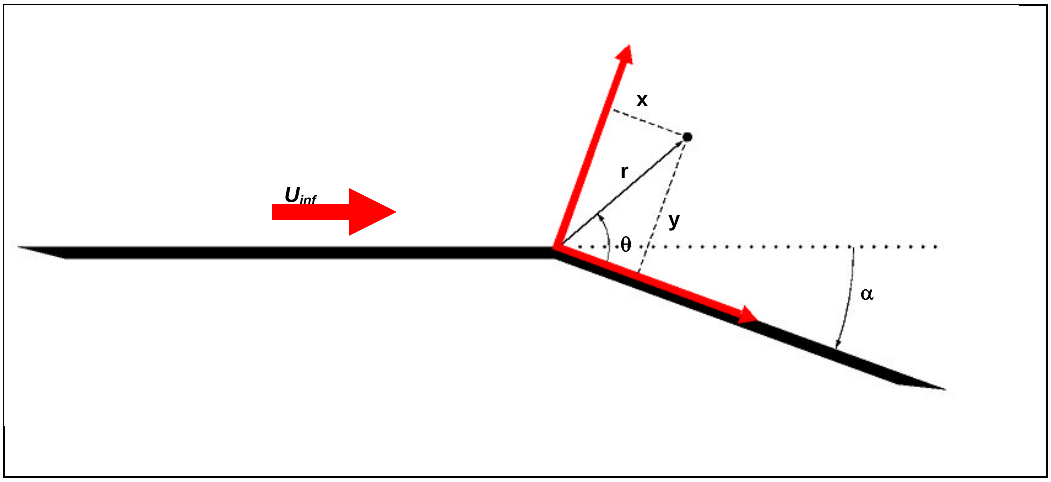

Figure 2.9: Coordinate system over the downstream plate of the model for the investigation of the potential flow. α is taken between a horizontal line and the downstream plate.

The general form of the potential function of the flow around a corner in cylindrical coordinates is defined by [Munson, 1998]:

$$\phi = Ar^{\pi/\alpha+\pi}\cos\frac{\pi\theta}{(\alpha+\pi)} \qquad \textbf{(2.12)}$$

where A is a constant dependant to the free-stream velocity. Thus the velocity components v_r and v_θ at any point in the flow field are defined by:

$$v_r = \frac{\partial\phi}{\partial r} = -\frac{A\pi}{\alpha+\pi} r^{\left(\frac{\pi}{\alpha+\pi}\right)-1}\sin\left(\frac{\pi\theta}{\alpha+\pi}\right) \qquad \textbf{(2.13a)}$$

$$v_\theta = \frac{1}{r}\frac{\partial\psi}{\partial r} = \frac{A\pi}{\alpha+\pi} r^{\left(\frac{\pi}{\alpha+\pi}\right)-1}\cos\left(\frac{\pi\theta}{\alpha+\pi}\right) \qquad \textbf{(2.13b)}$$

Using these velocity components, pressure distribution of the potential flow can be evaluated with the help of Bernoulli equation:

$$p_s = cst - \frac{1}{2}\rho(v_r^2 + v_\theta^2) \qquad \textbf{(2.14)}$$

Figure 2.10 shows the evaluated equal pressure lines (isobars) over the downstream plate at 5° of base slant angle.

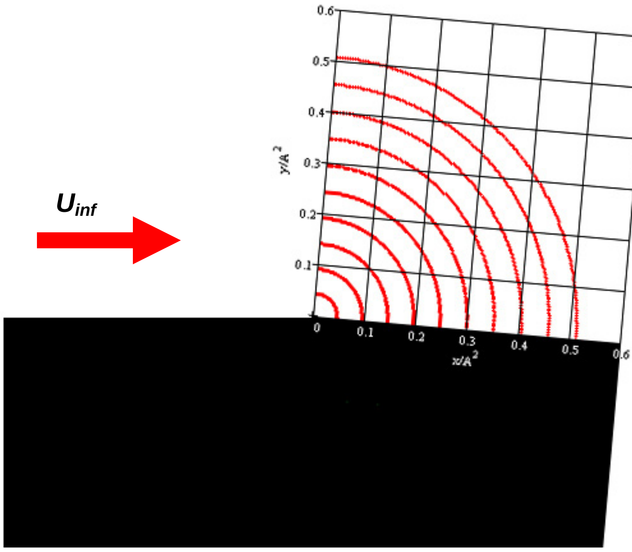

Figure 2.10: Equal pressure lines (isobars) along the downstream plate of the model at 5° of slant angle.

The pressure distribution is circular. According to this distribution, the pressure gradient is in the radial direction and it decreases with increasing *r*. Consequently, the pressure gradient in any radial direction is equal to the wall pressure gradient.

Cousteix (1988), defined the pressure gradient parameter by:

$$m = -\frac{x}{\rho_e u_e^2}\frac{dp}{dx} = \frac{x}{u_e}\frac{du_e}{dx} \tag{2.15}$$

In principal, the actual pressure gradient parameter *m* of the flow can be measured along the wall. However, in our case this is very difficult since we are dealing with velocities of the order of 10 cm/s and pressures of the order of ~5 Pa (~0.5 mm water at 20° C). Hence, our approach to estimate the pressure gradient parameter will be by indirect measurements of the velocity gradient over the model instead of direct pressure measurements.

Since the pressure gradient in the radial direction is defined by:

$$\frac{\partial p}{\partial r} = -\frac{1}{2}\rho A^2\left(\frac{\pi}{\alpha+\pi}\right)^2 2\left(\frac{\pi}{\alpha+\pi}-1\right) r^{2\left(\frac{\pi}{\alpha+\pi}\right)-3} \quad \textbf{(2.16)}$$

the pressure gradient is dependent on the deflection angle of the flow α and the coefficient A, which is dependent on the flow velocity. Hence in the case of our model, the parameters for the flow separation are the base slant angle α, and the Reynolds number built with the free-stream velocity.

Unfortunately we can not expect that the velocity distribution given in equation 2.8 to be valid over the whole plate and for any angle α. According to Figure 2.8, flow separation appears for m smaller than -0.091. Consequently the theory fails for α > ~18^o since m becomes smaller than the critical value. Moreover, according to Stewartson (1953), the theory can not explain the boundary layer profiles after the boundary layer separation has occurred. Finally, according to equation (2.13*a*), $\lim_{x\to 0} v_r$ goes to infinity. Therefore, the boundary layer theory is not applicable in the close neighborhood of the salient edge. As a result, the theory is applicable only in the range between the points far from the salient edge and the separation point, up to ~18 degrees of base slant angle.

Even more complicated, although in the discussion above flow separation was explained by the action of the pressure gradient of the potential flow, the actual flow situation for our model can be very different from the ideal corner flow. Firstly, there is circulation around the model, which induces additional velocity and pressure gradients above the model. This circulation might only be neglected for small base slant angles and small velocities, when circulation tends to zero. Secondly, because of the thickness of the model, there is an additional pressure gradient which is neglected in the calculations for our model assuming that its thickness ratio is very small (around 8 %). Third and most importantly, the velocity law around the model is never the same as in equation 2.8 because of the influence of viscosity on the flow. Hence, a complete explanation of the flow separation by using the potential corner flow assumption should never be expected. However, from a local point of view, the measured pressure gradient can be attributed to a fictive corner flow with the same pressure gradient. As a result, separation of the actual flow takes place when its corresponding fictive potential flow is separated.

For the estimation of pressure gradient parameter, PIV measurements in chapter 7 will be used. However, since we are dealing with a real fluid, the flow along the wall is not potential flow and the relevant gradients must be measured outside the boundary layer in the adjacent irrotational flow. In the next chapter we will investigate the experimental arrangement that we used to study this type of flow in more detail.

CHAPTER 3

EXPERIMENTAL SETUP AND EQUIPMENTS

3.1 Introduction

In this chapter, we introduce the experimental setup and the equipments used during the experiments. The experimental arrangement is composed of five different modules as sketched in Figure 3.1: the model, the water channel, the suction system, the data acquisition system and the illumination system. In the first section we describe the model that we use for the experimental investigation of the flow separation from a salient edge. Then we describe the water channel facility. The next section contains the description of the suction system, which is composed of the turbine meter and the suction pump. The data acquisition equipments are the subject of the following section. Finally we present some details of the illumination system which is crucial for flow visualizations.

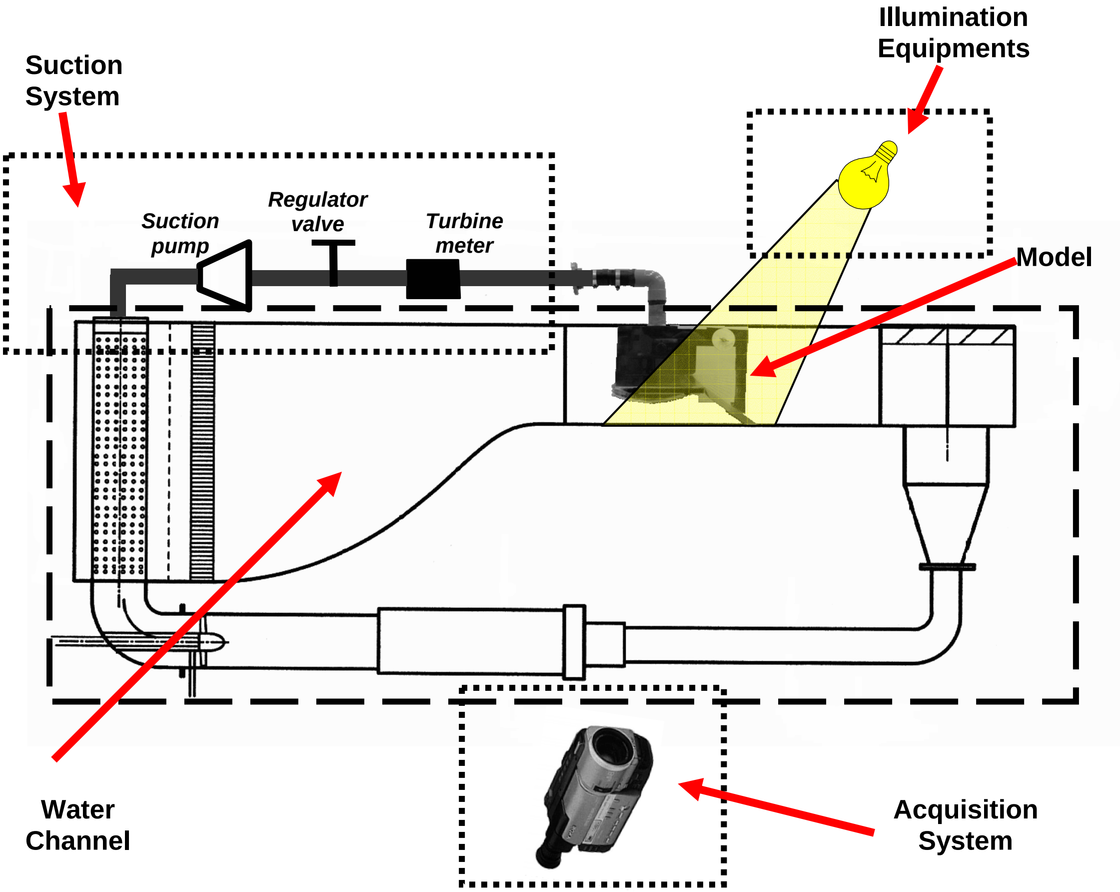

Figure 3.1: Scheme of the modules composing the experimental setup.

3.2 The model

The experimental model is designed to investigate the flow separation from a salient edge. It simulates the rear part of a simplified automotive vehicle model, “Ahmed body”. This model is an improved version of the models used in two former research projects [McEwans, 2001 and Studer, 2002]. The details of the improvements applied to the model after these studies are explained in chapter 5.

Schemes and views of the model are shows in Figure 3.2 and 3.3. The main components of the model are two flat plates, two sidewalls at the lateral limitations of the plates, a plenum chamber under the upstream plate, a suction slit below the leading edge, a pulley mechanism for the fixation of the base slant angle and a connection to the suction system.

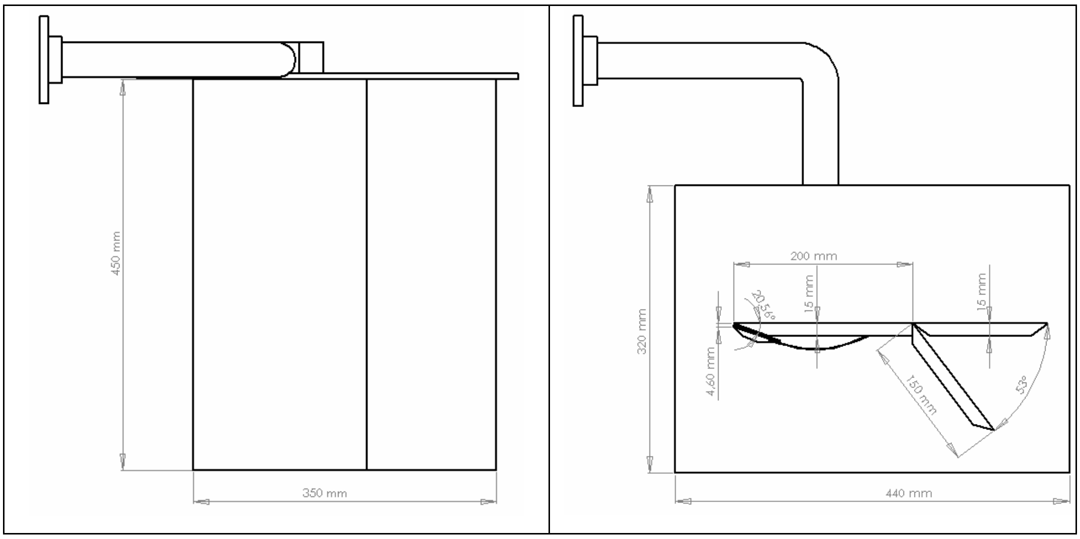

Figure 3.2: Schemes drawings of the model.

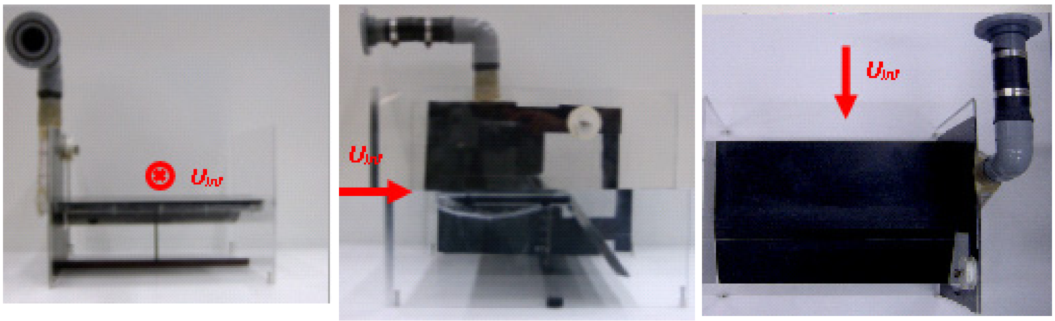

Figure 3.3: Views of the improved model from front, side and top respectively.

The main body of the model is composed of two 15 mm thick Prespex plates. The upstream plate is 450 mm in width and 200 mm in length. It is placed horizontally between two side-plates of 4 mm thickness. It has a wedge shaped leading edge with ~20^{o} of angle. The second plate, which is 150 mm in length, is connected to the end of the first one by means of a black adhesive film. In this way, the edge between the two plates is as sharp as possible. The second plate is free to rotate around the salient edge between the plates, the adhesive film acting as a hinge. The arrangement of the position of the second plate is performed by using a pulley mechanism shown in Figure 3.4. It is possible to change the base slant angle between 0^{o} and 53^{o} degrees with a precision, better than 0.5 degrees.

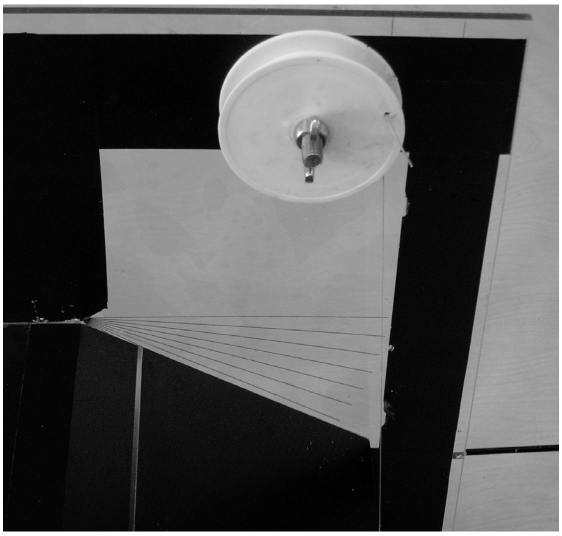

Figure 3.4: Pulley mechanism for the arrangement of the base slant angle and control lines for measurement of the slant angle.

For the control of the flow conditions upstream of the salient edge, we made use of suction. A suction channel was installed below the first plate. Details of the suction requirement and the arrangement of the suction slit are given in chapter 5. The entrance of the suction channel lies under the leading edge and the channel exit is connected to the plenum chamber. The exit of this plenum chamber is related to a vertical convergent channel which allows the transition into a circular pipe (Figure3.5). The model is connected to the suction system by a flexible fitting.

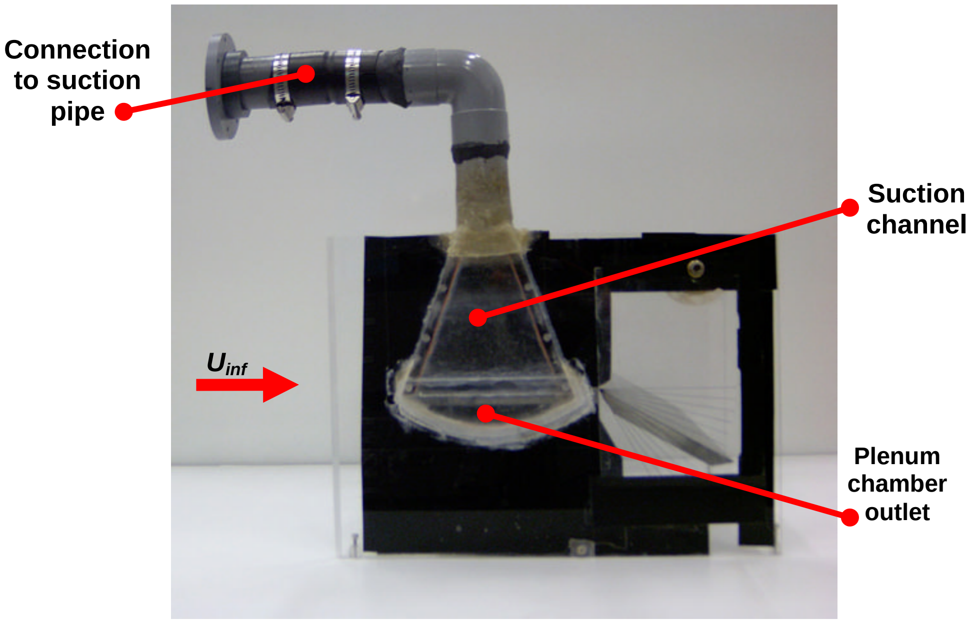

Figure 3.5: Side-view showing the arrangement of plenum chamber, suction channel and the connection to the suction system.

The suction outlet and the tube system are made of PVC and glass fiber. All the surfaces with the exception of the left sidewall are covered with a black adhesive film to avoid reflections of light.

3.3 The Water Channel

In this section the water channel facility and the channel interference effects are described.

3.3.1 The Water Channel Facility

The water channel is a closed loop, low speed water channel. The test-bed has a rectangular cross section of 0.5 m x 0.30 m and a length of 1.5 m. The upper face of the test section was left open with a free surface. This allows the experimenter to manipulate the equipment in the test section easily. All side walls are Prespex which allows flow visualizations from any direction. A lateral water evacuation by cyclones, allows observing the flow through the end-wall of the test-section in the upstream direction. A schematic drawing and the images of the water channel are shown in Figure 3.6 and 3.7 respectively.

The channel is driven by a 5kW AC motor, with a maximum 1400RPM.

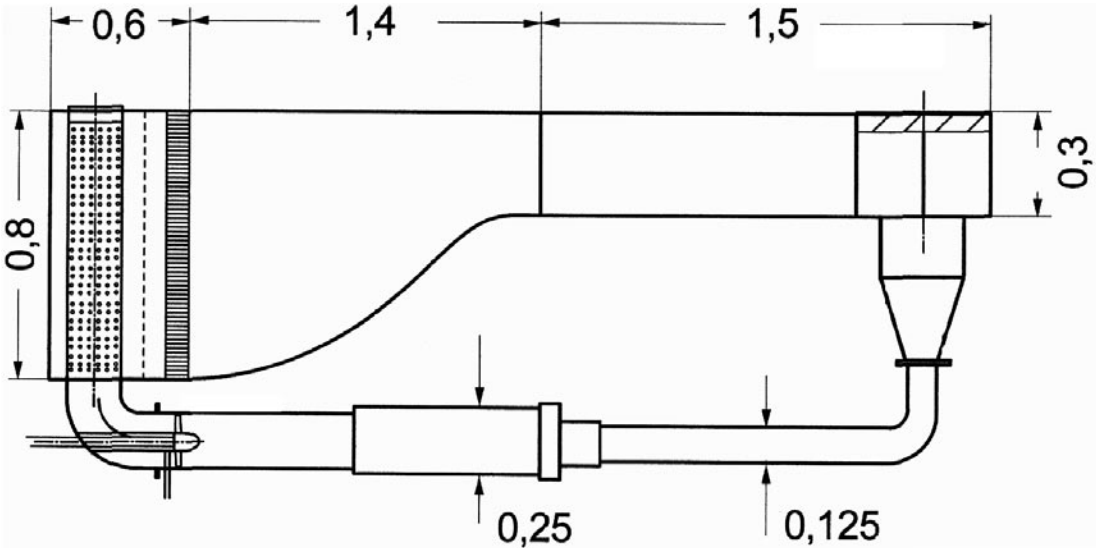

Figure 3.6: Schematic drawing of the water channel *[Spohn,2001]*.

(a)

(b)

Figure 3.7: (a) Side-view of the water tunnel **(b)** view from behind in the upstream direction.

The channel is operational from 3 cm/s up to 40 cm/s. However, at 100 RPM, which corresponds to ~4.35 ± 0.26 cm/s, the motor drive of the channel gets into resonance. Hence the channel can not be run at this velocity. In addition, at velocities higher than ~15 cm/s, the surface waves disturb the flow. Figure 3.8 shows the calibration curve of the channel.

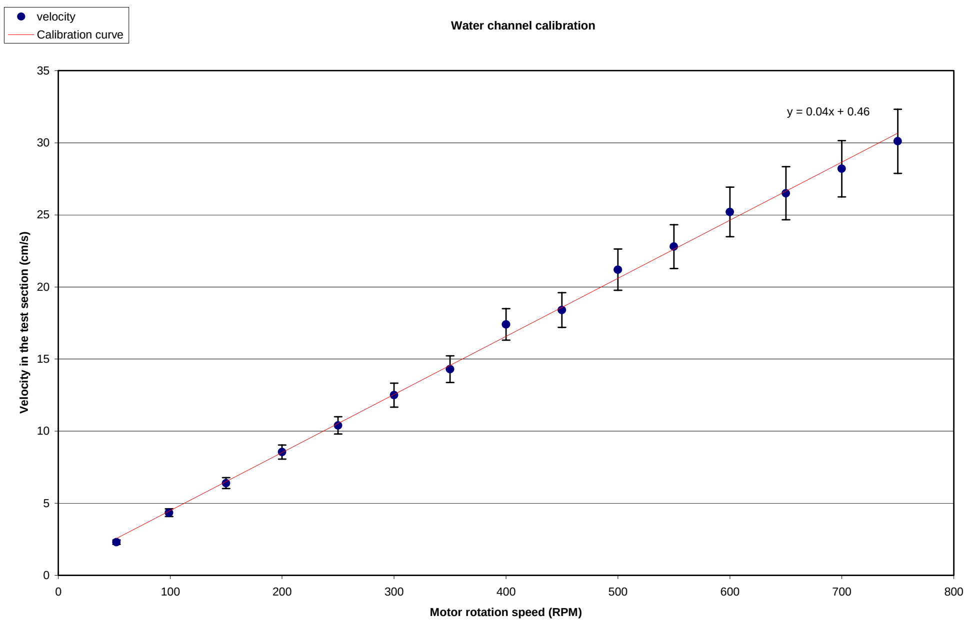

Figure 3.8: Calibration curve of the water channel.

3.3.2 Channel Interference Effects

When modeling a real world application in a wind or water channel, in general the flow conditions are not exactly the same as in the cases of unbounded or near-ground flows. In our study, we are not modeling a real world application directly in the water channel. However, we need to take wall effects into account to control the conditions required for the investigation of the separation phenomenon.

The presence of the limitations of the test section at a finite distance produces several effects. Pope (1999) discusses each of these effects separately. Three of the effects that Pope introduced are important for our case: the so-called horizontal buoyancy due to static pressure gradients, solid blockage due to the model cross-sectional area and streamline curvature due to the influence of the walls of the test section.

Horizontal buoyancy refers to a force resulting from the variation of static pressure along the empty test section. This static pressure variation is due to the increasing thickness of the boundary layers along the channel walls and the free water surface in the case of our water channel. These pressure variations in general accelerate the flow. According to the boundary layer assumptions of Blasius, the boundary layer thickness, δ is proportional to $\sim\sqrt{x}$. In our case with developed boundary layers, the variation of static pressure inside the empty test section is negligible. The horizontal surface of the empty test section also indicates that this variation is negligible (less than 0,1 mm H_2O or 1 Pa).

The solid blockage effect is due to the ratio of the frontal area of the model with respect to the cross section of the test section. This ratio should be less than 0.05 to avoid blockage effects. For our case, the maximum blockage ratio is 0.14 which leads to an acceleration of the flow around the model. Since we are not interested in direct comparisons with unbounded flows, this effect is not corrected in this study.

Curvature of the streamlines is due to the finite dimensions of the test section. There is an induced upwash or downwash around the model depending on the configuration. This effect can be evaluated by using the image vortex method, which gives an approximation for ground proximity effect. The flow in the test section can be modeled by a uniform flow and a bounded vortex created as a result of the circulation around an airfoil. To represent the effect of the channel wall, an image vortex is placed below the channel wall at a distance a_1 from the wall. The effect of the free surface can be represented by placing a second image vortex at a distance a_2 above the free surface since during the experiments, it is observed that the free surface does not change its shape considerably due to the streamlines of the flow and the normal velocity across the free surface is zero. Figure 3.9 shows the circulation around the model and the mirror images of this circulation, with respect to the channel wall and free water surface.

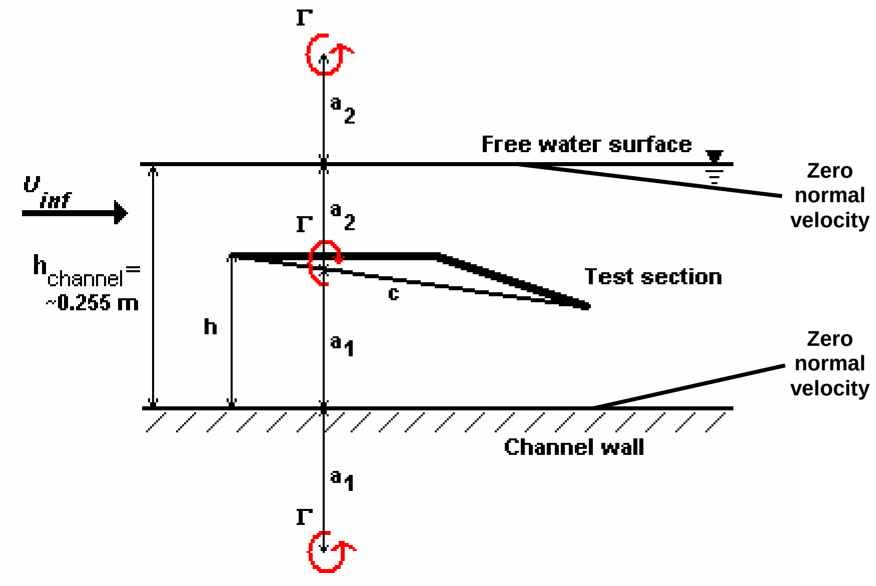

Figure 3.9: Schematic representation of tunnel interference effects. The proximity of the channel wall and the free water surface affects the flow around the model.

The image vortices act in two ways on the flow around the model. Firstly, they induce a streamwise velocity component around the model. The lower image vortex reduces the freestream velocity while the upper one increases this velocity. With the convention shown in Figure 3.9, this gives a change in circulation of:

$$\Delta\Gamma = \frac{-\Gamma_o}{4\pi a_1 U_\infty} \tag{3.1}$$

for the lower vortex and ,

$$\Delta\Gamma = \frac{\Gamma_o}{4\pi a_2 U_\infty} \tag{3.2}$$

for the upper vortex, where Γ_o is the circulation without wall interference and a_1 and a_2 are the vertical distances to the wall.

Secondly, the slip condition on the profile which is satisfied at ¾ of the chord c leads to an increase in circulation due to both image vortices [Katz, 1991]:

$$\Delta\Gamma = \Gamma o(\frac{c^2}{16a_1^2} + \frac{c^2}{16a_2^2}) \quad \textbf{(3.3)}$$

According to Kuethe (1986), for the total variation of the circulation, we obtain:

$$\Gamma = \Gamma_o\left(1 + \frac{c^2}{16a_1^2} - \frac{\Gamma_o}{4\pi a_1 U_\infty} + \frac{c^2}{16a_2^2} + \frac{\Gamma_o}{4\pi a_2 U_\infty}\right) \quad \textbf{(3.4)}$$

Thus, with $a_1 = a_2$ the net effect of ground is an increase in the circulation, resulting in an upwash at the leading edge (since $a_1 > a_2$). This upwash induces separation at the leading edge, requiring a greater suction rate at the leading edge of the model to attach the flow to the surface. The velocity vector map in Figure 3.10 shows the upwash created as by the circulation at 30^o of base slant angle.

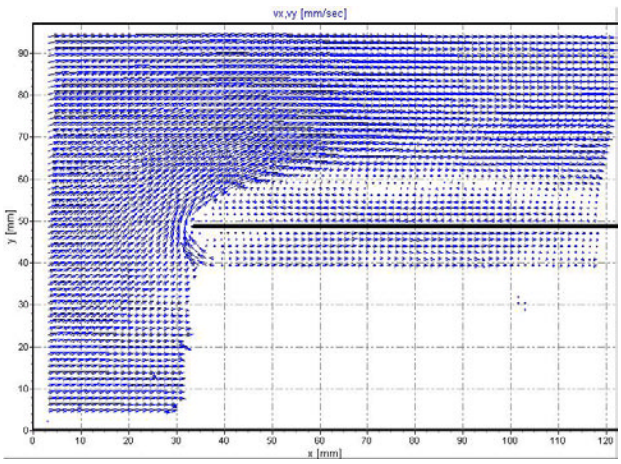

Figure 3.10: Time averaged velocity vector map showing the upwash and the separation bubble at the leading edge at 30^o of slant angle. U_∞= 6.4 ± 0.5 cm/s. No suction.

According to equation (3.4), changing the height of the model from the ground effects the circulation over the model. Figure 3.11 shows the effect of height on the circulation around the model for different slant angles. Here, height of the model from the channel ground is non-dimensionalized by the height of the channel.

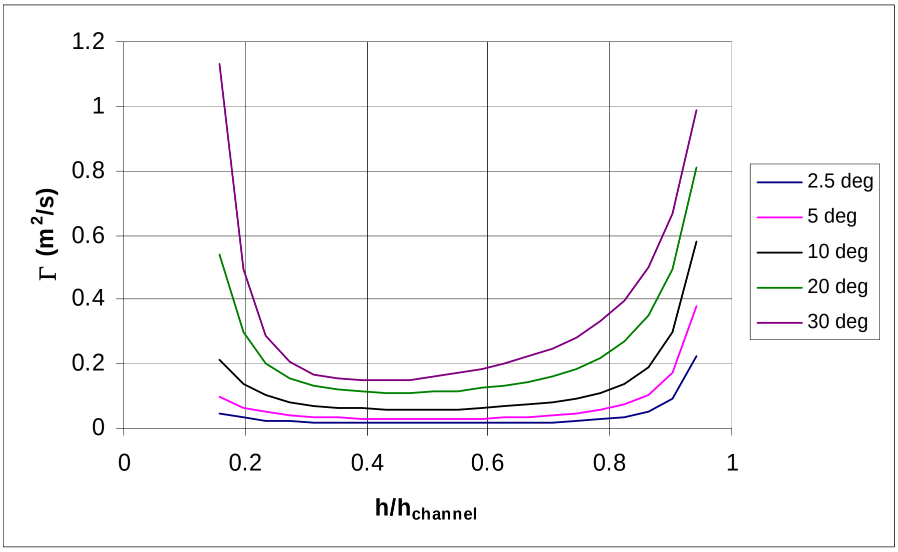

Figure 3.11: Variation of circulation with respect to the distance from the ground. Height of the model is non-dimensionalized by the height of the channel $h_{channel} = 0.255m$.

This figure indicates that the circulation around the model has a minimum when the distance from the channel ground is between 8 and 17 cm depending on the base slant angle. However this estimation is done assuming that there is no flow separation over the base slant. Therefore estimation for minimum circulation is valid for only small slant angles. As a compromise between height necessary to be able to reach high slant angles (~53^o) and the restrictions imposed by equation (3.4) we decided to place the model 17 cm above the channel ground to minimize the channel interference effects due to streamline curvature.

3.4 Suction System

The suction circuit is composed of the water-channel, the turbine meter and the submerged water pump. This turbine meter and the submerged pump are discussed separately in the following paragraphs.

3.4.1 Turbine Meter

To measure the suction rate, a measurement device was required upstream of the suction pump. The possible devices were venturi tube, orifice meter, rotameter or turbine meter. However, none of the available instruments in the laboratory were suitable for our setup. Therefore, a device has been manufactured for our specific requirements.

The specific requirements were:

1- The device must be adaptable to the 5 cm diameter PVC tube, ahead of the pump inlet.
2- The pressure loss across the device should be as low as possible, in order to avoid the reduction of the suction rate.
3- It should be read easily. A digital scale or a computer output might be an advantage for the ease of use.
4- Finally the ease of manufacturing was a very important selection criterion.

If we consider the venturi meter, it can not be manufactured easily because of the conical shape of its inlet and outlet. Moreover, the required length of the device is not suitable to use it in our arrangement. Similarly, rotameters are not easy to manufacture. Besides this, they need to be positioned vertically, which is not desirable in our arrangement. Although orifice meters are convenient to be fixed to our arrangement, high pressure losses created through the orifice prevents us using orifice meters. The alternative to these devices with less pressure loss and easier manufacturing process is a turbine meter.

Turbine meters are used for flow rate measurements of both liquids and gases. Inside the measurement device, flow passes through a free-turning rotor, mounted coaxially on the body centerline. The angular velocity of the rotor is proportional to the flow rate. Since no rotor is without friction, the friction across the rotor and the friction of the bearing system make it necessary to calibrate the device [Upp, 1993].

As flow through the turbine first increases from zero, a certain flow rate exists before the rotor begins to turn. At some point, the torque produced by aerodynamic forces is big enough to overcome the moment due to friction. At this point, the rotor begins to turn and the friction moment reduces, since the dynamic friction coefficient of the bearing is smaller than its static friction coefficient. Because of this friction force, the calibration curve does not pass from zero. The aerodynamic torque, controls the rotor speed.

Advantages of turbine meters are good accuracy and repeatability in the measurement range and direct electronic output at high resolution rate which can be transferred to a computer. Irregularities in the signal can be reduced by averaging.

It has also some disadvantages which are, low reproducibility and accuracy at low flow rates and the requirement of homogeneous pipe flow, upstream of the device. To obtain this flow-pattern, long inlet pipes are required.

The manufactured device is composed of a turbine with 42 mm diameter and 8 blades. It is free to rotate over a shaft which is designed with Teflon bearings to create low friction. The turbine is placed into the center of an 80 mm outer diameter and 44 mm inner diameter Prespex cylinder. The entrance and exit diameters of the instrument are 50 mm to fit the pipes, used in the experimental setup. Figure 3.12 shows the manufactured turbine meter.

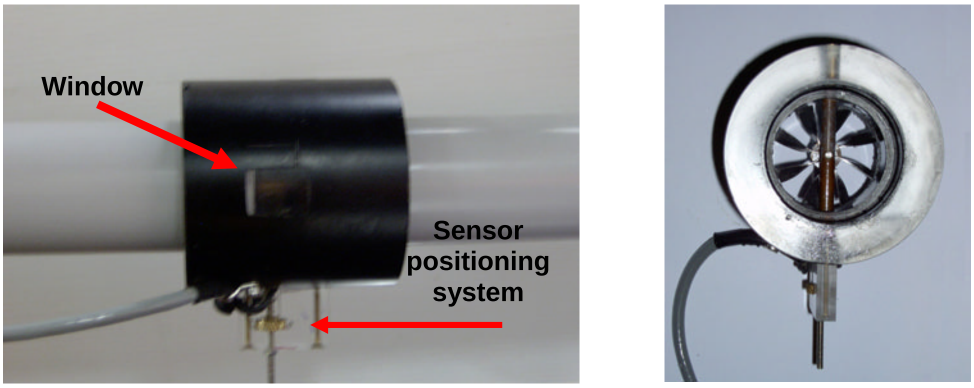

(a) **(b)**

Figure 3.12: Manufactured turbine meter. **(a)** Side-view. The window allows the control of the rotation. **(b)** Rotor inside the housing.

The measurement of angular velocity of the turbine is performed with an opto-electronic sensor. It is directed towards the turbine blades and measures the light reflected from the edge of the blades. The electrical circuit creates a rectangular signal each time a blade passes in front of the sensor.

The signal is transferred to a computer through the serial port to calculate the frequency of the rotor. This frequency can be averaged with respect to time and mean deviation can be calculated continuously.

Figure 3.13 shows the screenshot of the software called “Flowrate”. It allows adjusting the flow rate by counting and averaging the number of passing turbine blades.

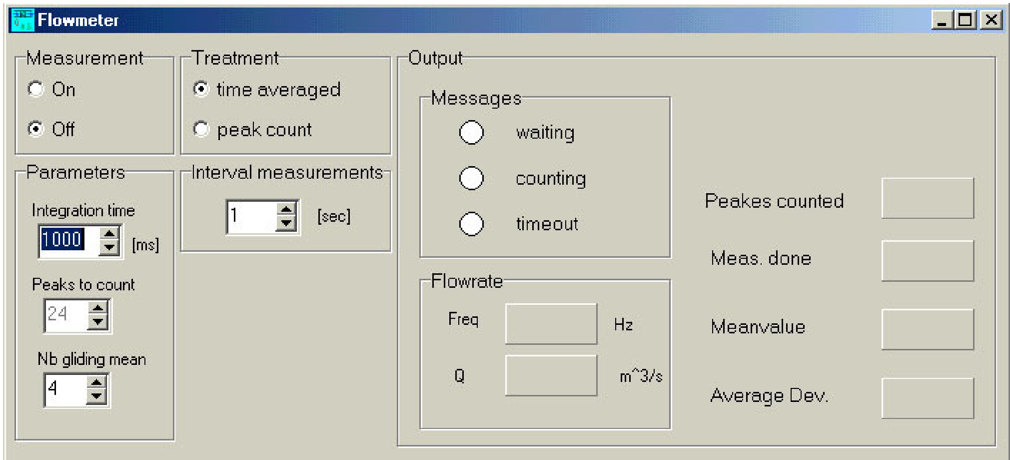

Figure 3.13: Screenshot of the “Flowrate” software, developed by A. Spohn.

The calibration was done by measuring the real flow rate with a balance. For this calibration process, a pump is required to supply water with a constant flow rate. To achieve this constant flow rate, the pressure upstream of the pump has to be constant. This means that the water level of the tank from which the pump sucks water off must remain constant in time. The easiest way to achieve this is to use a very large suction tank so that the change in water level during the pumping process is negligible with respect to the level of water above the pump inlet. This requires a big water tank, in which the water surface area is very large. The only tank that we had with these properties was the water channel. The complete arrangement used for calibration is shown in Figure 3.14.

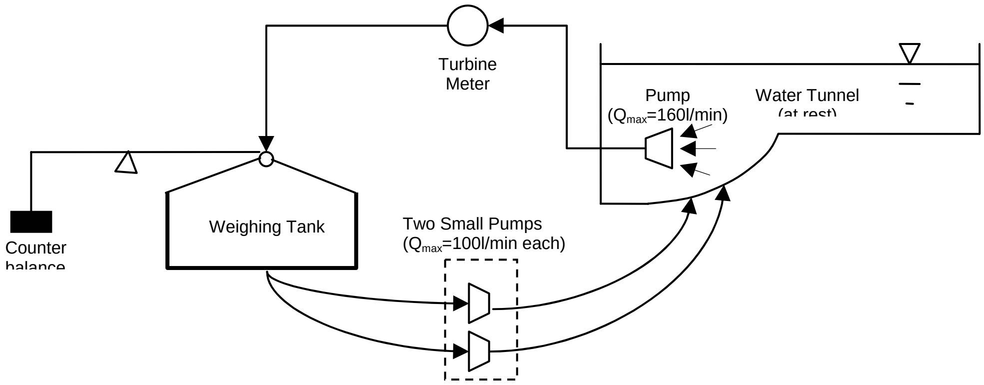

Figure 3.14: Turbine meter calibration setup.

The weighing tank in Figure 3.14 is a part of the "Hydraulics Bench" which is intended to provide facilities for performing a number of simple experiments in hydraulics for students. The tank is below the bench and the water discharged from the apparatus being tested on the bench may be filled into it to measure the flow rate. There are two opto-electronic switches, which measure the time needed for the weight of the water to compensate the imposed counter balance. For the calibration process, we used 22.5 kg of weight to counter balance the water filling inside the tank. To be able to use the arrangement for several successive measurements, the water coming of the weighing tank must be pumped back into the channel continuously. To compensate the flow rate of the pump in the water channel with 160 l/min maximum flow rate capacity (MARINA TF 400/S), two small pumps of 100 l/min capacity each (MARINA STG 250) were branched in parallel.

For calculation of the flow rate, the density of the water is approximately taken as 1000 kg/m^3 as we were not very far from normal conditions (T_w=23.3^{o}C, T_{air}=22.4^{o}C). If we call the volumetric flow rate Q, then:

$$Q = 22.5\frac{1}{\rho .t}\left[m^3/s\right] \tag{3.5}$$

where t is the time required to fill the tank and ρ is the density of the water.The resulting calibration curve is given in Figure 3.15:

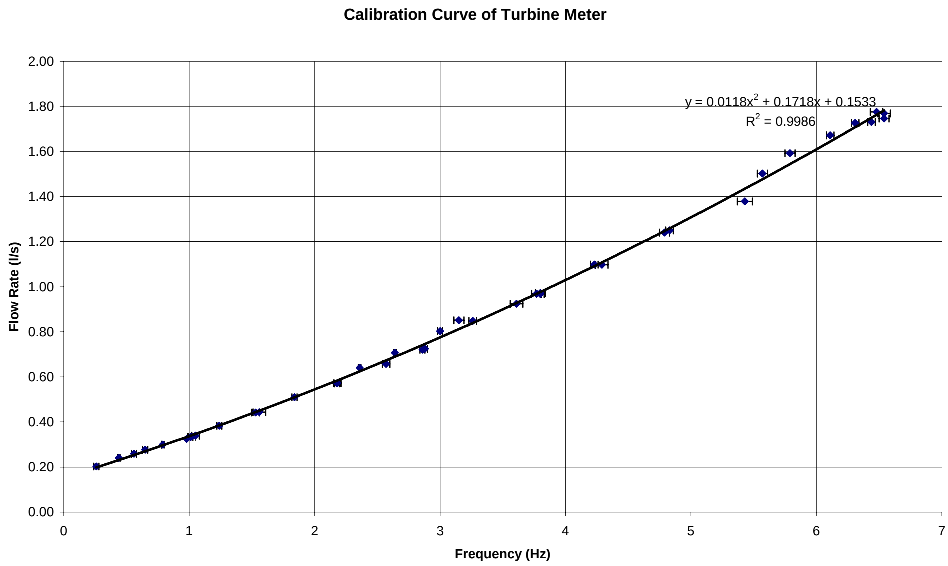

Figure 3.15: Calibration curve of the turbine meter.

The equation of the calibration curve is:

$$Q = 0.0118f^2+0.1718f+0.1533 \tag{3.6}$$

The lower part of the curve is non-linear. However, the upper part is quite linear as typical for turbine meters [Upp, 1993].

3.4.2 Suction Pump

In the previous experimental investigations, there were some shortcuts coming from the suction system as well. Firstly the pumping system was not sufficient to apply required suction for more than 20^o of base slant angle because of the suction slit efficiency and the limited power of the suction pump. Secondly, the suction rate was fixed. There was no control on suction rate.

To improve the suction rate, the suction pump is changed. The current suction system is using a MARINA TF 400/S type submerged water pump (Figure 3.16). The pump has

160 l/min pumping capacity. It's power is 400 W with 2800 rev/min. It's water head is 6 m.

Figure 3.16: Suction pump

The pump, which is normally a submerged radial pump, is used by connecting it directly to the suction channel. A secondary connection allowed at the beginning of each experiment to push the air out of the suction system. The yellow pipe shown in Figure 3.16 is this secondary connection.

To control the flow rate of the pump, a regulator tap (GEORG FISCHER 314 type PVC tap) is installed at the exit of the pump. It is an industrial usage type tap which allows precise control of the flow rate (Figure 3.16).

3.5 Acquisition system

One of the most important requirements of flow visualization is the ability to capture high quality images. To obtain such high quality data, both high quality instruments and careful arrangement of the equipment is required. Two types of recording devices are used in this study. First a SONY CCD-TR3200E Hi8 analog video recorder, second a IMASYS JAI CV-M1 model CCD digital camera. The output of the analog camera is digitized by using

PINNACLE (PC Vision) frame grabber card in order to convert the analog data into digital data for storage in a computer.

3.5.1 Analog Camera

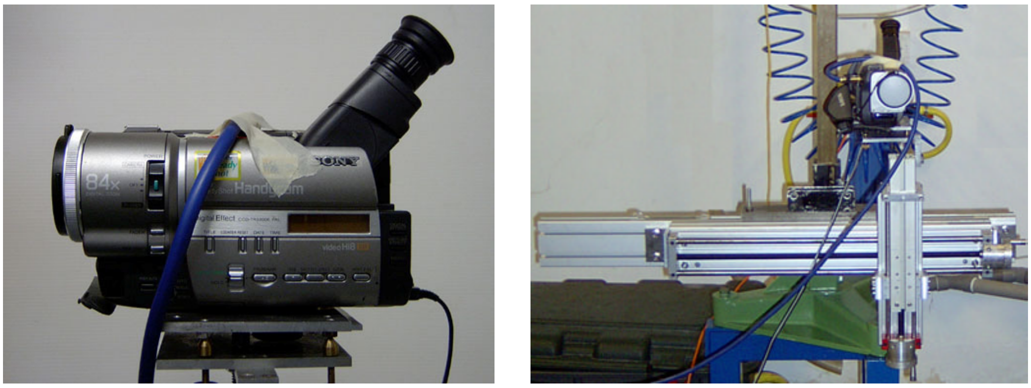

Figure 3.17: Sony CCD-TR3200E Hi8 Analog Camcorder and the two-axis camera positioning system.

Sony CCD-TR3200E Hi8 analog camera is one of the devices that we used for image capturing (Figure 3.17). This is a commercially available camcorder. It has 21x optic zoom. The shutter time can be modified between 1/3 to 1/10000 seconds. It allows capturing images by using a CCD sensor and recording them to 8mm tapes in Hi8 format. The camera captures 25 frames per second. Each frame consists of two blended fields with a time phase of 1/50 seconds. Hence, the frames must be de-interlaced to be used for measurements. The de-interlacing process is explained in more detail in chapter 4. By using a frame grabber card, the analog output of the camera is transferred to digital data and stored in a computer. The frame grabber card transfers the images to 24 bit, 256 color, 768 x 576 pixel digital images. The digitized video data are in *.avi (audio video interleave) format. For electrolytic precipitation and hydrogen bubble techniques the output of this camera is quite successful although the optical lens quality is not free of distortion. For PIV measurements, both the pixel resolution and the optical lens quality are not satisfactory. The distortion at the edges of the picture is high with respect to the CCD camera (about 4 % distortion in the x-direction). Hence, the measurements using this lens might cause measurement errors in PIV technique.

3.5.2 Digital CCD Camera

The term CCD stands for charge-coupled device. A CCD camera comprises an array of detectors called pixels. Each pixel is a MOS capacitor (a capacitor created by a metal and a semiconductor separated by an insulator), being charged by converting incident photons of light into electrons, like in a photo-diode. Light falling on a pixel is thus converted into an electronic charge. The charge on the individual pixel is transformed to a voltage during read-out of the CCD chip and the value of the voltage is seen as gray scale distribution on the image.

The JAI-IMASYS CV-M1 CCD camera is used for our experiments. This model is a 1.3M pixel, 8 bit grayscale CCD camera. The output of the camera is 1296x1026 pixel digital images in *.tif (tagged image file) format. It captures 12 frames per second. There is a computer controlled DISPLAYTECH Ferroelectric-liquid-crystal-light-valve (shutter) in front of the camera. The optical lens of this camera is a SIGMA 180mm 1:2.8 objective (Figure3.18) with no measurable distortion at the edge of the images.

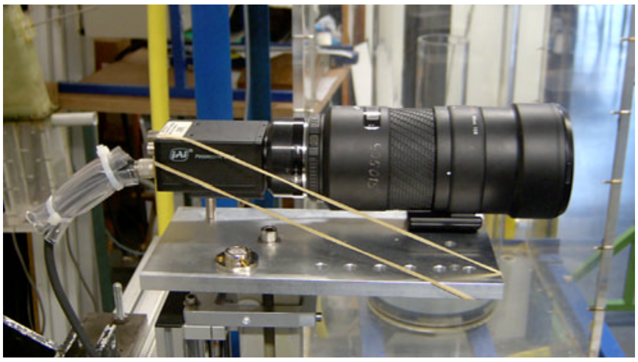

Figure 3.18: JAI IMASYS CV-M1 CCD Camera with SIGMA 180mm objective.

3.6 Illumination Equipments

There are two illumination equipments used in the experiments: white halogen light and laser light. For the hydrogen bubble technique and the electrolytic precipitation technique, white light is used. Argon Laser light sheets are used for some experiments with the electrolytic precipitation technique and in particular the PIV measurements.

The halogen white light projector is used for illuminating a large region inside the test section. Three light bulbs with 50W are arranged in line. The voltage required for the projector is 12V for security reasons. It is fixed over a tripod with a flexible arm, which allows the projector to move in every direction. Figure 3.19 shows the arrangement of the projector light.

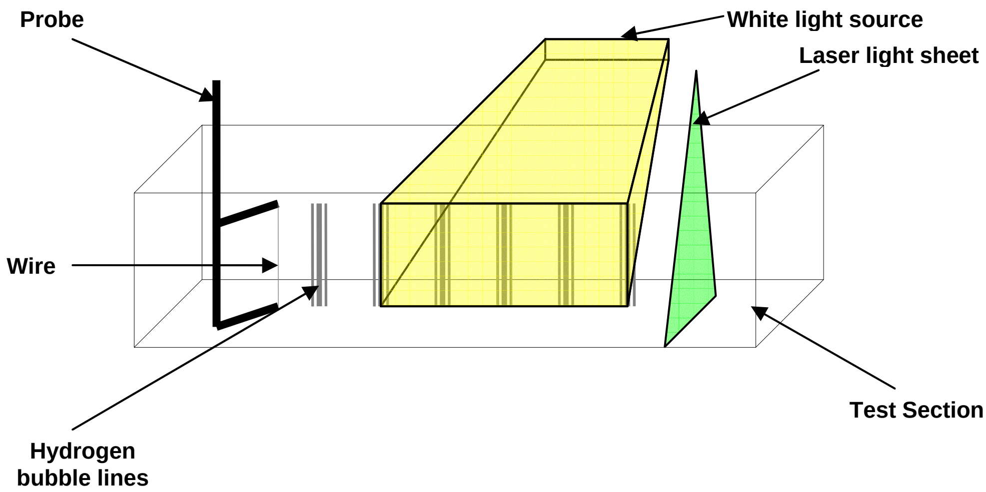

(a)

(b)

Figure 3.19: (a) Schematic drawing of the illuminating system. **(b)** Halogen lamps and the flexible tripod, used for the illumination of the hydrogen bubbles.

For PIV visualizations and some electrolytic precipitation visualizations only a plane needs to be illuminated with an intensive light sheet. For this purpose, a PERFORMA SPECTRA PHYSICS, 165-05 UV, 5W Argon laser with 40A current in combination with a cylindrical lens is used. The laser light is carried to the test section through an optical fiber. It is possible to minimize the thickness of the light sheet to about 1 mm. The laser produces a continuous light sheet with a maximum of 4.6W power. Figure 3.20 shows the argon laser device.

Figure 3.20: PERFORMA SPECTRA PHYSICS Argon laser and fiber branching.

CHAPTER 4

VISUALIZATION AND MEASUREMENT TECHNIQUES: THE HYDROGEN BUBBLES, THE ELECTROLYTIC PRECIPITATION AND THE PARTICLE IMAGE VELOCIMETRY

4.1 Introduction

Many fluid flow investigations require non-intrusive methods to investigate flow fields with minimal perturbations. Examples for such methods are the hydrogen bubble technique, the electrolytic precipitation technique and the particle image velocimetry (PIV). In this chapter, these methods are described. The details of the hydrogen bubble technique, which is used for both qualitative and quantitative measurements, are presented in the first section. In particular, the bubble generation procedure, the illumination technique and the data reduction procedure are discussed. The electrolytic precipitation technique, which gives complementary qualitative information in the near wall region, is discussed in the next section. Finally the principles of the employed PIV technique are described at the end of this chapter.

4.2 The Hydrogen Bubble Technique

The details of the hydrogen bubble technique are given in the following. First the basics of the technique are given. Then the data reduction process is described.

4.2.1 Hydrogen Bubble Flow Visualization Technique

The hydrogen bubble technique is used for both qualitative and quantitative flow visualizations of water flows. If two electrodes are introduced into a water flow and a DC voltage is applied, hydrogen bubbles and oxygen bubbles are formed at the cathode and anode respectively. Since oxygen bubbles are bigger than the hydrogen bubbles, only the hydrogen bubbles are used as the tracer particles. According to Schraub et al (1965), this technique was first introduced by Geller and then further developed by Smith & Clutters in 1961. It is still a very attractive technique for many flow situations since it allows production of bubbles at a controlled rate at nearly any desired position in the flow.

A schematic drawing of the whole hydrogen bubble generating system, including the DC power supply, computer, electronic circuit and the electrodes is shown in Figure 4.1.

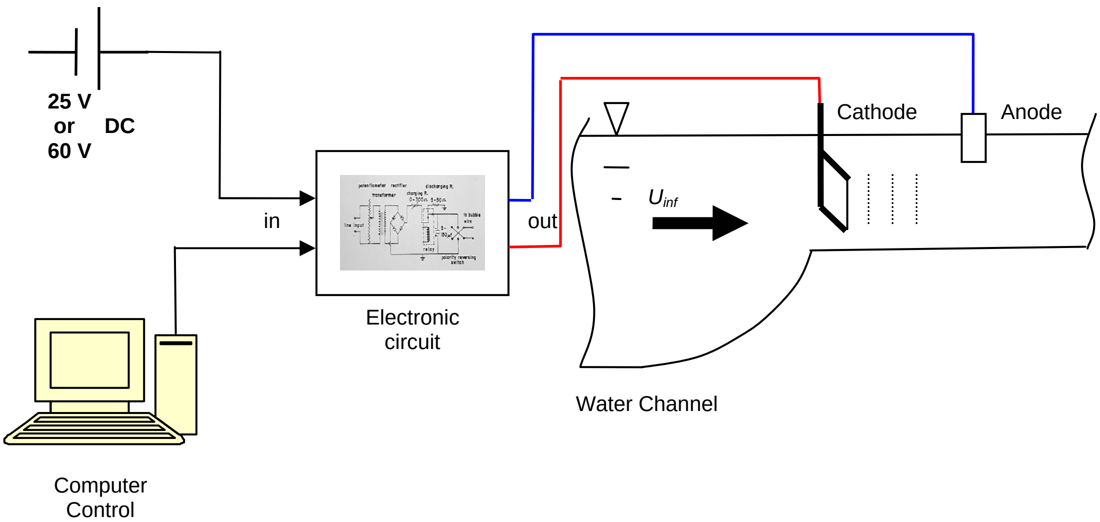

Figure 4.1: Schematic drawing of the hydrogen bubble generating system. The system is controlled by a computer program to allow a flexible variation of the bubble frequency between 0.5 and 20 Hz and the duty cycles between 10 % and 100 %.

In a conventional arrangement, a thin wire, which is used as the cathode of a DC circuit, is placed into the flow under investigation. Due to corrosion and fragility aspects platinum, copper or stainless steel is used as the wire material. The stainless steel wires are stronger and easier to handle. Platinum is usually preferred because it does not corrode and it appears to accumulate dirt less rapidly. However, it is about 50 times more expensive than the stainless steel wires. Therefore, we used stainless steel wires with 0.05 mm diameter in our experiments. A stainless steel plate was placed downstream along the channel wall as anode.

The greatest difficulty of this method is to control the “bubble quality”. During the operation, the timing of the voltage pulses with sharp on-off characteristics of the circuit, are very important to obtain high quality bubbles. A schematic drawing of the circuit, which is employed for bubble generation, is shown in Figure 4.1.

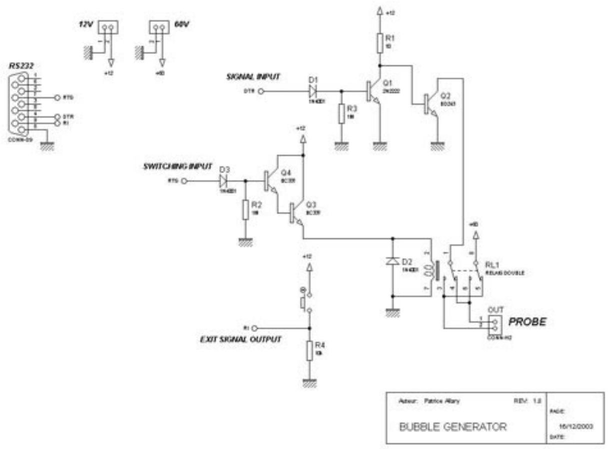

Figure 4.2: Schematic drawing of the bubble producing circuit.

This circuit was connected to a computer through a data acquisition card. The timing and length of the pulses are controlled by a software, called “Bubblegenerator” developed in the laboratory. The screen shot of this software is given in Figure 4.3.

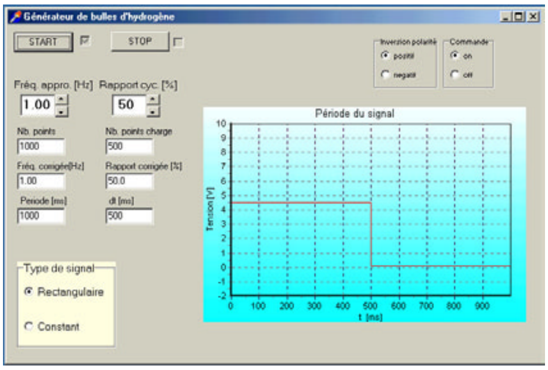

Figure 4.3: The screenshot of the "Bubblegenerator" software, which allows to control the bubble generation.

Although the bubble diameter may vary from half the wire diameter up to the wire diameter, according to a rule of thumb established by Schraub et al (1965), the bubble size is of the order of the diameter of the generating wire. However, more precisely the bubble size also depends on other parameters, e.g. on the conductivity of the fluid and on the applied voltage. Irregularities over the surface of the wire can lead to the local production of oversized bubbles.

Usually in hard tap water, no added electrolyte is needed. In softer waters, some additives such as sodium sulphate or NaCl, can be used to increase conductivity of water to improve bubble quality and the bubble generation. Since the tap water in Poitiers is hard enough, we used no additives for our experiments.

Voltages of up to 100V are required to obtain a sufficient optical density of the bubbles which is necessary for good image contrasts over appreciable distances. In practice the required voltage is a function of the electrolyte concentration, the distance between the electrodes and the geometry. The circuit that was used in our experiments was able to apply either 25 or 60 V to the wire. Unfortunately, with 60 V voltage, it is difficult to eliminate oversized bubbles. Some large bubbles are almost always formed and rise too rapidly to give accurate streak-surfaces. Therefore, in continuous mode we used only 25 V, while for short triggered pulses, 60 V were used. In this way the formation of bigger bubbles could be almost completely suppressed.

Much more troublesome than the few larger bubbles was the lack of repeatability of bubble formation under apparently constant conditions. Most wires require “aging” under operation conditions for a few minutes before they will produce bubbles uniformly. Some wires produce more uniform and smaller bubbles than others for no known reason. Some water compositions give better, that is, smaller and more uniform, bubbles than others. Sometimes a wire which has worked satisfactorily begins erratic bubble formation for no apparent reason. When this occurs, reversing the polarity on the wire for a few minutes will often solve this difficulty. For this reason, the circuit in Figure 4.2 contains a switch to inverse the polarity of the output voltage. The wire needs to be cleaned by acetone or thinner from time to time. Unfortunately, this is not always enough to solve all the problems. Problems of bubble control make the method somewhat tricky.

Since hydrogen is soluble in water, the bubbles produced by the wire dissolve; this has both advantages and disadvantages. The primary advantage is that no pollution occurs in closed-circuit flows. The disadvantage is that the half-life of the bubbles is very short (depends on flow conditions and size of the bubbles but under laminar conditions, roughly 3 s. For a velocity of 10 cm/s this corresponds to a distance of 30 cm over which the bubbles can be observed. Turbulence dissolves the bubbles even more rapidly [Schraub et al, 1965].

Hydrogen bubbles that are produced at the cathode wire are carried away with the flow and attain the flow speed about 70 wire diameters downstream [Schraub et al, 1965]. However, owing to buoyancy, the bubbles necessarily rise in the flow during their motion since the density of the hydrogen bubbles is about 1000 times less than the density of water. It is desirable to have their rise rate as low as possible, to obtain more accurate velocity measurements. Therefore, bubbles with smaller sizes, but still enough surfaces for light reflections are preferred for visualizations.

The terminal rise rate of the bubbles, due to the buoyancy forces may be approximated by using Stoke’s solution for solid spheres, since the Reynolds numbers based upon bubble diameter is very small. The resulting equation for the final velocity is given by Schraub (neglecting the motion inside the bubbles);

$$v_T = \frac{1}{18}\frac{\rho_{H_2O} - \rho_{H_2}}{\mu_{H_2O}} g d^2 \qquad \textbf{(4.1)}$$

For the bubbles, with 0.05 mm diameter (At 20^{o}C ρ_{H2O}=1000 kg/m^3, ρ_{H2}=0.86 10^{-1} kg/m^3, μ_{H2O}=10^{-3} m^2/s) the terminal rise velocity of the bubbles is:

$$v_{Tmax}=1.36\ \ 10^{-3}\ \mathrm{m/s}$$

This terminal rise velocity corresponds to a rise rate Reynolds number of 0.068 << 1.0, which is low enough for use of the Stoke's flow around the bubble. Clearly, the assumption of low Reynolds number holds.

In the above calculations, the bubble diameter used is in fact the maximum bubble diameter. Hence, the bubble rise, calculated in this way is the maximum possible bubble rise rate. For comparison, the terminal rise velocity of the bubbles with minimum size is:

$$v_{Tmin}=3.4\ \ 10^{-4}\ \mathrm{m/s}$$

In order to test the effect of the bubble rise, we measured the bubble rise rate and compared it with the result of the formulation, given by Schraub et al (1965). The channel velocity was 8.6 ± 0.5 cm/s. Hydrogen bubbles are generated from a horizontal 0.050 mm thick wire. The applied tension was 60 V and bubbles were generated continuously to simulate the worst possible case.

Figure 4.4 shows the path of the bubble sheet, which progresses with an inclination of ~0.2^o with respect to the horizontal.

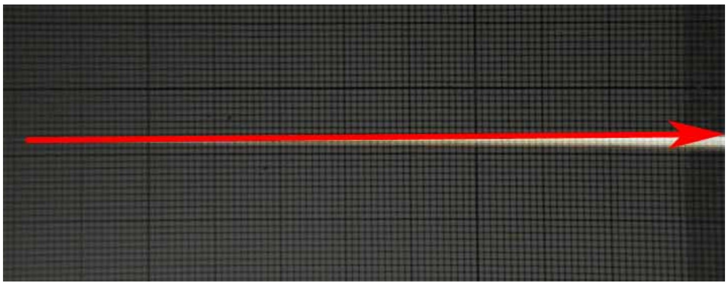

Figure 4.4: Hydrogen bubbles, generated over a horizontal plane to measure the bubble rise. The red arrow shows the direction of the bubble motion. The inclination of the bubble sheet is about 0.2^o

With the flow velocity of the experiment, the rise rate according to Schraub gives an angle of 0.9^o while for the minimum bubble diameter of 0.025 mm, this angle is reduced to 0.2^o. This shows that the measured bubble rise, is inside the calculated range. However, for such small angles, the measurements must be very precise. Since it is not possible to measure the exact bubble diameter easily, the measurements at least show that the estimated bubble diameter is reasonable. Moreover, even the maximum bubble rise rate of 1.36 mm/s represents only about 1.6% of the channel velocity (8.6 ± 0.5 cm/s). Therefore, the bubble rise can be considered as negligible in most of the cases that we are concerned in this study.

It should be noted that the bubble rise rate may change if the wire is positioned vertically instead of horizontally. This is because of the interaction between the rising bubbles. The velocity induced by a rising bubble might increase the rise rate of the bubbles coming from below. In addition, while working with vertical wires, isolated bubbles might merge leading to larger bubbles, which rise more rapidly.

Effective illumination does not rely simply on a strong light intensity. The quality of the visualization strongly depends on the angle of light incidence on the bubbles. Furthermore, a black background turns out to be very important to obtain a high contrast for the captured images. A non-reflecting material such as felt proved to be very useful to avoid unnecessary reflections.

The optimum angle for lighting with respect to the optical axis of the camera or viewer should be 115^o [Schraub et al 1965]. This angle is a result of refraction of light through the water-hydrogen and hydrogen-water interfaces. Also the distance between the bubbles and the light should be arranged regarding the required light conditions. Increasing the distance between the bubbles and the lamp gives a better distribution of the light on all bubbles but the intensity of light becomes less. Placing the light source closer gives a higher intensity of light but with a reduced cone of light illuminating only a smaller area of bubbles. Also the fringes between the individual lamp bulbs become apparent on the illuminated segments of the streak surfaces. It is necessary to find a compromise between intensity and extensions of the illuminated section in order to arrive at the optimum arrangement for the light source. The details of the white light projector which was used for hydrogen bubble visualizations are explained in section 3.6.

Another problem associated with lighting is the heating of the water at the upper level of the test section near the light bulbs, causing convection currents that interfere with the flow. One solution of this problem is to introduce a small amount of common domestic washing up liquid on the surface of the water, which helps breaking the surface tension and allows the interface to move thus reducing thermal convection currents. This method can be applied if disturbing effects of heating becomes considerable. A special glass to filter the heat is also a solution.

4.2.2 Data Reduction Process

Data reduction process is the most time consuming part of hydrogen bubble technique. During the experiments, the images of the flow field are taken by an analog camera. These images are transferred to the computer through a frame grabber card which digitizes the images. The data stored in the computer at the end of an experiment are digital images, in the form of movies (Audio Video Interleave format-*.avi) or single picture frames (bitmap format-*.bmp).

The movies, which are stored in the computer contain 25 images (frames) per second created by combining 50 half images (fields) per second. Each image is created by combining and capturing two consecutive half-images.

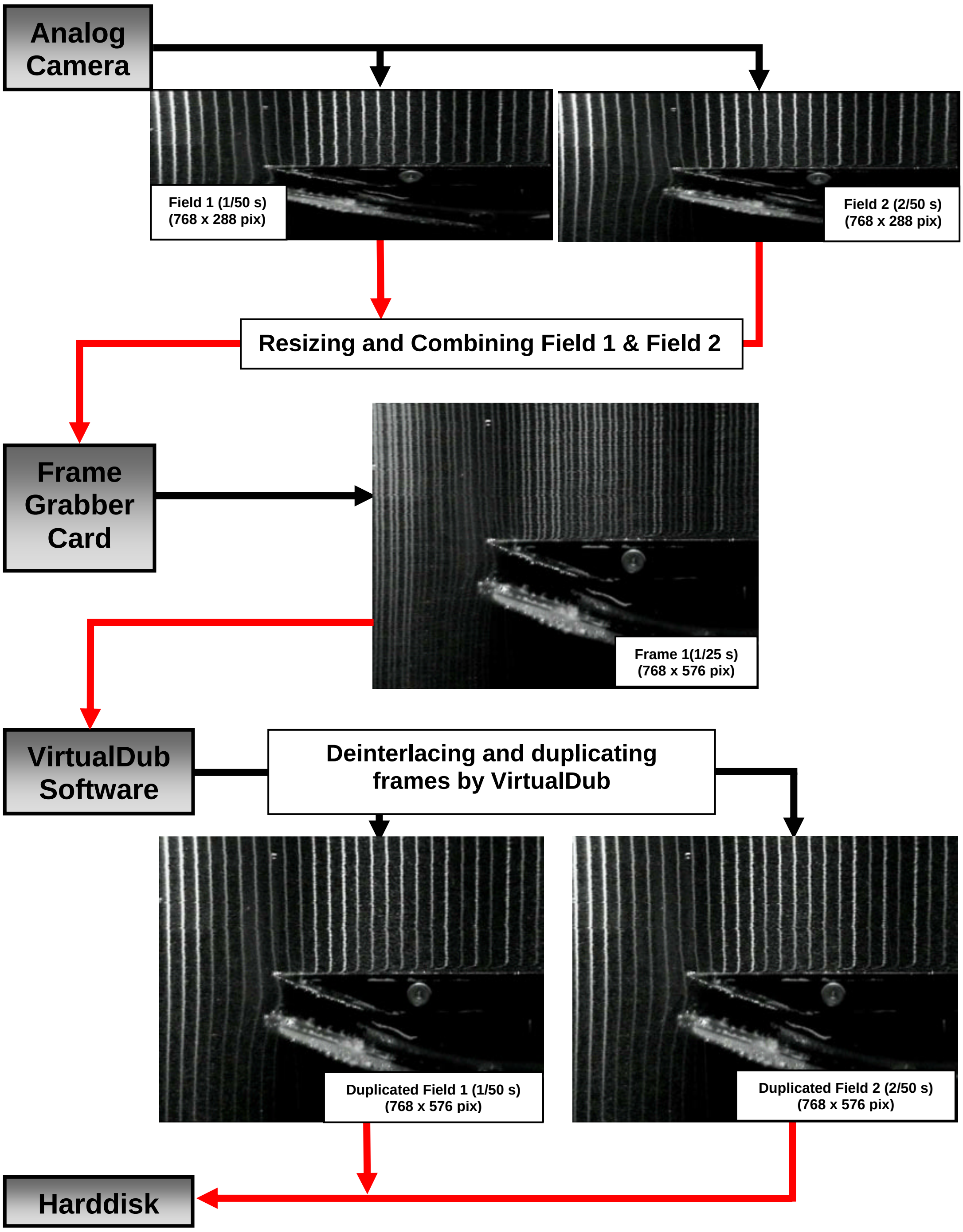

Figure 4.5 : Schematic representation of the image capturing and deinterlacing process. The two fields coming from the analog camera are resized and combined in a single frame by the frame grabber card. To obtain information on the motion of hydrogen bubbles, this frame is deinterlaced and the timelines of the corresponding two fields are duplicated. Each frame gives information about the flow field with a 1/50 s time interval. Black arrows in the figure show outputs and red arrows show the inputs to the devices.

The order of image capturing process for a single frame using a digital video capture card is shown in Figure 4.5. The different steps are:

1- The frame grabber card digitizes the first half-image, called field 1 of the first frame (t=1/50s).
2- Digitizes the second half-image, called field 2 of the first frame (t=2/50s).
3- Resizes and combines fields 1 and 2 together and creates frame 1 (t=1/25s).

Deinterlacing of the images is done with the help of the "VirtualDub 1.4.13" software. It is a video capturing and filtering software for processing -*.avi formatted video files.

These movies and images provide qualitative flow visualization data of the flow field but do not provide any quantitative information about the flow velocity. This information can be obtained by analyzing the filtered images.

The time difference between two consecutive hydrogen bubble lines (timelines) in a single image are known from the bubble generation frequency. To be able to read the velocity information, hidden in this image, we need to find the distance between two timelines, so that we can obtain flow velocity by using the well-known equation:

$$Velocity = Displacement / Time \qquad \textbf{(4.2)}$$

From the digital images, we can find the distance between two lines in terms of pixels. If we have a scale, showing the distance in terms of millimeters, we can easily relate these pixels to the real distances in millimeters, to find the velocity. Figure 4.6 shows an example scale for the images filtered above.

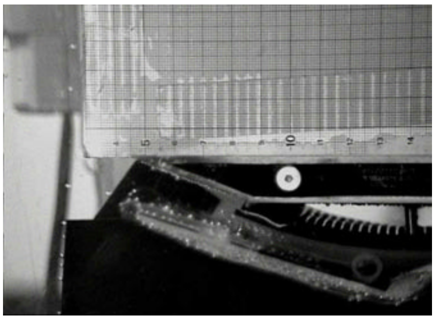

Figure 4.6: Scale for the hydrogen bubble measurements.

The scale must be well aligned with the model since it serves as reference for all measurements. It must be taken with the same camera position and zoom as used during the visualizations. For velocity measurement, the scale needs to be fixed to the image by using an image processing software. Figure 4.7*a* shows the digital image, which is ready for analysis.

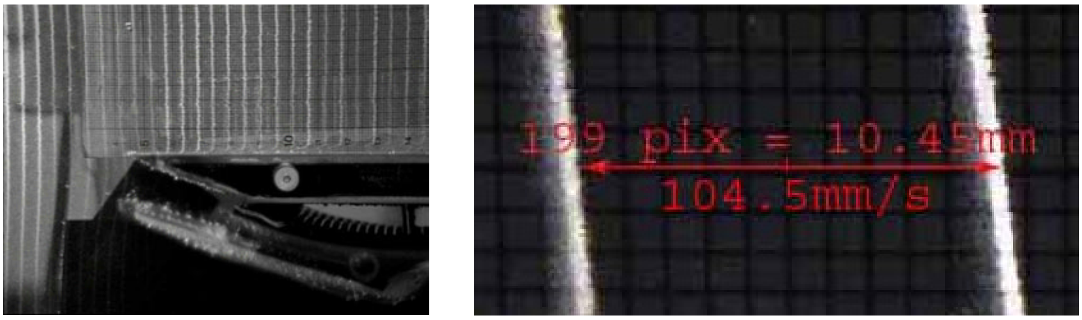

(a) **(b)**

Figure 4.7: Digital images showing the hydrogen bubble timelines and reference scale fixed to it. **(a)** The image, which is ready for analysis. **(b)** The image, zoomed between two timelines with an example of velocity calculation between two consecutive timelines, generated at 10 Hz with 13% duty.

In Figure 4.7*b*, a simple velocity measurement is performed. The velocity is measured between two consecutive timelines which were produced with 10 Hz frequency with 13% duty cycle at 8.6±0.5 cm/s tunnel velocity.

Knowing that the timelines has a thickness, which depends on the flow speed and the duty cycle, when measuring the distance in pixels, the distance should be taken either from starting of the first line to the starting of the second line or from end of the first line to the end of the second line. The distance between two timelines in Figure 4.7*b* is 199 pixels. In the neighborhood of this position, 381 pixels correspond to 20 mm and therefore, 1 pixel corresponds to ~0.0525 mm. Hence, the distance between two consecutive timelines is 10.45 mm. Using the frequency information, we obtain 104.5 mm/s of velocity. This velocity corresponds to the mean velocity, at the mid-point of the two lines.

As mentioned by Schraub (1965), even in extremely difficult measuring situations, this technique provides measurements of velocity within precision of 4 percent. More details on the precision of the measurements is given in Appendix A.

One of the major advantages of this technique for low-speed water flows is that it gives information of the flow structure and the velocity field at the same time. However, there are also some disadvantages. Firstly, the velocity range is restricted to about 30 cm/s of velocity [Schraub et al, 1965]. Furthermore, with the described procedure, only one component of the velocity at a point can be measured. For our study, we used hydrogen bubble technique mainly for determination of the Vx component of the velocity.

4.3 Electrolytic Precipitation Technique

The electrolytic precipitation technique can be used for visualizing water flows up to 15 cm/s velocity as shown by Taneda et al (1980). This technique produces a white powder from the precipitation of a solder wire strip (97% tin, 3% copper). The solder wire is fixed on the body surface in the zone, where the flow structure needs to be investigated. In our experiments, we have employed 3 to 4 mm wide, 0.08 mm thick solder wire strips. Figure 4.8 shows the schematic drawing of the electrolytic precipitation system.

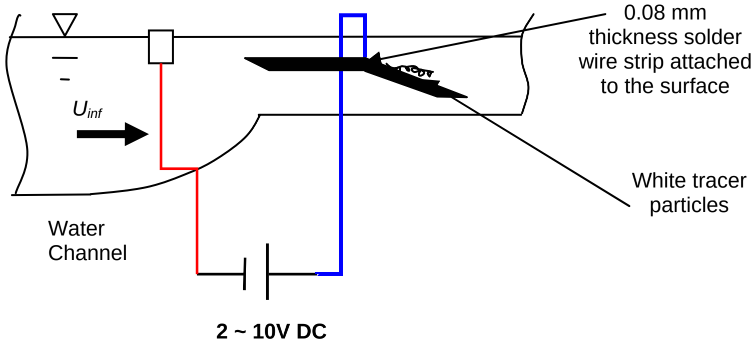

Figure 4.8: Schematic drawing of electrolytic precipitation system.

Applying a tension between the solder wire and another electrode which was positioned at a close distance from the model, results in the production of white precipitates due to electrolysis. Tensions as low as 2 V are generally enough to obtain the production of precipitates, but the process should be initiated by applying first voltages as high as 10 V for several seconds. Since the solder wire strip is only 0.08 mm thick, the produced particles are directly released on the wall. The particles thus, give information about the direction of the wall shear stresses and in particular on the separation of the flow from the body. Separation lines become visible by accumulation of tracer particles.

The white precipitated particles can not be observed clearly without proper illumination by a laser light sheet or white light. The lifetime of the solder wire is limited and using high tensions reduces the lifetime.

Figure 4.9 and 4.10 show the installed solder wire and an image with the tracer illuminated by a vertical laser light sheet respectively.

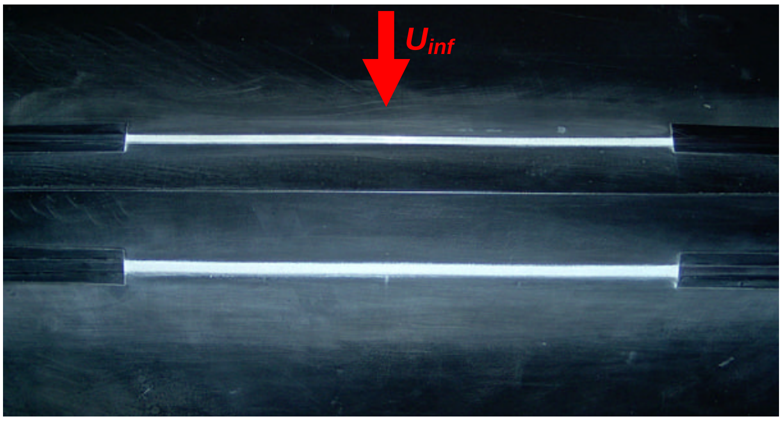

Figure 4.9: Two solder wire strips fixed upstream and downstream of the salient edge. These strips are used to detect flow separation and to visualize the flow inside the separation region.

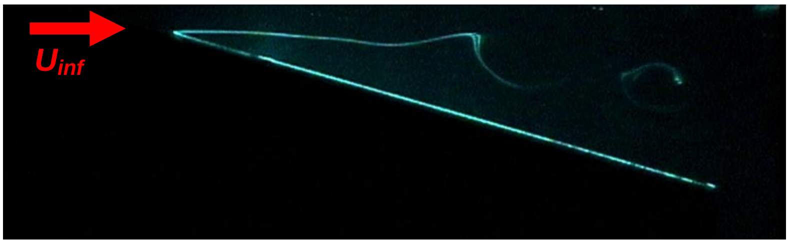

Figure 4.10: Flow visualization obtained with electrolytic precipitation technique. The vertical plane of symmetry of the model is illuminated by using a vertical laser light sheet of about 1 mm thickness.

4.4 Particle Image Velocimetry (PIV)

Particle image velocimetry (PIV), is an optical measurement technique, which works non-intrusively. In contrast to local measurement techniques by probes (pitot tube, hot wire etc.), the PIV technique allows to find the velocity information over the whole image at a given instant.

The idea of this technique is to record two successive images of the particle distribution in an illuminated plane of the flow and to deduce the displacement of the particles from these images. Figure 4.11 briefly explains a typical set-up for PIV recording in a wind tunnel.

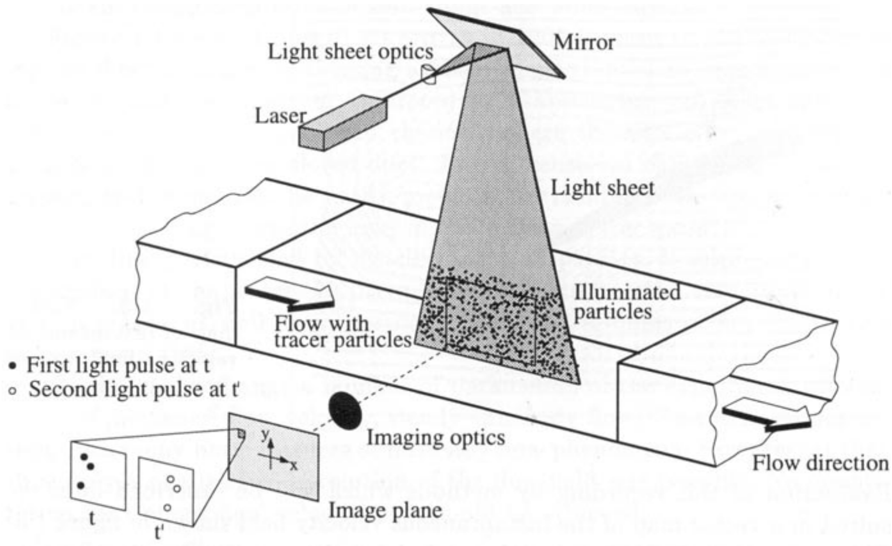

Figure 4.11: A typical arrangement of a PIV system [Raffel, 1998]

Before going into details of the PIV technique, some general aspects have to be discussed.

In PIV, it is not actually the velocity of the flow that is measured, but the velocity of particles suspended in the flow. In this respect, these seeding particles can be considered to be the actual velocity probes, and seeding considerations are thus important in PIV. The particles must be small enough to track the flow accurately, yet large enough to scatter sufficient light for the camera to be able to detect them. Ideally, the particles should also be neutrally buoyant in the fluid. Beside these properties, cheap, non-toxic, non-corrosive, non-abrasive, non-volatile (or slow to evaporate), chemically inactive, clean and easily generated particles are desired.

The tracer particles that we used are lycopodium particles, which are the spores of a medical plant. The average particle diameter of the lycopodium particles is between 20 and 35 μm.

The particles are illuminated by using a laser light sheet generated by the Ar-Laser described in Section 3.6. In a conventional PIV system, the light sheet is pulsed so that the particles are illuminated with instantaneous pulses and the images of the illuminated particles are recorded by a CCD sensor. CCD sensor may record two consecutive images to a single frame or two different frames. If they are recorded into a single frame, the image is processed by an auto-correlation algorithm. If they are recorded on two consecutive frames, then the images are processed by cross-correlation. However, in the system that we employed, the laser light sheet is not pulsed. Instead, an electromagnetic field shutter is used in front of the CCD camera to capture instantaneous images of the continuously illuminated particle plane. The images are recorded on two different frames and processed by cross-correlation.

For evaluation, the digital PIV recordings are divided in small sub-areas called “interrogation areas”. The local displacement vector for the images of the tracer particles of the first and second frame is determined for each interrogation area by means of cross correlation. It is assumed that all particles within one interrogation area have moved homogeneously between the two frames. The projection of the vector of the local flow velocity into the plane of the light sheet (2-component velocity vector) is calculated taking into account the time delay between the two frames and the magnification at imaging. The process of interrogation is repeated for all interrogation areas of the PIV recordings.

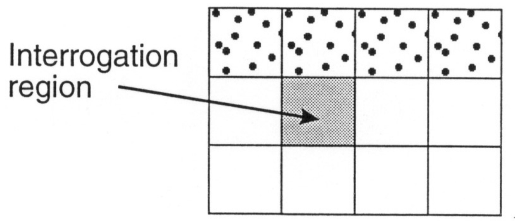

Figure 4.12: The digital PIV recordings are divided into interrogation areas.

No matter how many particles are inside the interrogation areas, there are generally some random correlations between the initial position of some particles and the final position of other ones. These random correlations can be considered as noise and in order to reduce their influence, several particle pairs within each interrogation region must show a higher correlation signal.

The size of the interrogation area at evaluation must be small enough so that velocity gradients have no significant influence on the results. Furthermore, it determines the number of independent velocity vectors and therefore the maximum spatial resolution of the velocity map which can be obtained for a given spatial resolution of the camera sensor. When selecting the interrogation area size, several aspects should be taken into consideration. To get a good signal-to noise ratio in the correlation function, the flow velocity within the interrogation area should essentially be homogeneous, implying that the smallest spatial scales you wish to resolve in the flow should be larger than the interrogation area size. This indicates that the interrogation area size should be as small as possible, while fulfilling the requirement of a minimum of 5 particles per interrogation area, as explained in the Dantec PIV system documentation [Dantec Documentation].

The dynamic range of the measured velocity values increases with larger interrogation areas. To maintain high measurement accuracy the maximum particle displacement between successive images should be less than ¼ of the size of the interrogation area. This indicates that the interrogation area should be as large as possible to get the largest possible dynamic range.

The conflicting interests stated above indicate that a compromise between spatial resolution and dynamic range of velocity has to be found. When selecting the interrogation area size you should also be aware of the following: The time required to process an interrogation area will increase with increasing interrogation area size. However, the number of interrogation areas that need to be analyzed will decrease. As a consequence, results of the PIV measurements are user-dependent. User should input the interrogation area size according to his requirements such as processing time, velocity resolution and accuracy of the measurement.

The above discussion about the interrogation area is based on obtaining maximum information from the available images. However, for better results, the number of particles should be as high as possible, no matter how big the interrogation area is. Figure 4.13 shows two examples with different particle densities. The corresponding PIV results are also shown in the same figure. The resolution of the vector map with high particle density is higher, since high particle density allows smaller interrogation areas and more correlations. Using the same interrogation area size in the image with less particle density (Figure 4.13*a*) or trying a second correlation results in errors.

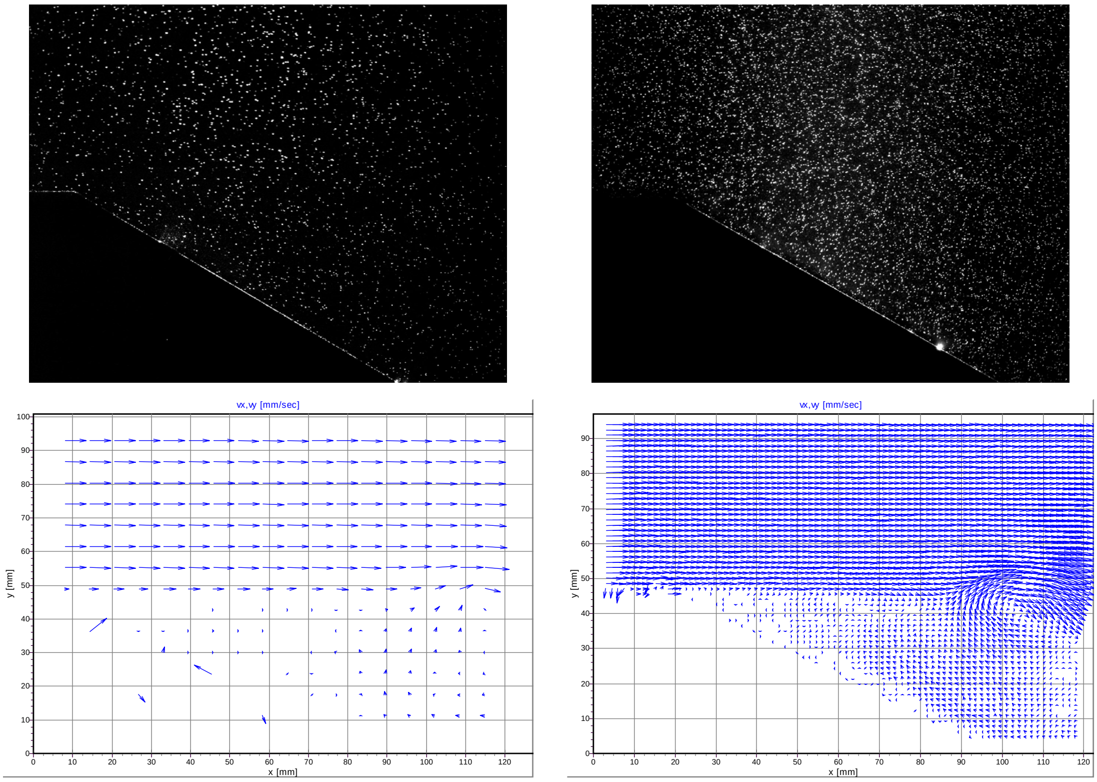

(a) **(b)**

Figure 4.13: Effect of particle density on PIV measurements. The particle density of the image on the left is clearly less than the particle density of the image on the right. This is also apparent in the vector maps. Higher particle density allows using smaller interrogation areas and more successive correlations.

By offsetting the second interrogation area (area in the second image) relative to the first, the range of measurable displacements is no longer symmetric about zero. In this way, all the particles inside the interrogation area of the first image remain in the same interrogation area in the second image. This process reduces the noise.

Near the interrogation area edges there is an increased risk, that either the initial or the final particle position will be outside the interrogation area. Thus, particles near the edges are unlikely to contribute to the velocity calculation. By overlapping the interrogation areas, the chance that all particle pairs become within at least one interrogation area is increased. In addition, the resolution of the vector map is increased.

For finding the correlations between recorded digital images, the software called “CIV” is used which was developed by A. Spohn. This software allows treatment of the images, finding correlations, plotting and processing the velocity vector maps. A screenshot of this software is given in Figure 4.14.

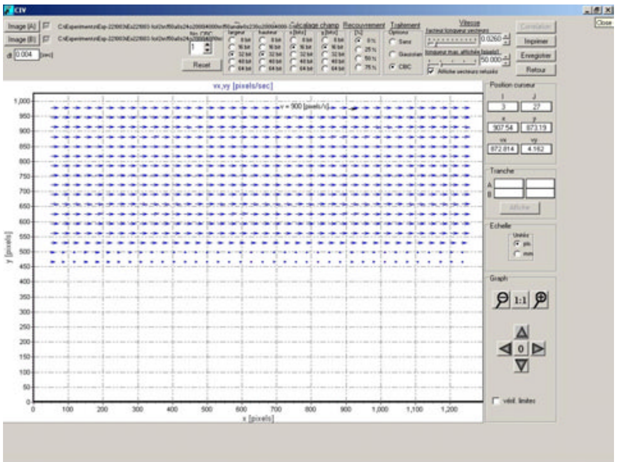

Figure 4.14: Screen shot of CIV software

The software is currently under development. However for low-speed water channel velocity measurements, the results are quite encouraging. It is possible to obtain whole field velocity measurements with spending less time and with less flow disturbance, with respect to many other methods.

One of the most important improvements in the software is the ability to estimate the wall boundaries and the velocity gradients close to the surface. For this purpose, there is an option in the software, called mirror. This option takes the mirror image of the region which is at the 70 pix neighborhood of the body surface of the first image (A) and pastes it to the second image (B). Then it does the same operation in the second image (B) (Figure 4.15). By mirroring the close neighborhood of the surface, it becomes possible to find more precise velocity gradients in the close neighborhood of the wall. As a result, the surface boundary, where the velocity is zero, can be estimated successfully.

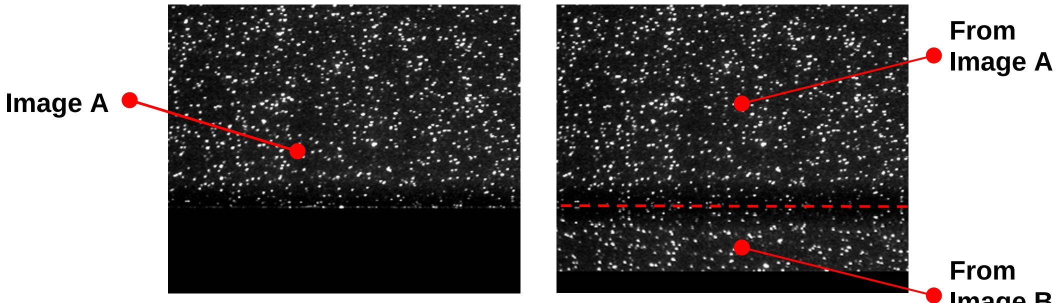

(a) **(b)**

Figure 4.15: (a) image A without mirror **(b)** image A with mirror.

Figure 4.16 shows the comparison of two analyses by using either no mirror or mirror options. In Figure 4.16*a*, which corresponds to the case without the use of the mirror option, the wall boundary is not clear since the velocity profile does not pass from zero. However, in Figure 4.16*b*, the y position where the velocity is zero is clear. This point corresponds to the wall boundary. The velocity data, above and below this point are opposite in sign but almost equal in magnitude because of the mirroring process.

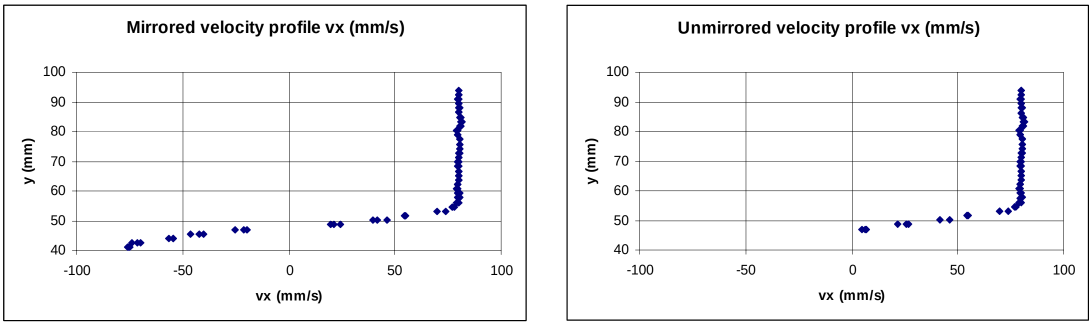

(a) **(b)**

Figure 4.16: Velocity profiles for mirrored and unmirrored PIV correlations at the same position.

When the mirror option is utilized, PIV results show some velocity vectors inside the mirrored region of the image (Figure 4.17).

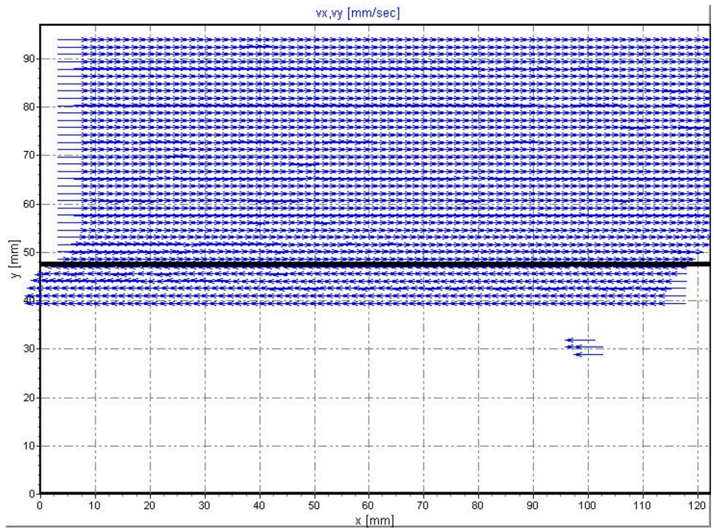

Figure 4.17: The velocity vectors over the wall does not indicate any physical velocity. Their function is to improve the velocity measurements at the close neighborhood of the wall and to indicate the surface boundary.

These vectors are in the opposite direction and at the same magnitude with flow which is at the close neighborhood of the surface. It should be noted that the velocity vectors below the boundary, do not reflect any physical velocity. They exist only for improving the results at the close neighborhood of the body surface.

All these techniques are used in the next chapters to analyze the flow. In the next section, we begin with the description of the experiments concerning the improvements of the model.

CHAPTER 5

SUCTION SLIT IMPROVEMENT PROCESS AND VALIDATION OF MODIFICATIONS

5.1 Introduction

In order to get useful experimental results on the flow separation process from the salient edge, it is necessary to guarantee controlled conditions upstream of the separation region. In this chapter we present the effort to improve the flow around the existing model. First we describe the former experimental arrangement and its shortcuts. The improved model is described in the second part of this section. Finally the improvements of the model are validated by flow visualizations with hydrogen bubbles. These observations are discussed in the last section of this chapter.

5.2 Improvements on suction

This section summarizes the improvements on the suction system.

5.2.1 Former suction arrangement and shortcuts

For the control of upstream conditions the arrangement of a special suction configuration is necessary since otherwise, flow separation already takes place at the leading edge. This is due to two main effects. First, the plate has a thickness of 15 mm with a wedge shaped leading edge. This leads to an asymmetry in the flow field with a flow around the sharp leading edge. Secondly the inclined downstream plate causes circulation which also favors the flow around the sharp leading edge. Without suction, a stagnation point forms at the lower side of the front part and flow separation appears at the leading edge. A separation bubble which contains unsteady vortical flow forms above the upper horizontal surface (Figure 5.1*a*).

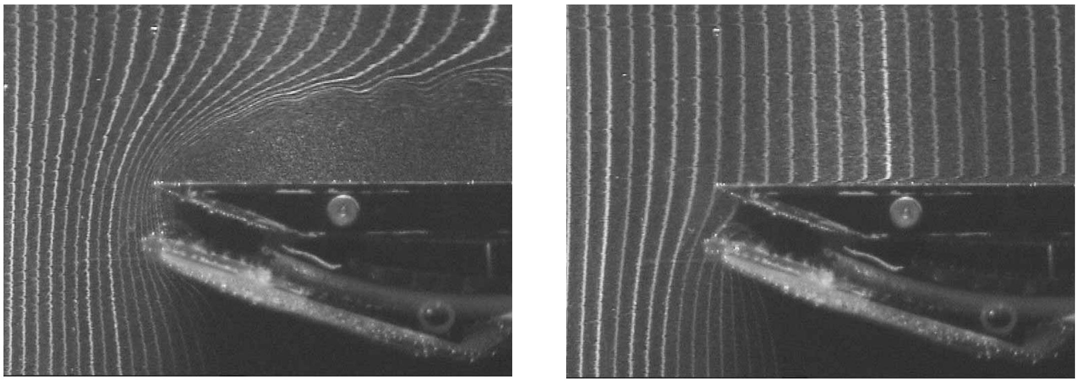

(a) **(b)**

Figure 5.1: Visualization of the flow structure at the leading edge of the existing model **(a)** without Suction **(b)**with Suction. Hydrogen bubbles method is used for visualization. Bubble generation frequency is 10 Hz with 13 % duty cycle. Base slant angle is 20 degrees. U_{inf}= 8.6 ± 0.5 cm/s.

Figure 5.1 compares the flow behavior near the leading edge with and without suction. In both cases the hydrogen bubble flow visualization technique is employed. The wire is positioned vertically about 5cm upstream of the leading edge. The slant angle is set to 20 deg. and the tunnel speed is set to 8.6 ± 0.5 cm/s. In Figure 5.1*a* it is observed that the flow is not attached to the surface. However, with suction, the flow attaches and follows the surface perfectly (Figure 5.1*b*). Clearly, the slit suction can avoid flow separation as shown by former experiments by Studer (2002).

As shown in Figure 5.2, the existing model used suction through a slit downstream of the leading edge to obtain attached laminar flow. Suction generated in this way turned out to be insufficient for the slant angles greater than 20^o degrees.

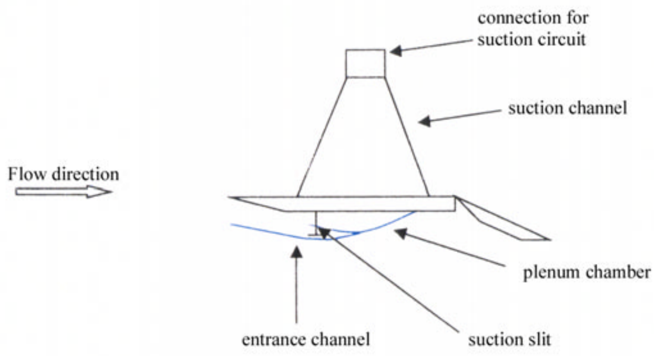

Figure 5.2: Schematic drawing of the existing configuration [Studer, 2002].

The relation between the position of the suction slit and the effectiveness of suction can be explained by modeling the slit with a line of sinks along the suction slit. Thus, the velocity potential of a single sink under the assumption of 2D flow is;

$$\phi = \frac{m}{2\pi r} \ln r \qquad \textbf{(5.1)}$$

where, *m* is the strength of the sink and *r* is the distance from the sink. From this relation, the radial velocity, v_r induced by the sink is found by;

$$\frac{\partial \phi}{\partial r} = v_r = \frac{m}{2\pi r} \qquad \textbf{(5.2)}$$

As seen from equation 5.2, the velocity induced by the sink is proportional to *1/r.* Therefore a suction slit, downstream of the leading edge, is less effective than a slit directly at the leading edge. Besides the position, a secondary defect of the existing slit was the wide distribution of the inlet flow outside the slit. A considerable amount of water was sucked off below the model which is not effective in order to achieve attached flow upstream of the salient edge on the upper side of the model. Both shortcuts can be diminished by moving the suction slit towards the leading edge.

Replacing the existing wide entrance channel in front of the slit by a new lid, arranged parallel to the leading edge, could solve both problems at once. The old 1mm thick polycarbonate piece was replaced by a 5mm thick Prespex lid. The circular shape of the plenum chamber was taken into account for the outer contour of the lid in order to avoid flow disturbance below the model. This new arrangement with suction at the leading edge, is shown in Figure 5.3.

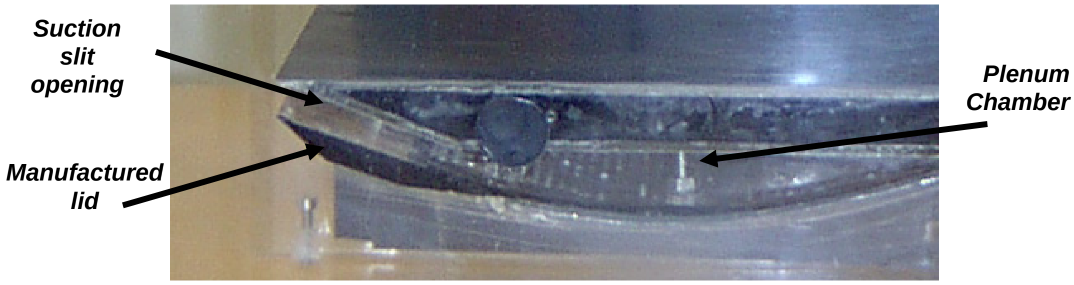

Figure 5.3: Side view of the suction slit and the manufactured lid. The suction slit entrance, the manufactured lid to carry the suction to the leading edge is indicated in the figure. The shape of the lid is adapted to the plenum chamber to minimize flow disturbance.

During the modification process, the form of the old plenum chamber was not modified. The new suction channel lid was fixed to the plenum chamber by means of screws. However, to overcome stiffness problems, related to the greater pressure loss along the slit, a row of screws was added in the middle of the plenum chamber to keep it rigid (Figure 5.3).

5.2.2 Control of the slit width over the modified model

According to equation (5.2) the suction velocity of a sink flow decreases with *1/r*. The flow inside the plenum chamber can also be modeled by a sink flow, the sink being located at the outlet of the chamber. The suction velocity produced by this sink decreases in spanwise direction. This creates excess suction at the side of the plenum chamber outlet and suction deficit at the opposite side unless a variable amount of pressure loss is forced along the slit. A higher pressure loss at the side of the plenum chamber exit and a lower pressure loss at the opposite side results in, uniform suction velocity distribution all over the leading edge.

Unfortunately, there is a disadvantage of applying suction. Pressure drop through the slit decreases the effectiveness of suction. However, the amount of maximum available suction rate, which is ~1.14 ± 0.002 l/s is enough to tolerate an amount of pressure loss of several percent to obtain uniform suction velocity.

There are two possible ways of arranging uniform suction at the leading edge that we have considered. First a pressure loss was created by means of a porous (permeable) material, such as foam and second the slit width was varied along the leading edge. The first technique did not work. The porous materials turned out to create too much pressure loss so that suction becomes ineffective. Moreover, it is difficult to adapt the thickness of the material to create the required variable pressure loss. That’s why we used variable slit width to control the pressure drop distribution.

To control the width of the suction slit along the leading edge, two rows of screws were added over the manufactured Prespex lid (Figure 5.4).

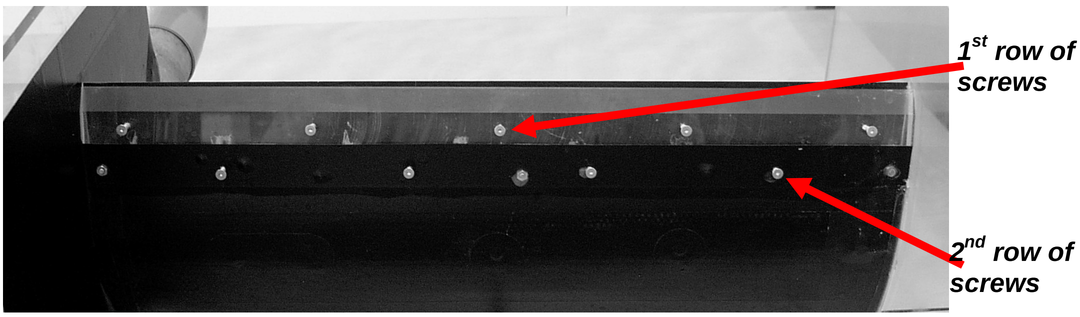

Figure 5.4: View from below the leading edge. Two rows of screws with five screws in the front row and four screws in the back row are visible in the figure. These screws allow adjusting the width of the suction slit.

Using these screws to regulate the slit width, uniform suction velocity is obtained. Since the variation of the slit width in the spanwise direction remains very small, the flow inside the slit can be assumed to be highly two-dimensional. Therefore, the pressure drop at each spanwise position can be estimated based on the flow between two parallel flat plates with the local slit width as distance. Figure 5.5*b* shows the schematic drawing of the arranged suction slit and its final dimensions.

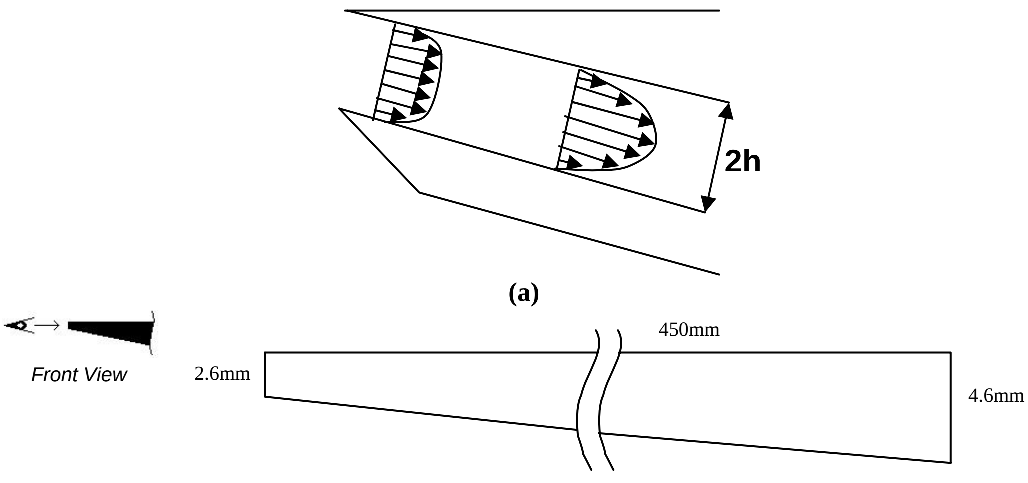

(a)

(b)

Figure 5.5: (a) Flow inside the slit can be modeled by flow between parallel plates in 2-D. **(b)** Schematic drawing of the final view of the suction slit in the downstream direction. The slit width is largely exaggerated.

The flow entering the suction slit is laminar. For laminar flow, entering a parallel-plate channel, the flow becomes fully-developed at a distance at the order of 50 to 100 heights of the channel thickness. For the current model, the length from the slit enterance to plenum chamber is much less than this value. Hence, simple channel flow model (Poiseuille flow) would not be valid. To calculate the pressure-drop in each section, Sparrow et al (1963) gives the following formulation, derived from the momentum equations.

$$\frac{p_o - p}{\frac{1}{2}\rho U^2} = 6\frac{x/h}{Uh/\nu} + K(x) \qquad \textbf{(5.3)}$$

Here, p_o is the entrance pressure and p is the pressure at any position x. h is the half channel thickness and U is the entrance velocity. The pressure-drop increment *K(x)* can be evaluated from the plots, that are given by Sparrow et al (1963) (Figure 5.6). For more details, the reader is also referred to White (1974).

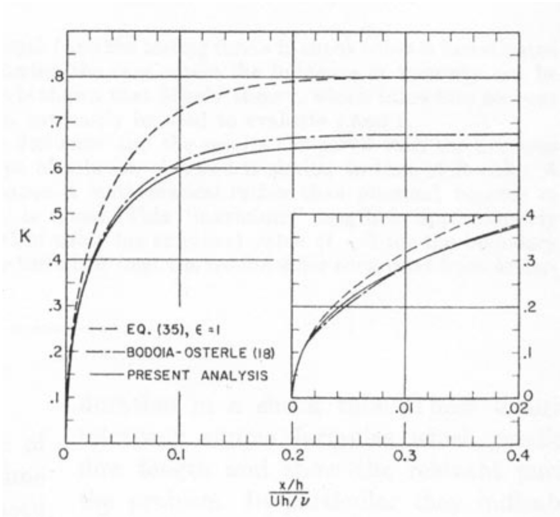

Figure 5.6: The incremental pressure drop due to flow development in a parallel-plate channel [Sparrow, 1963].

Suction velocity is uniform all over the suction slit. Thus, the entrance velocity at any section can be calculated from the suction rate of the pump. Maximum flow rate of the suction circuit is 1.14 ± 0.002 l/s. Thus, average velocity at the entrance slit is 0.70±0.001 m/s in each section of the model, for the slit dimensions shown in Figure 5.5*b*.

Since pressure drop is dependent on the gap between the two parallel plates, the variation of pressure across the slit differs at each position of the leading-edge. The following graph shows the pressure drop calculated by using equation (5.3) all along the suction slit.

Figure 5.7: Spanwise non-dimensional pressure loss across the slit.

According to Figure 5.7, the pressure loss is higher at the side where suction is applied and it decreases at the side, far from the suction as desired for the uniformity of suction velocity.

We tried to measure the velocity inside the slit by using PIV measurements, however it was not possible to obtain correct measurements since the illumination of the particles inside the channel was not possible. However, by using the CCD camera, long-exposure time images are taken to visualize the flow inside the channel as shown in Figure 5.8. Since exposure time is very long, pathlines of the particles inside the channel could be observed. A separation bubble at the tip of the channel and a reattachment point after ~*8h* distance from the slit entrance can be distinguished. The flow after the reattachment point is laminar inside the channel which means that the laminar flow assumption above is true. However, the flow separation at the tip, leads to an additional pressure drop, which has to be taken into account for complete evaluation of the pressure loss. For simplification purpose, we neglected this local pressure loss assuming that its distribution is uniform along the slit, only adding a constant to the resulting mentioned above.

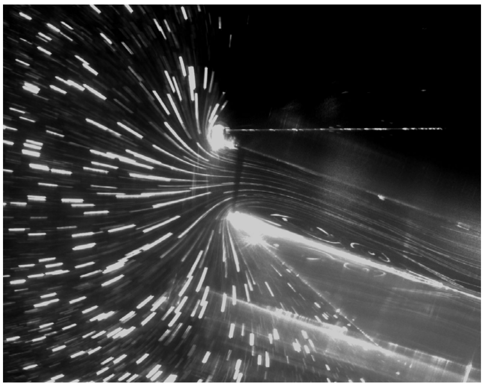

Figure 5.8: Long exposure time digital image of the suction slit by CCD camera at the middle plane of the model to visualize the streaklines in the suction slit. Suction rate is 0.32 ± 0.01 *l/s*, no free-stream velocity.

5.3 Validation of improvement on the suction slit

To validate the improvements on the suction slit and to arrange the slit for uniform suction, the experimental setup shown in Figure 5.9 is used.

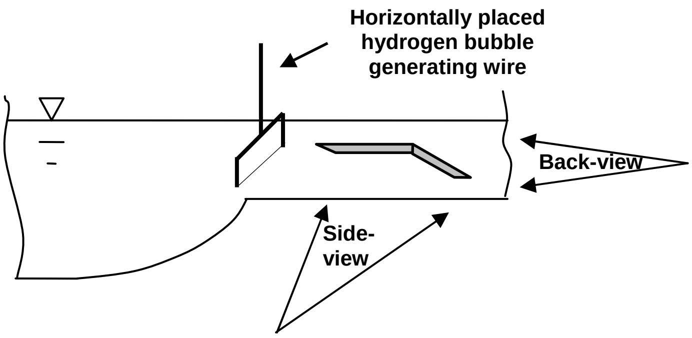

Figure 5.9: Schematic drawing of the experimental setup for the validation of the suction slit. The hydrogen bubble generating wire is positioned horizontally parallel to the leading edge of the model over the whole width of the model. The flow is observed from side and from behind in the upstream direction of the model to arrange the suction distribution.

Before the arrangement of the suction slit, the effects of changing the suction rate and varying the slit width were observed from behind, in the upstream direction with the help of the hydrogen bubbles. The bubble generating wire is positioned parallel to the leading edge horizontally over the whole tunnel width. The slant angle is set to its maximum value, which is 53^o degrees. First the suction slit was set to a thickness of 4.5 mm all over the span of the model. The channel speed is set to 8.6 ± 0.5 cm/s. Without suction, the flow is detached from the surface and it becomes quickly irregular and unsteady (Figure 5.10).

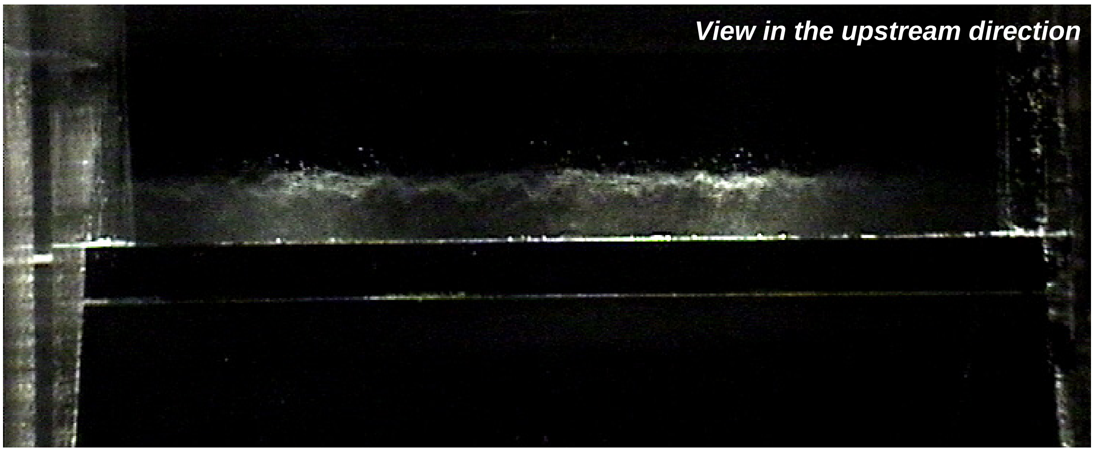

Figure 5.10: Hydrogen bubble flow visualization with 4.5 mm constant slit width and without suction, from behind. Channel Speed 8.6 ± 0.5 cm/s, 53^o slant angle, Hydrogen bubble generating wire is positioned 4cm below the surface level. The white hydrogen bubbles are visible, detached from the surface of the model indicating flow separation at the leading edge.

When the suction is turned on with maximum flow rate of 1.14 ± 0.002 l/s, the unsteady separation bubble disappears. However, as shown in Figure 5.10, the hydrogen bubble sheet released by the horizontal wire is inclined when the suction slit width is constant. At the side of the outlet of the plenum chamber –on the right-hand side of the figure- the height of the hydrogen bubble sheet from the surface is shorter than the other side. The suction velocity is not homogeneous in the spanwise direction. As mentioned in Section 5.2.2, this is due to the sink effect of the plenum chamber exit at the right-hand side of the figure.

Figure 5.11: Hydrogen bubble flow visualization from behind, with 4.5 mm constant slit width and 1.14 ± 0.002 l/s suction. Channel Speed 8.6 ± 0.5 cm/s, 53^o slant angle, hydrogen bubble generating wire is positioned 4 cm below the surface level. It is clear that suction is not uniformly distributed.

In order to get homogeneous suction, we first arranged the slit width with the help of visualizations from behind. The hydrogen bubbles are generated continuously, by positioning the bubble generator at the same position as in the previous visualizations. (The setup is shown in Figure 5.9). Using a visual control, the slit is arranged for homogeneous suction. Figure 5.12 shows the hydrogen bubble sheet after optimization of the slit width. It is clear that except for the edges of the model, where the wall effects are present, the bubbles are parallel to the leading edge and they are all at a constant height from the model.

Figure 5.12: Final arrangement of the suction slit with homogeneous suction. The bubbles are parallel to the surface of the model. Channel speed 8.6 ± 0.5 cm/s, 53^o of slant angle and 1.14 l/s suction. The hydrogen bubble generating wire is positioned 3 cm below the height of fixed panel and 7 cm upstream of the leading edge.

In order to obtain a quantitative control of the uniformity of suction velocity, images of hydrogen bubble timelines are used at three different spanwise positions. If the plenum chamber outlet side of the leading edge is taken as the reference point, the measurements are done at 125 mm, 225 mm and 325 mm in the spanwise direction, whereas the overall span of the leading edge is 450mm. If we denote the span of the model by b, then the measurements are done at $0.28b$, $0.5b$ and $0.72b$ of the model. The slant angle is again the maximum angle 53^{o} deg.

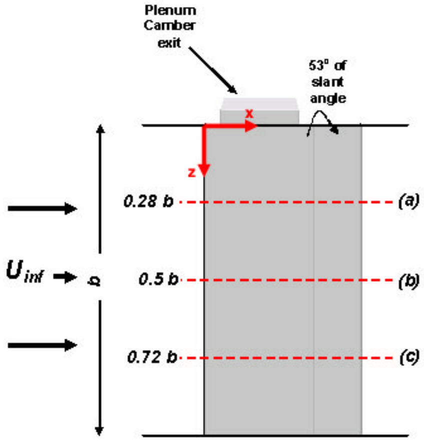

Top view of the model, showing the measurement stations with respect to the plenum chamber exit. The base slant angle is 53^o for this configuration

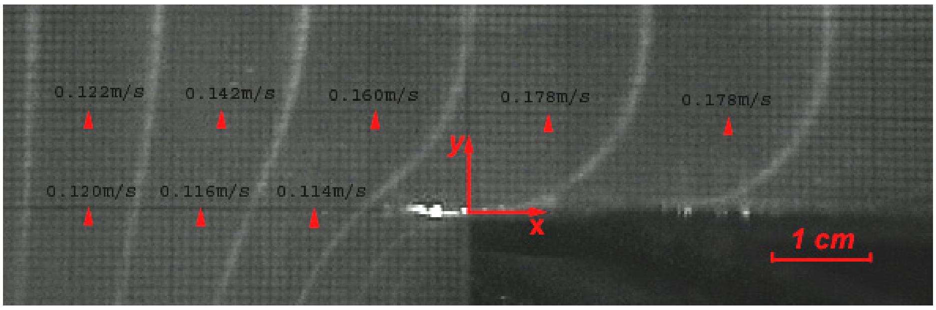

(a) Hydrogen bubbles at *y/b = 0.28* Tunnel Speed 8.6 ± 0.5 cm/s Freq:10Hz Cycle:10 %

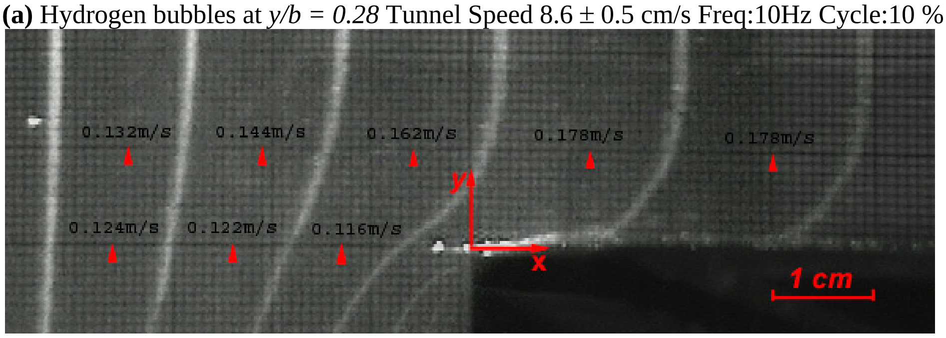

(b) Hydrogen bubbles at *y/b = 0.5* Tunnel Speed 8.6 ± 0.5 cm/s Freq:10Hz Cycle:10 %

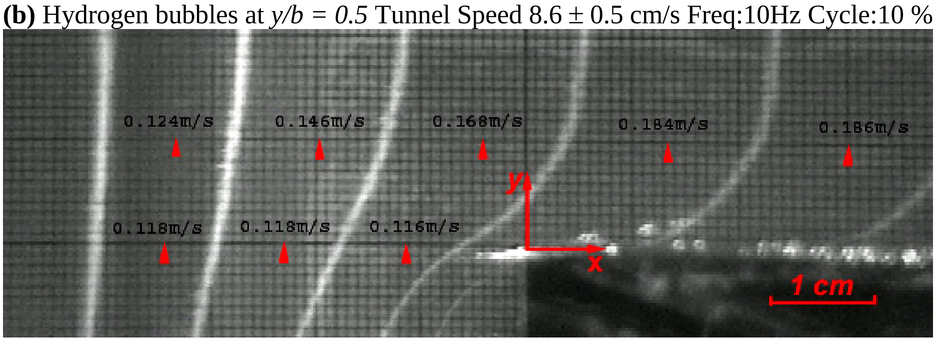

(c) Hydrogen bubbles at *y/b = 0.72* Tunnel Speed 8.6 ± 0.5 cm/s Freq:10Hz Cycle:10 %

Figure 5.13: Velocity measurements at the entrance of the suction slit. Measurements are performed with hydrogen bubble technique at three different spanwise positions. Red arrows show the positions where the indicated velocities are measured.

The velocity distribution in the region of the suction slit entrance has been obtained using the hydrogen bubble technique described in Chapter 3. It is used to validate the uniformity of suction velocity quantitatively.

If we take the leading edge of the model as our reference point, the propagation of velocity over the model with respect to this reference point is plotted in Figure 5.14.

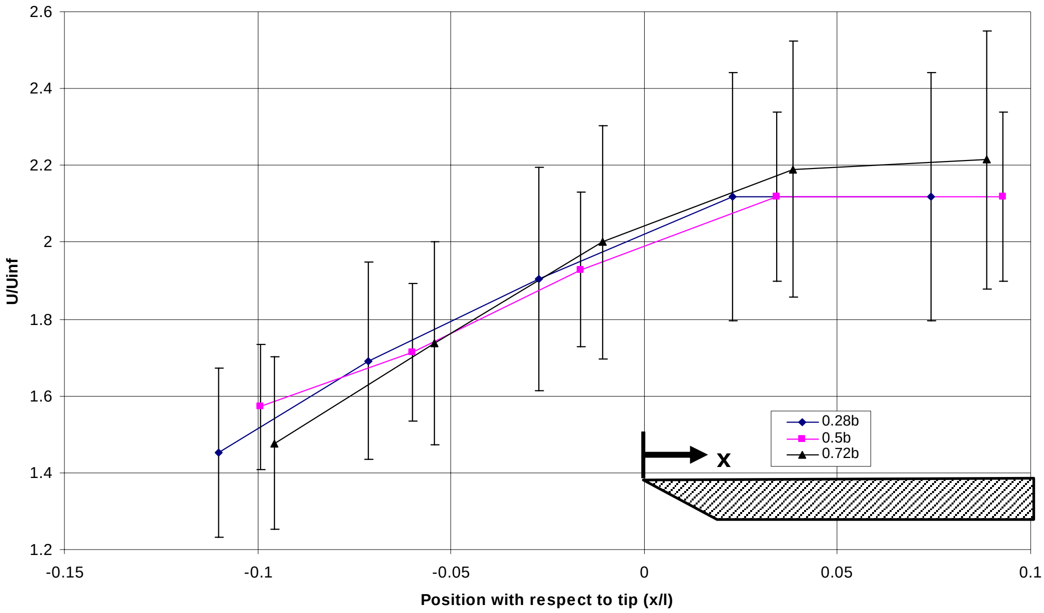

Figure 5.14: Velocity increase in the streamwise direction around the leading edge 1cm above the surface of the front panel for $U_\infty = 8.6 \pm 0.5$ cm/s and 1.14 ± 0.02 l/s suction rate. Three different spanwise sections are compared.

From Figure 5.14, we see that the increase of the velocity around the leading edge is rather uniform in the spanwise direction. The objective of uniform suction is therefore obtained. Table 5.1 indicates the numerical data obtained from these measurements.

Table 5.1: Non-dimensional velocities in the neighborhood of the leading edge, at three spanwise positions. Measurements are performed at 1 cm above the surface level. Analysis of the data in Figure 5.11. Velocities are non-dimensionalized with the channel velocity ($U_\infty = 8.6 \pm 0.5$ *cm/s*) and distances are non-dimensionalized by the length of the plate (*l=350 mm*).

Spanwise Position					
0.28b (125mm)		0.5b (225mm)		0.72b (325mm)	
X Position	U/U_∞	X Position	U/U_∞	X Position	U/U_∞
-0.11	1.45	-0.1	1.57	-0.1	1.48
-0.07	1.69	-0.06	1.71	-0.05	1.74
-0.03	1.90	-0.02	1.93	-0.01	2.00
0.02	2.12	0.03	2.12	0.04	2.19
0.07	2.12	0.09	2.12	0.09	2.21
$U_{L.E.} = 2.02\ U_\infty$		$U_{L.E.} = 2.01\ U_\infty$		$U_{L.E.} = 2.04\ U_\infty$	
Mean velocity at tip: $2.023\ U_\infty$			Mean Deviation at L.E. = 0.5%		

Using the error estimation procedure for the hydrogen bubble technique given in Appendix A, the accuracy of the measured velocity is ±0.8 cm/s. This corresponds to ~4.6% error with respect to the mean velocity at the leading edge. Errors in the *x/l* component are negligible with respect to the uncertainty of the velocity measurements.

During the validation of suction experiments, both slant angle and the suction rate was set to maximum values to obtain uniform suction at the most severe conditions. However, these are not the conditions in the actual experiments for the investigation of flow separation and it was, therefore, necessary to perform further experiments with more realistic slant angles and a reduced suction rate which is just enough to avoid flow separation.

In these experiments, the number of stations where the measurements were taken is increased to five to have a better idea about the velocity distribution. Measurements were done at 0.28b, 0.39b, 0.5b, 0.61b and 0.72b for two different slant angles of 15^o and 30^o.
To set the suction rate to required minimum, the suction rate gradually decreased until the separation bubble appears and afterwards, the suction rate was increased just enough to remove the bubble. In more recent experiments, the installed turbine meter allowed direct control of the flow rate, making visual control superfluous.

Figure 5.15 shows an example of this experimental procedure for a slant angle of 15^o. Clearly, flow separation disappears and leaves place to the formation of a laminar boundary layer.

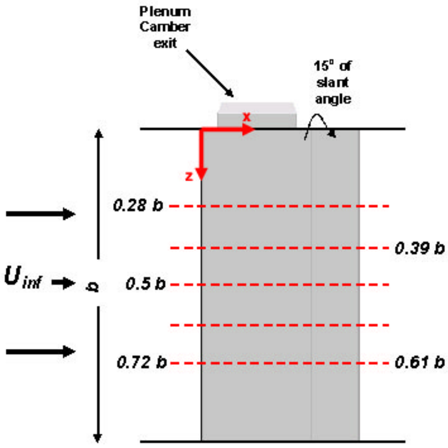

Top view of the model, showing the measurement stations with respect to the plenum chamber exit. The base slant angle is 15° for this configuration.

y/b=0.28

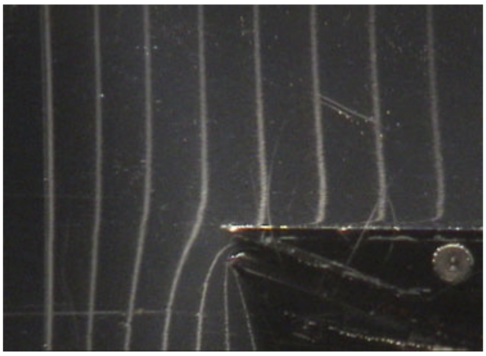

y/b=0.72

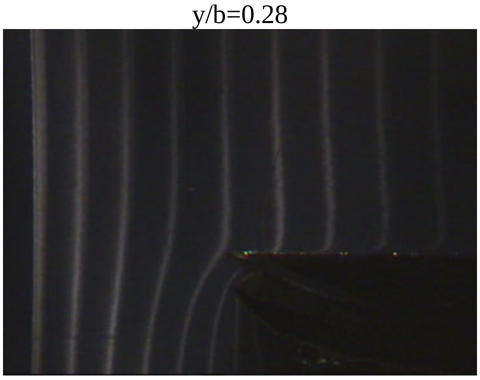

y/b=0.39

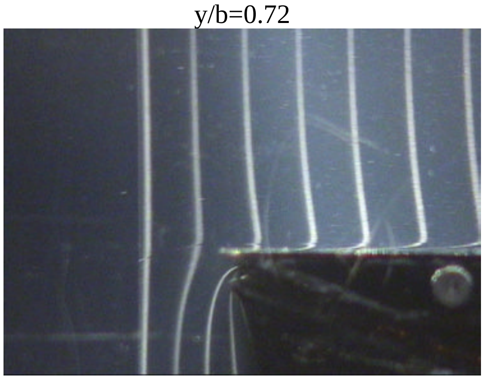

y/b=0.61

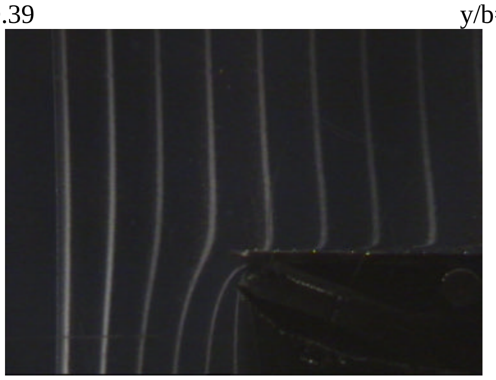

y/b=0.5

Figure 5.15: Hydrogen bubble flow visualizations at five different spanwise positions for 15° degrees of base slant angle. U_∞=8.6 ± 0.5 cm/s, just enough suction is applied to attach the flow to the surface.

Again the measurements are performed in a plane, 1 cm above the model and parallel to the surface. The velocity measurement from the captured images by using hydrogen bubble technique gives the spanwise velocity distribution, shown in Figure 5.16.

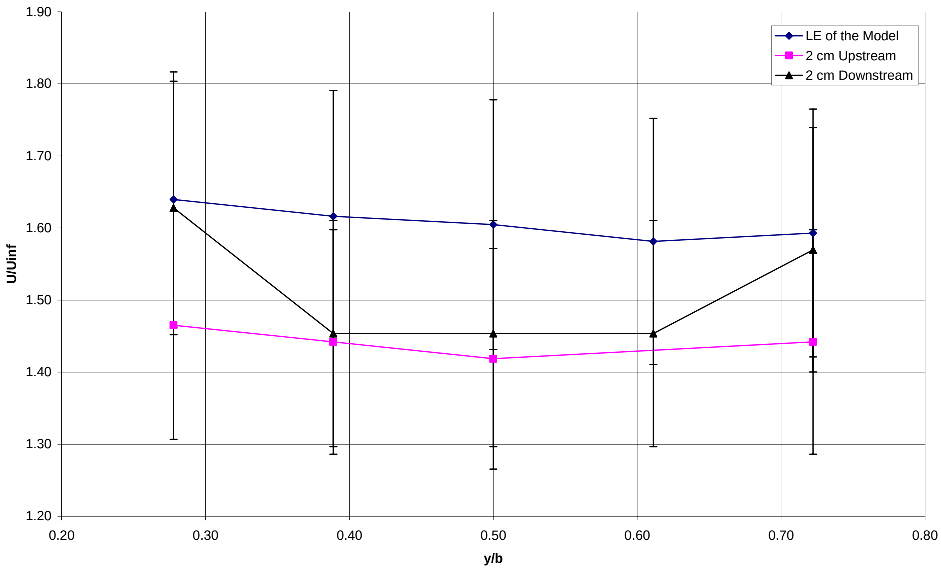

Figure 5.16: Spanwise uniformity of the velocity around the leading edge in a plane, 1cm above the model surface at three different streamwise stations. The base slant angle is 15^o and U_∞=8.6 ± 0.5 cm/s. The suction rate is just enough to attach the flow to the surface.

Figure 5.16 shows that the velocity distribution upstream of the model is almost constant. The corresponding data are resumed in Table 5.2.

Table 5.2: Analysis of the velocity measurements shown in Figure 5.16. Mean velocities and deviation from mean velocities at 1cm above the surface at three different streamwise locations. The base slant angle is 15^o and the reference velocity is U_∞=8.6 ± 0.5 cm/s. The mean deviations show the deviation from the mean velocity at that position.

Position with respect to the leading edge	Mean Velocity		Mean Deviation all over the leading edge (%)
	Non-dimensional	Dimensional (cm/s)	
2 cm upstream	1.44 ± 0.06 U_∞	12.4	0.8
Over the leading edge	1.63 ± 0.06 U_∞	14.0	1
2 cm downstream	1.51 ± 0.06 U_∞	13.0	4.6

Although it is expected that the flow accelerates in the streamwise direction, Figure 5.14 shows that the velocity, 2 cm downstream of the leading edge is lower than the velocity at the leading edge. However the error bars indicate that the deceleration at 2 cm with respect to the leading edge velocity is inside the error bars.

Below in Figure 5.17, results of the images captured for the same experiment with 30^o of base slant angle are represented.

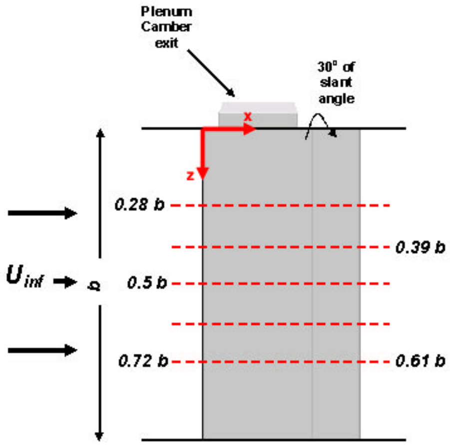

Top view of the model, showing the measurement stations with respect to the plenum chamber exit. The base slant angle is 30^{o} for this configuration.

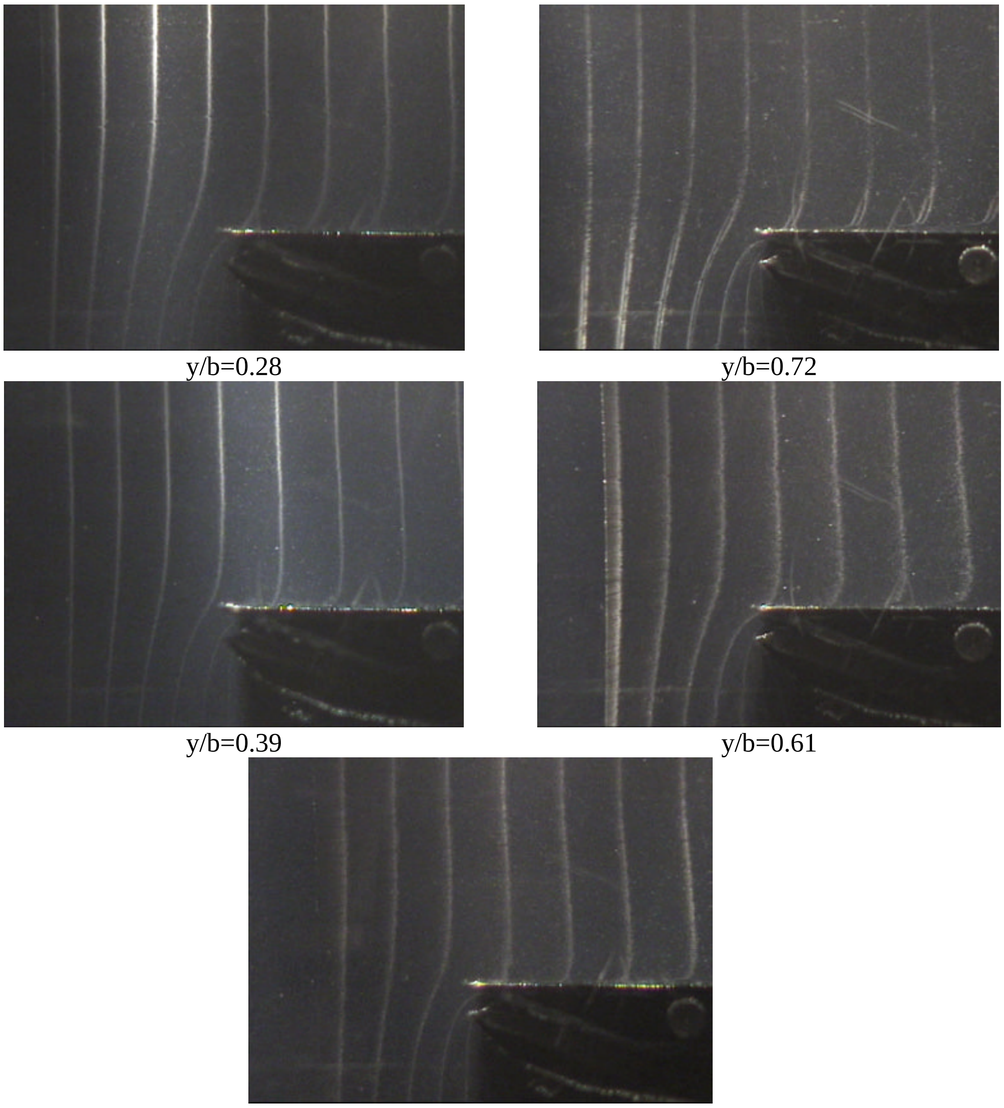

y/b=0.28 y/b=0.72

y/b=0.39 y/b=0.61

y/b=0.5

Figure 5.17: Hydrogen bubble flow visualizations at five different spanwise positions for 30^{o} degrees of base slant angle. U_{∞}=8.6 ± 0.5 cm/s, just enough suction to attach the flow to the surface.

At 30^o of slant angle, the same analysis ends up with the following graphs:

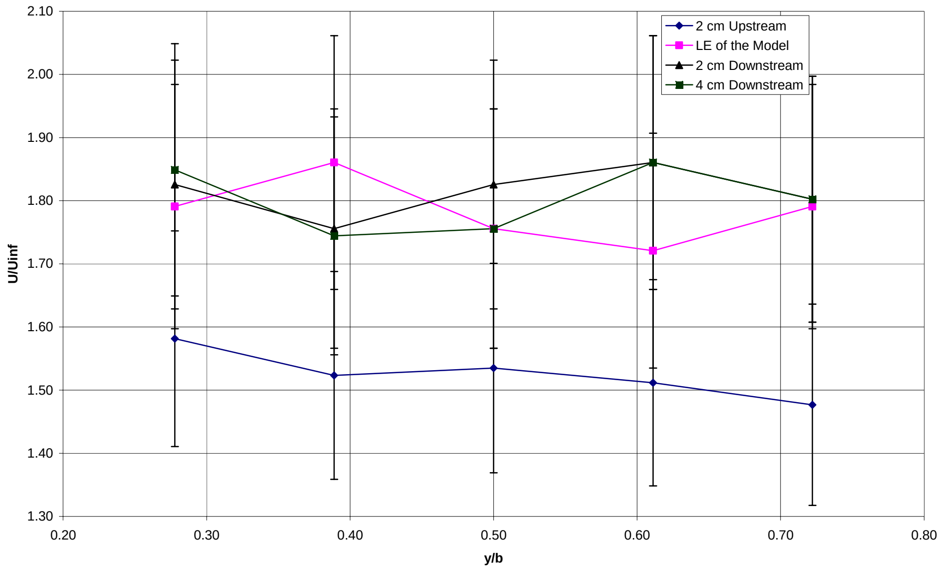

Figure 5.18: Spanwise uniformity of the velocity around the leading edge in a plane, 1cm above the model surface at four different streamwise stations. The base slant angle is 30^o and U_∞=8.6 ± 0.5 cm/s. The suction rate is just enough to attach the flow to the surface.

Table 5.3 shows the mean velocities at the positions that measurements were performed and the mean deviations at those positions.

Table 5.3: Analysis of the velocity measurements shown in Figure 5.18. Mean velocities and deviation from mean velocities at 1cm above the surface of the front panel at 4 different streamwise locations. The base slant angle is 30^o. Velocities are non-dimensionalized by U_∞=8.6 ± 0.5 cm/s. Mean deviation shows the deviation from the mean velocity at that position.

Position with respect to the leading edge	Mean Velocity		Mean Deviation all over the leading edge (%)
	Non-dimensional	Dimensional (cm/s)	
2 cm upstream	1.52 ± 0.06 U_∞	13.1	1.7
Over the leading edge	1.78 ± 0.06 U_∞	15.3	4.6
2 cm downstream	1.81 ± 0.06 U_∞	15.6	1.5
4 cm downstream	1.80 ± 0.06 U_∞	15.5	2.9

Accuracy of the measurements above is 7.7 mm/s, which corresponds to an error around 5 %.

However, the error in non-dimensional velocity term is around 10.8 %, because of the uncertainty of the U_{inf}.

The tip velocity at 1 cm above the model for 15^o of slant angle is 13.8 cm/s and for 30^o of slant angle, 15.3 cm/s. The cause of this difference is not only the difference in slant angle, but also the difference in suction rates. As the suction rates are different, comparing the numerical results of these two configurations does not give any information. But it is observed that the mean deviation from the mean velocity is 1.0 % for 15 degrees of slant angle and 4.6% for 30 degrees of slant angle. In view of the measurement errors, these errors can be tolerated.

The results of the experiments at 15^o and 30^o show that suction distribution is homogeneous for given conditions. Also the experiments at the most severe conditions with a slant angle of 53^o (which is the maximum allowed by the model) and maximum suction rate, show attached flow with uniform velocity distribution over the leading edge. Hence, the applied improvements are satisfactory for the purpose of the present study.

The improvements of the suction slit described in this chapter allow a better control of flow separation at the leading edge, as far as efficiency and homogeneity of the suction system are concerned. Furthermore, they enlarge the range of possible slant angles. In the next chapter, these improved flow conditions allow a more detailed analysis of the behavior of the boundary layer upstream of the salient edge.

CHAPTER 6

INDIRECT MEASUREMENT OF PRESSURE GRADIENT

6.1 Introduction

The aim of the present chapter is to estimate the pressure gradient along the horizontal plate of the model in order to analyze the flow conditions upstream of separation. The boundary layer thickness of the Blasius layer is calculated and compared to the experimental boundary layer thickness measurements over the model by using hydrogen bubble technique. The displacement thickness deduced from these measurements is used to estimate the axial pressure gradient along the model. Finally, PIV measurements of velocity profiles inside the boundary layer are compared with the results of the hydrogen bubble technique.

6.2 Measurement of the boundary layer thickness

In order to determine the pressure gradient along the fixed plate upstream of the salient edge, we measured the velocity inside the boundary layer. The slant angle was set to 0^o to obtain a flat plate with 350 mm of length. The hydrogen bubble technique was used to measure the streamwise velocity distribution inside the boundary layer. Bubbles were released in the middle plane of the model from a vertical wire. The position of this wire was very close to the model (more than 3.5 mm which is the required distance for bubbles to attain flow speed). The tension aplied on the wire was 60 V. The bubble frequency was 10 Hz with 9% duty cycle.

The video camera was positioned at ~1 m distance from the bubble generation plane to obtain high resolution images. An optical zoom of 21 was used to allow the maximum possible resolution of the velocity gradients near the wall.

Measurements are performed at 6.4 ± 0.4 cm/s channel velocity and 0.30 ± 0.11 l/s of suction rate.

Examples of images obtained with this arrangement are shown in Figure 6.1. In each successive image, the increasing boundary layer thickness can be clearly observed from the evolution of the hydrogen bubble timelines. The position of the images is given in both dimensional and non-dimensional form. The reference length is the length of the model $l = 350\ mm$.

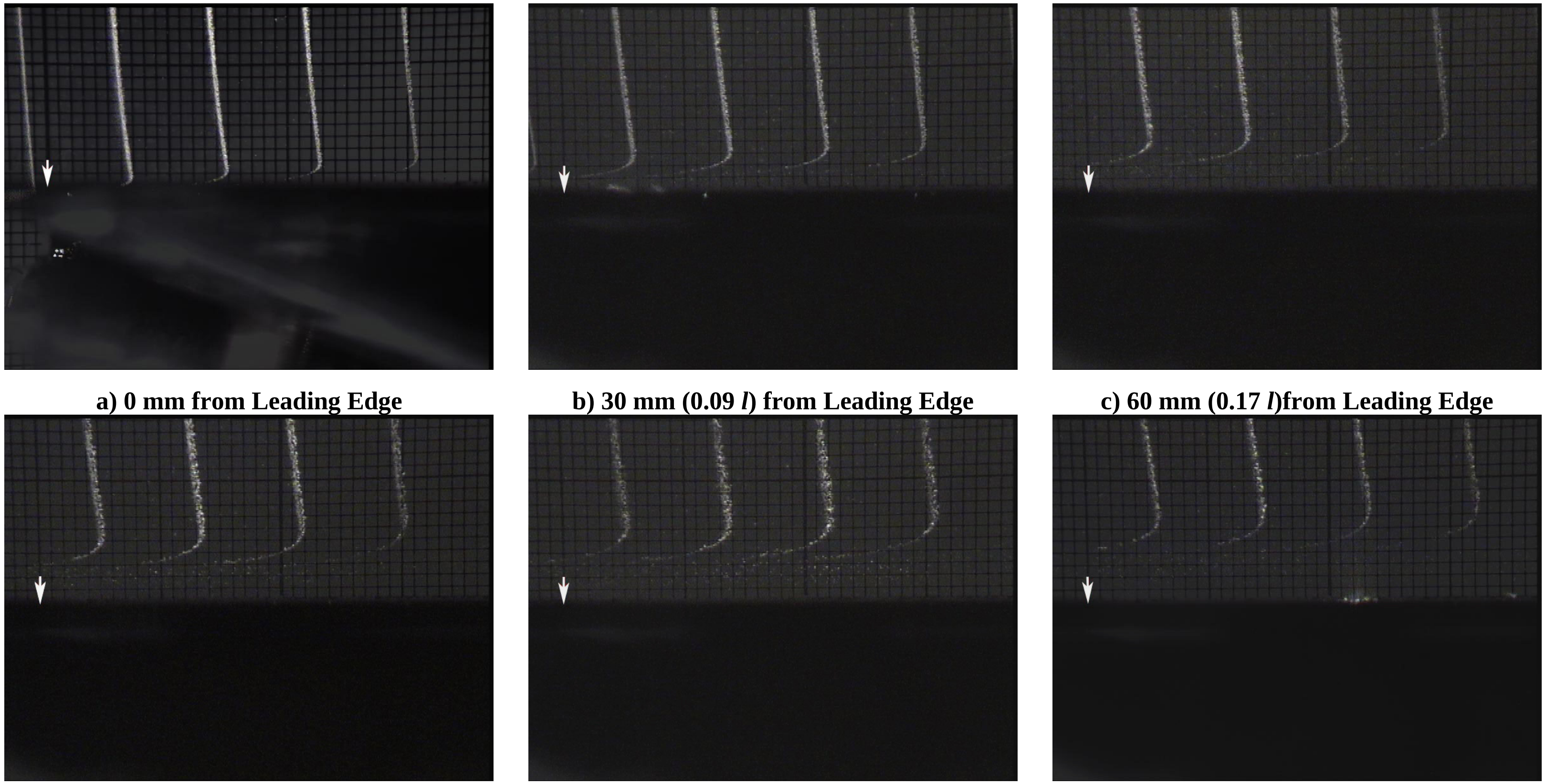

a) 0 mm from Leading Edge | **b) 30 mm (0.09 *l*) from Leading Edge** | **c) 60 mm (0.17 *l*)from Leading Edge**

d) 90 mm (0.26 *l*) from Leading Edge | **e) 120 mm (0.34 *l*) from Leading Edge** | **f) 150 mm (0.43 *l*) from Leading Edge**

Figure 6.1: Visualization of the evolution of boundary layer in the middle plane of the model at 6.4 ± 0.4 cm/s tunnel speed and 0.30 ± 0.11 l/s suction rate along the leading edge. Timelines are generated using hydrogen bubbles with 10 Hz frequency and 9% duty cycle with 60V. The white arrow indicates the position of the reference points for measurements, with respect to the leading edge.

In the downstream direction the timelines become less sharp since the bubbles begin to dissolve in the working fluid. As a result, the precision of velocity measurements decreases with increasing distance from the leading edge.

The analysis of the recorded images, according to the procedure described in chapter 4, gives the evolution of the boundary layer thickness in the axial direction, shown in Figure 6.2. For comparison, this figure also contains the boundary layer thickness obtained from the Blasius model.

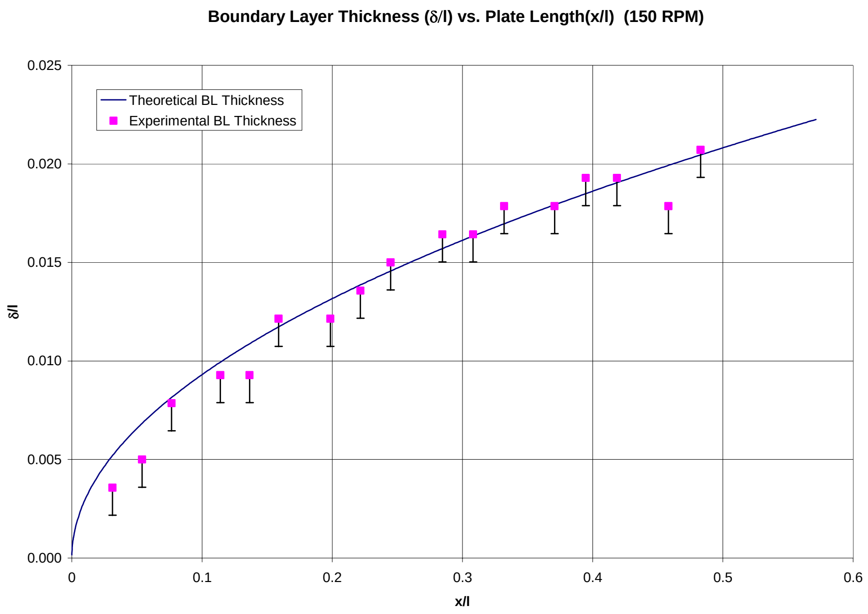

Figure 6.2: Non-dimensional boundary layer thickness as a function of axial distances x/l for $U_\infty = 6.4 \pm 0.4$ *cm/s*. All the lengths are non-dimensionalized by the full plate length, $l = 350$ *mm*. The results are compared to the Blasius model for a flat plate without pressure gradient.

As a whole, the measurements and Blasius model show similar behavior. However, near the leading edge, the measured values are smaller in the mean. This might be caused by the downward component due to suction. From Figure 5.8, it is clear that suction introduces a downward velocity component at the leading edge. This component reduces the boundary layer thickness close to the leading edge. More downstream,this effect becomes negligible.

The outlier at $x = 0.46\ l$ might be due to errors caused by the bubbles which start to dissolve as shown in Figure 6.1.

During the analysis of the hydrogen bubble images, velocity measurements were done with 0.5 mm increments in the normal direction. Hence, there is a measurement uncertainty of 0.5 mm in y-direction. Moreover there are also errors due to the hydrogen bubble method itself, which are described in more detail in Appendix A. However the order of these errors is small with respect to the errors due to measurement increments. Hence, only the errors due to measurement increments are shown in Figure 6.2.

6.3 Estimation of pressure gradient

The pressure gradient over the surface of the model can be calculated by using the displacement thickness of the boundary layer. This displacement thickness is ~1/3 of the measured boundary layer thickness as stated in chapter 2. Since the measurements of the boundary layer thickness are in good agreement with the Blasius profile, we can use the result obtained for the Blasius profiles for the estimation of the pressure gradient.

If we call the area between the leading edge of the model and the free surface level as A_1 and the area between the free surface level and the edge of the displacement boundary layer as A_2, under the assumption of incompressible fluid and uniform distribution of velocity U in each streamwise section, the conservation of mass gives, the local free-stream velocity U:

$$U = \frac{A_1}{A_2} U_\infty \tag{6.1}$$

Figure 6.3 shows the local pressure gradient over the upstream plate of the model for 6.4 ± 0.5 cm/s channel velocity. Under the assumption of negligible viscous forces, far from the boundaries this pressure gradient is obtained from:

$$\frac{dp}{dx} = -\rho U \frac{dU}{dx} \tag{6.2}$$

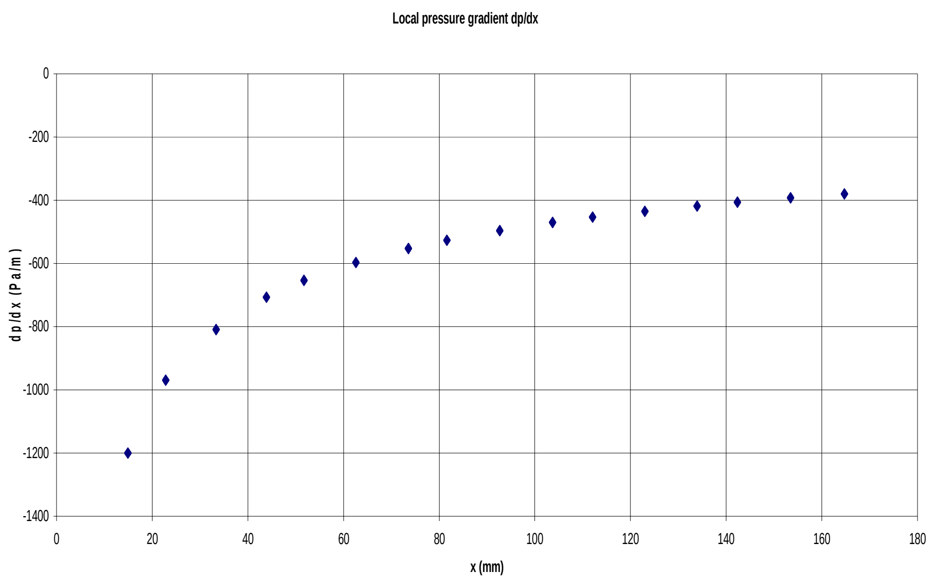

Figure 6.3: Pressure gradient over the model for 6.4 ± 0.4 cm/s velocity.

From this graph, it is observed that the local pressure gradient is negative ($\delta p/\delta x<0$). This kind of gradient is called favorable pressure gradient and it keeps the flow attached to the body. However it is also clear from this figure that our Blasius boundary layer is only a first order estimate, since a pressure gradient exists.

During the determination of the pressure gradient, the boundary layer at the free surface of the water channel has not been considered. This is because, the boundary layer is formed far upstream of the test section and it is fully developed at the location of the model. Since the value of $d\delta / dx$ decreases with increasing x, the change in displacement thickness of the boundary layer along the free surface is negligible over the length of the model*:*

$$\frac{d\delta}{dx} \approx \frac{5}{2}\sqrt{\frac{\nu}{Ux}} \tag{6.3}$$

To validate the measurements of the boundary layer thickness, the measurements were repeated by measuring directly the velocity profiles with the PIV technique. Figure 6.4 shows the resulting velocity vector map.

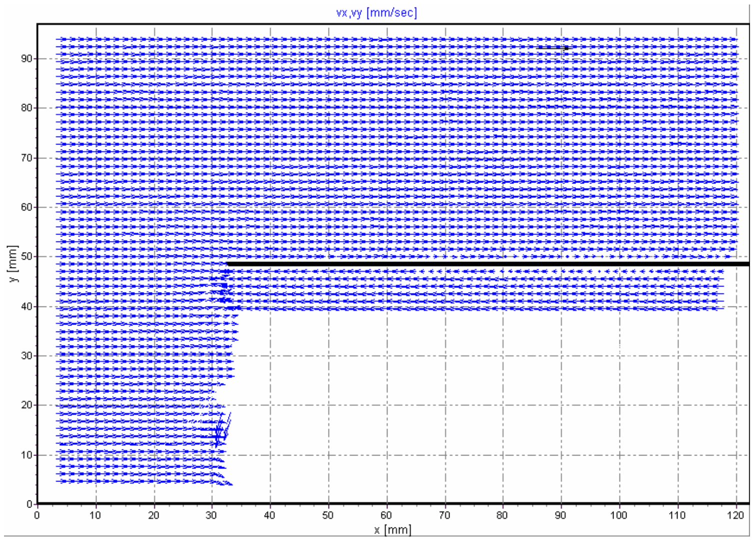

Figure 6.4: Velocity vector maps over the surface. Boundary layer profiles can be observed over the surface. Channel velocity is 6.4 ± 0.4 cm/s and the suction rate is 0.27 ± 0.02 l/s.

From the vector map above, we can obtain the boundary layer profiles at the same locations where hydrogen bubble measurements are taken. This gives us the possibility to compare the boundary layer profiles and verify the boundary layer thickness. Figure 6.5 shows these profiles.

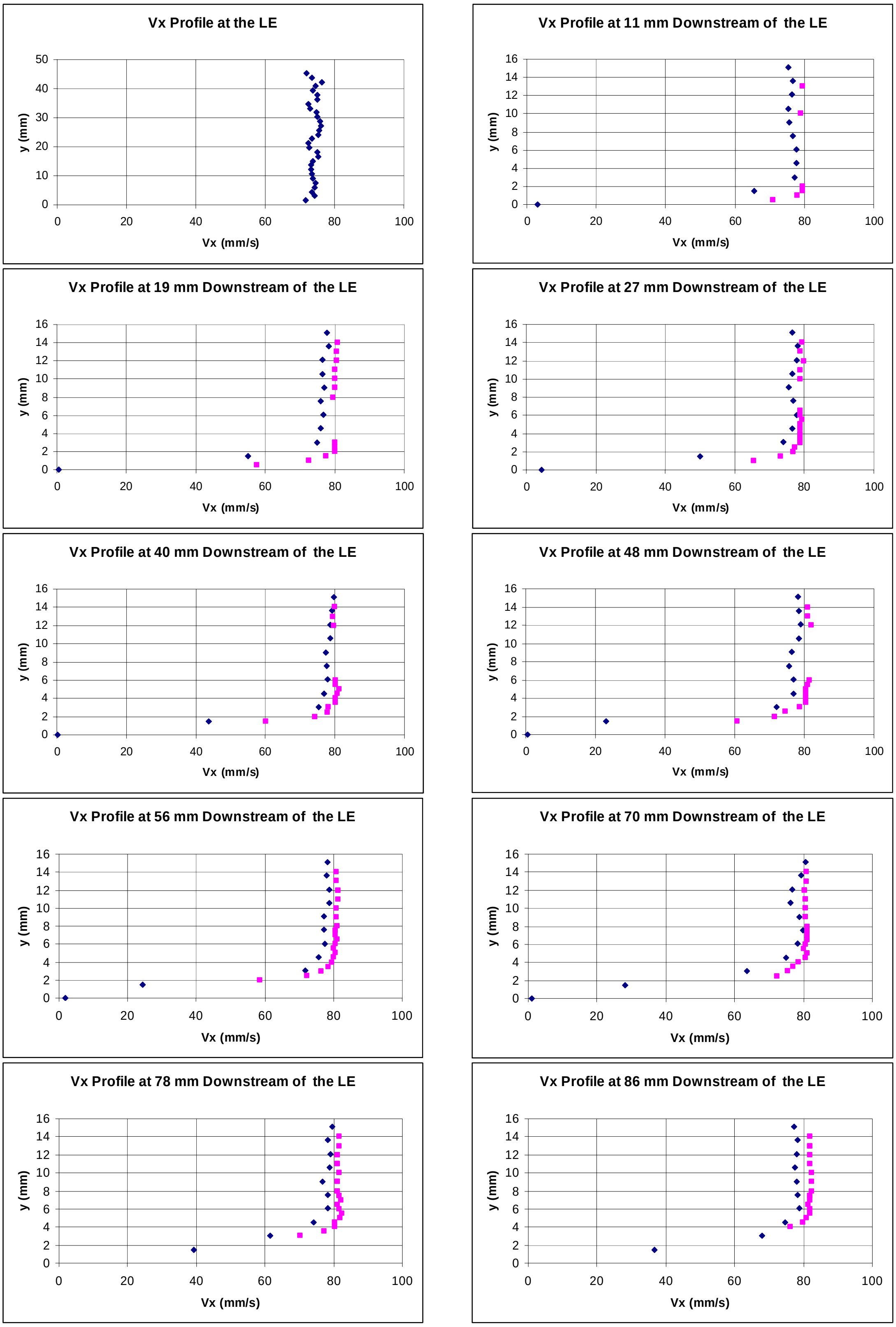

Figure 6.5: x-component of the velocity profile with ~0.30 *l/s* suction rate. Blue data series show the PIV measurements, pink data points show the hydrogen bubble measurements. (U_∞ = 6.4 ± 0.4 m/s) PIV measurements were performed with 0.30 ± 0.02 l/s suction rate whereas hydrogen bubble measurements were performed with 0.30 ± 0.11 l/s suction rate.

It appears that the freestream velocity measured by PIV is lower. The difference between the mean value of the hydrogen bubble measurements and the PIV measurements is around ~5 %. However, considering the error in the velocity measurements with the hydrogen bubble technique, which is ~1.3%, the results of both techniques are in good agreement. In addition, there might be a small uncontrolled difference in the experimental conditions in both series of experiments.

In conclusion, the comparison between the measured boundary layer thickness and the theoretical Blasius boundary layer gives us the possibility to evaluate the displacement effect of our model at zero slant angle. The deduced pressure gradient is clearly favorable and avoids any tendency of flow separation until the end of the model at zero slant angle. The adverse pressure gradient imposed by circulation at zero slant angle is thus also negligible for this configuration. However, at high slant angles, important pressure gradients may form, making it necessary to check for attached flow. Since the visualizations presented in the next chapter all show attached flow, we did not yet measure this influence of circulation with increasing slant angle.

CHAPTER 7

STUDY OF THE FORMATION OF FLOW SEPARATION

7.1 Introduction

In this chapter, we study the formation of flow separation in view of the different concepts mentioned in chapter2. In the first section, the results of qualitative flow visualizations, obtained with a combination of the hydrogen bubble and electrolytic precipitation techniques are presented. These visualizations are completed in the next section by PIV measurements of the separation region. Section 7.4 compares the observed flow behavior with the theoretical models introduced in chapter 2, in particular with the results of Falkner-Skan. Finally, preliminary results on the effect of Reynolds number variations are presented.

7.2 Visualization of formation of flow separation at different slant angles

The evolution of the flow structure for different slant angles has been studied with the hydrogen bubble technique in combination with the electrolytic precipitation. The hydrogen bubbles are generated in a plane adjacent to the body surface to analyze the flow outside the separation zone. The bubble wire was placed horizontally, 16 cm upstream of the salient edge, 2 cm above the front plate of the model. The frequency of bubble generation was 2 Hz.

The electrolytic precipitation technique allows visualizing the limitations of the separation region and in particular the flow structure inside this region. Two solder wires are fixed on the surface of the model. The first solder wire, 20 mm upstream of the salient edge is employed to visualize the evolution of the shear layer between the main flow and the separation region. The second one, which is fixed 30 mm downstream of the salient edge, is used for determination of the flow structure inside the separation region. Figure 7.1 shows the position of the electrolytic precipitation wires on the model.

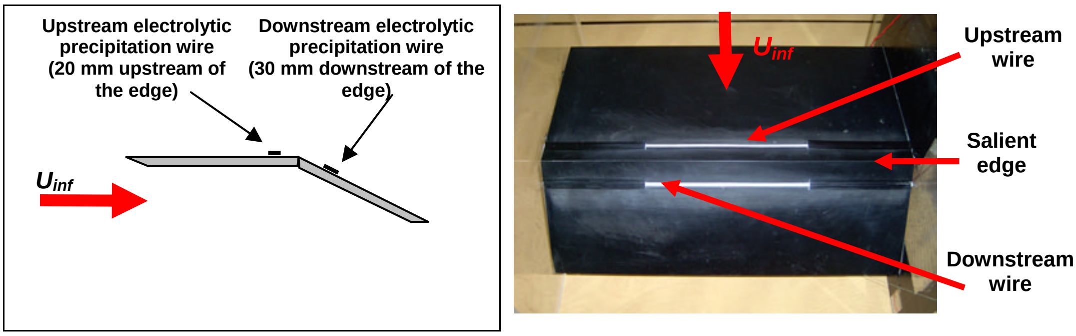

(a) (b)

Figure 7.1: (a) Schematic drawing of the experimental arrangement from side. **(b)** Image of the model, showing the position of the solder wires. The wires are 20 cm in length, 2-3 mm in width and 0.07 - 0.1 mm in thickness.

In all visualization experiments presented in this section, the channel speed was set to 6.4 ± 0.4 cm/s. The suction rate was adjusted to 0.87 ± 0.01 l/s in order to guarantee attached flow over the model for a maximum slant angle of 53^{o}. The water temperature was 24.6 ± 0.2^{o} C which gives a kinematic viscosity of 0.9 x 10^{-6} m^2/s according to Weast [1962]. The corresponding Reynolds number, based on the chord length, is 24800. The water level inside the test section was 25.5 ± 0.1 cm and the air temperature was 24.3 ± 0.2^{o} C.

Figure 7.2 and 7.3 show the results of the visualizations obtained with the upstream and downstream wires respectively. In both figures, the pulsed hydrogen bubbles illustrate the deviation of the flow direction far from the body surface.

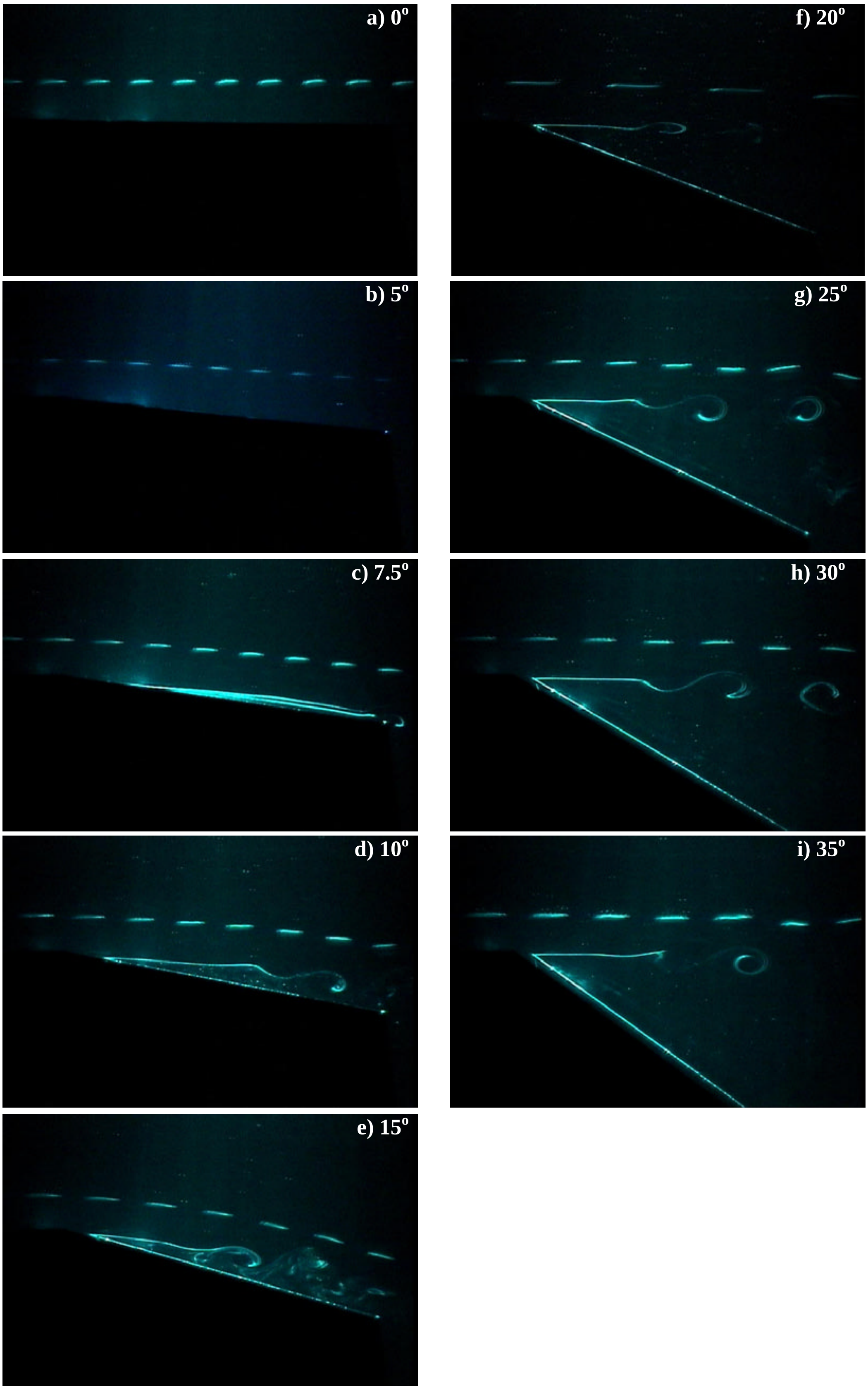

Figure 7.2: Visualization of flow separation from the salient edge by hydrogen bubbles and electrolytic precipitation techniques for increasing slant angles. Velocity is 6.4 ± 0.4 cm/s, the applied suction rate at the leading edge is 0.87 ± 0.01 l/s. The electrolytic precipitation wire is positioned 20mm upstream of the salient edge.

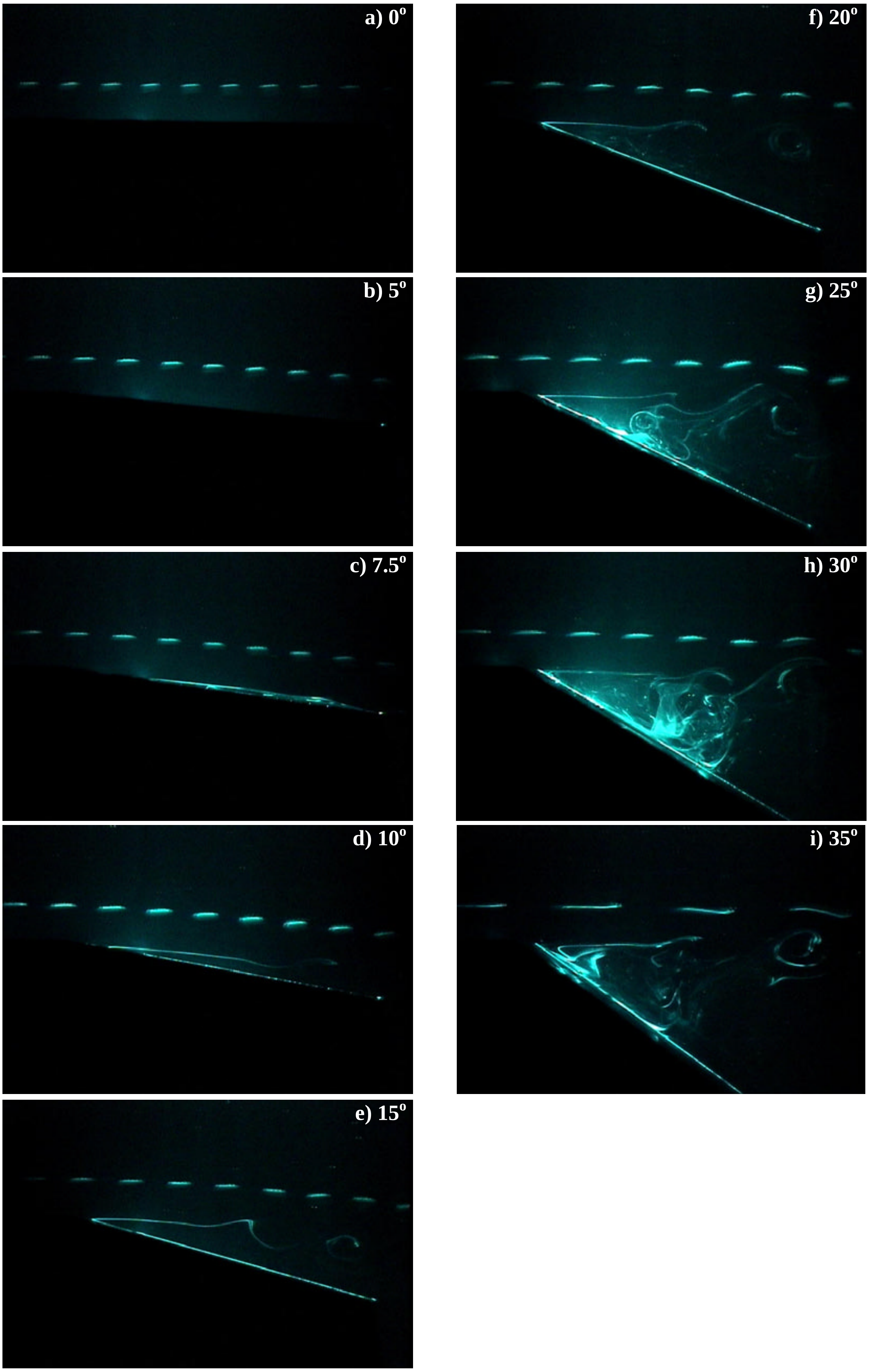

Figure 7.3: Visualization of flow separation from the salient edge by hydrogen bubbles and electrolytic precipitation techniques for increasing slant angles. Velocity is 6.4 ± 0.4 cm/s, the applied suction rate at the leading edge is 0.87 ± 0.01 l/s. The electrolytic precipitation wire is positioned 30mm downstream of the salient edge.

At 0^{o} and 5^{o} in Figures 7.2*a,b* and 7.3*a,b* the hydrogen bubbles progress parallel to the base slant angle and the white powder produced on the wall by electrolytic precipitation does not penetrate into the interior of the flow. This clearly shows that the flow remains attached for these angles. Neither an inertial separation at the slanted edge, nor a boundary layer separation on the base slant is observed.

When increasing the slant angle to 7.5^{o} (Figure 7.2*c* and 7.3*c*), the white tracer becomes visible just above the wall. This indicates the onset of boundary layer separation. According to the steps of the slant angles used in our experiments, this onset lies between 5^{o} and 7.5^{o} for the free stream velocity of 6.4 ± 0.4 cm/s.

With increasing slant angle, shown in the Figures 7.2*d,e* and 7.3*d,e,* the separation of the boundary layer moves upstream towards the salient edge. Along the limitation of the separated region, the tracer line remains straight just downstream of the separation point and then becomes progressively undulating, indicating the formation of vortices with identical sense of rotation. Further downstream, the increasing deformations of the streak surface indicate a rapid increase of the extensions of these vortices. All these observations imply the presence of an instability mechanism related to shear flows also known as Kelvin Helmholtz instability. As shown in both Figures, the development of these vortices is more rapid with increasing slant angle.

The hydrogen bubble tracer lines show that at base slant angles up to about 15^{o}, the outer flow has a tendency to flow downwards, in the direction of the rear panel (Figures 7.2*a,b,c,d*). At greater angles, in Figures 7.2*f* to 7.2*i*, the outer flow leaves the upstream panel almost tangentially. According to Section 2.3.2, this is an indication of inertial flow separation. Hence, inertial flow separation starts at a base slant angle between 15^{o} and 20^{o} for 6.4 ± 0.4 cm/s free stream velocity. Compared to the boundary layer separation, the recirculating flow above the rear panel is in this case, much more extended. The outer flow remains nearly unaffected and leaves the model tangentially near the salient edge. Only further downstream, the hydrogen bubbles visible in Figures 7.2*f,g,h,i* show a wavy motion, due to mixing in the shear layer.

Since the fluid separates at the salient edge, only the tracer particles coming from the downstream solder wire visualize the flow inside the recirculation region. Figures 7.3*f,g,h,i* indicate unsteadiness in this region. The recirculation zone appears to be divided into two main zones: one near the salient edge where low velocities lead to high tracer concentration and one further downstream where fluid is entrained from outside the recirculation zone by mixing. Since this part of the flow has not been marked with tracer, this second region appears to be dark in the Figures 7.3*f*,*g*,*h*,*i*.

Although we can distinguish on these visualizations the evolution of the flow structure with increasing slant angle, they do not give any quantitative information on the velocity and pressure field inside the separation region. However, such information would be helpful to get a more insight into the physical mechanisms which lead to separation. PIV measurements, which give an instantaneous picture of the velocity field corresponding to the flow visualizations which are shown in this section, are presented in the next section.

7.3 Investigation of the flow structure by PIV measurements

To complete the information obtained by the flow visualizations, PIV measurements were carried out under nearly identical flow conditions. The employed technique is described in more detail in chapter 4.

Experiments are performed at 6.4 ± 0.4 cm/s channel velocity (*Re = 24800*) and 0.63 ± 0.03 l/s of suction rate which is about 20% less than the suction in the visualization experiments. This reduction allowed minimizing any possible velocity overshoot in the boundary layer due to suction. During operation, this flow rate turned out to be sufficient to avoid flow separation from the leading edge for slant angles up to 35^o. Measurements were taken at 0^o, 5^o, 7.5^o, 10^o, 15^o, 20^o, 25^o and 30^o similar to the flow visualizations shown in the previous section.

The digital JAI-CCD camera, described in section 3.5.2, is used for data acquisition. The exposition time of the sensor was set to 2000 µs and the interval between two consecutive images was set to 4000 µs for capturing digital images. During the processing of the images, interrogation areas were taken as 64 x 64 pixels and the offset of the images was 16 x 16 pixels for the first correlation. For each pair of images, a second correlation was used to improve the resolution of the velocity field. Finally, the results of 10 successive image pairs were averaged to obtain the average velocity vector maps during a whole time period of 1.5 s. The visualizations in the previous section show that the frequency of vortex shedding is between 0.5 and 1s. Hence a period of 1.5 s. is enough for averaging the velocity vector maps.

Figure 7.4 to Figure 7.11 show the results of these measurements. In each figure, the first image presents the average velocity vector map of the flow field. The coordinates of the vector maps start from the lower left corner of the image. Following images show the x-component of the velocity profiles at different cross-sections. It should be emphasized that the origin of the axis of the profiles is different from the origin of the axis of the vector map. The origin of the coordinate axis of the profiles, are taken at the salient edge of the model. The y-coordinate of this axis is perpendicular to the upstream plate of the model.

The distances are non-dimensionalized by the length of the model ($l = 350\ mm$) and the velocities are non-dimensionalized by the channel velocity ($U_\infty = 6.4 \pm 0.4\ cm/s$).

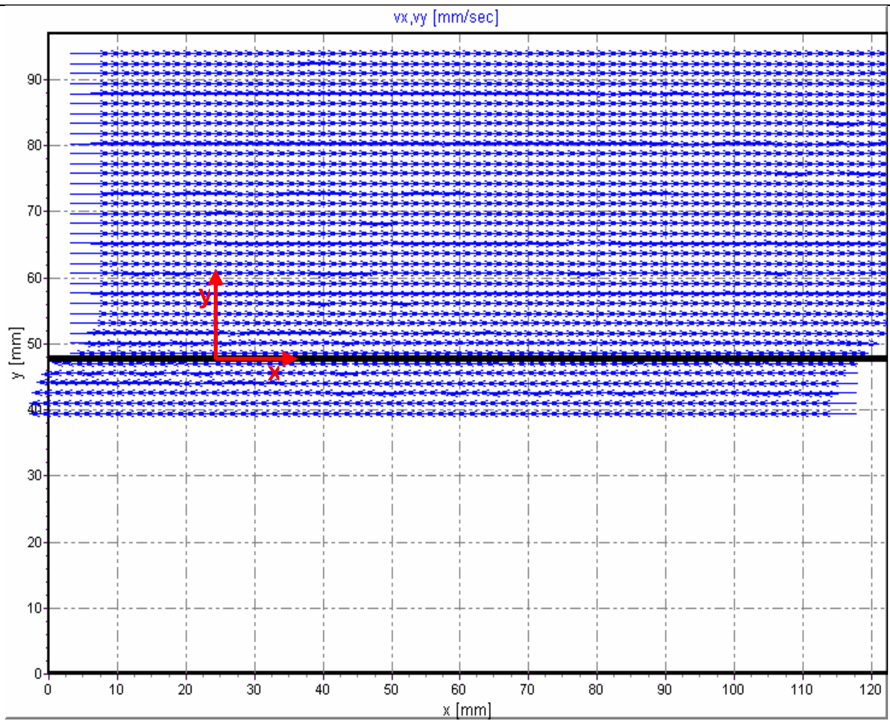

Average velocity vector map at 0^{o} of base slant angle. U_{∞}= 6.4±0.4 cm/s. Δt = 1.5 s corresponding to 10 consecutive image pairs. The red axis indicates the coordinate axis of the profiles.

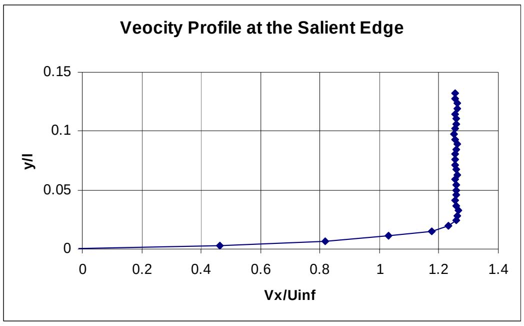

$\overline{Vx}$ component at x = *0.571 l* from the leading edge.

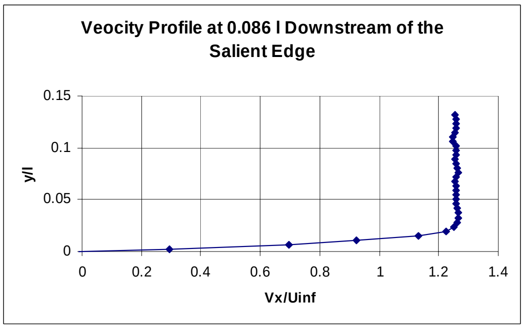

$\overline{Vx}$ component at x = *0.657 l* from the leading edge.

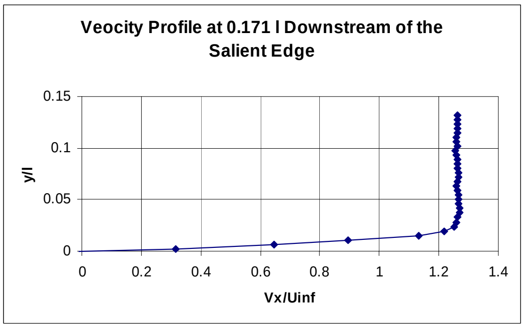

$\overline{Vx}$ component at x = *0.743 l* from the leading edge.

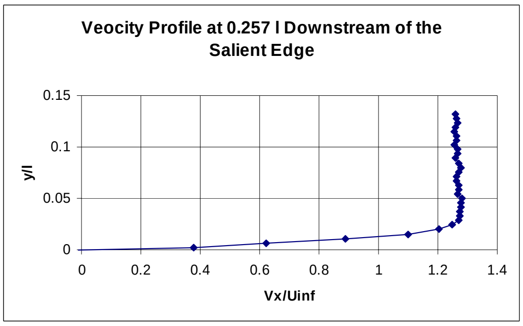

$\overline{Vx}$ component at x = *0.828 l* from the leading edge.

Figure 7.4: Average velocity vector map and velocity profiles of x-component of velocity at various streamwise positions. Base slant angle is 0^{o} degrees. U_{∞} = 6.4±0.4 cm/s. The time average is taken during 1.5 s corresponding to 10 consecutive image pairs. The coordinate axis of the velocity profiles start from the salient edge.

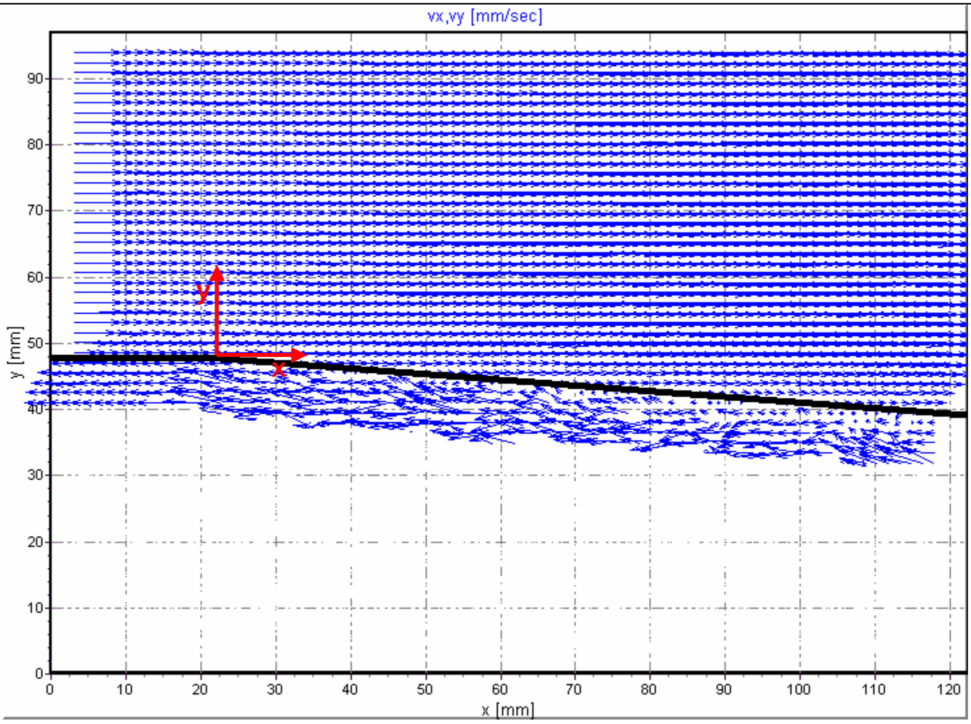

Average velocity vector map at 5° of base slant angle. U_∞= 6.4±0.4 cm/s. Δt = 1.5 s corresponding to 10 consecutive image pairs. The red axis indicates the coordinate axis of the profiles.

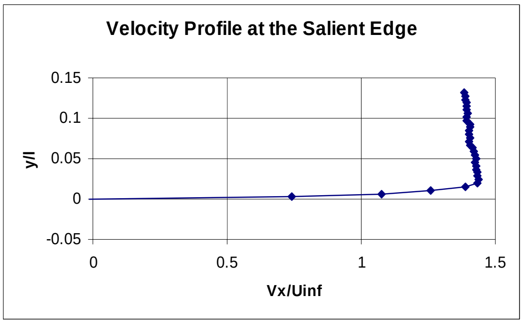

$\overline{Vx}$ component at $x = 0.571\, l$ from the leading edge.

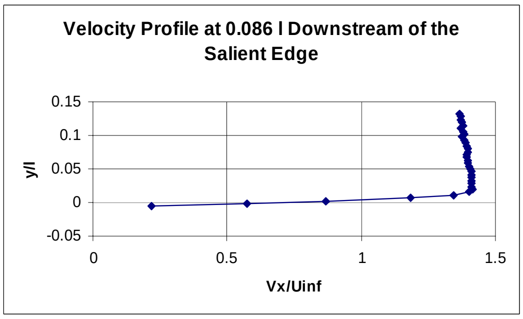

$\overline{Vx}$ component at $x = 0.657\, l$ from the leading edge.

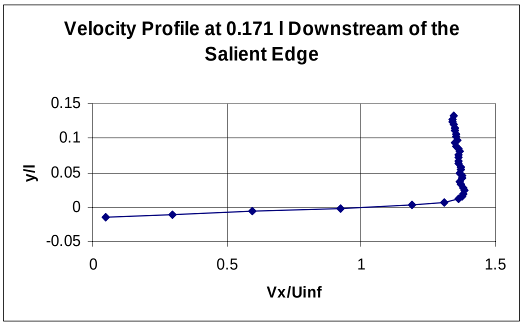

$\overline{Vx}$ component at $x = 0.743\, l$ from the leading edge.

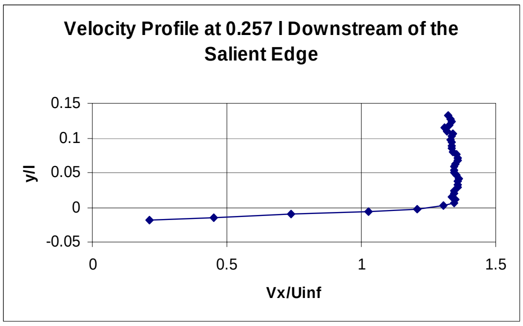

$\overline{Vx}$ component at $x = 0.828\, l$ from the leading edge.

Figure 7.5: Average velocity vector map and velocity profiles of x-component of velocity at various streamwise positions. Base slant angle is 5° degrees. U_∞ = 6.4±0.4 cm/s. The time average is taken during 1.5 s corresponding to 10 consecutive image pairs. The coordinate axis of the velocity profiles start from the salient edge.

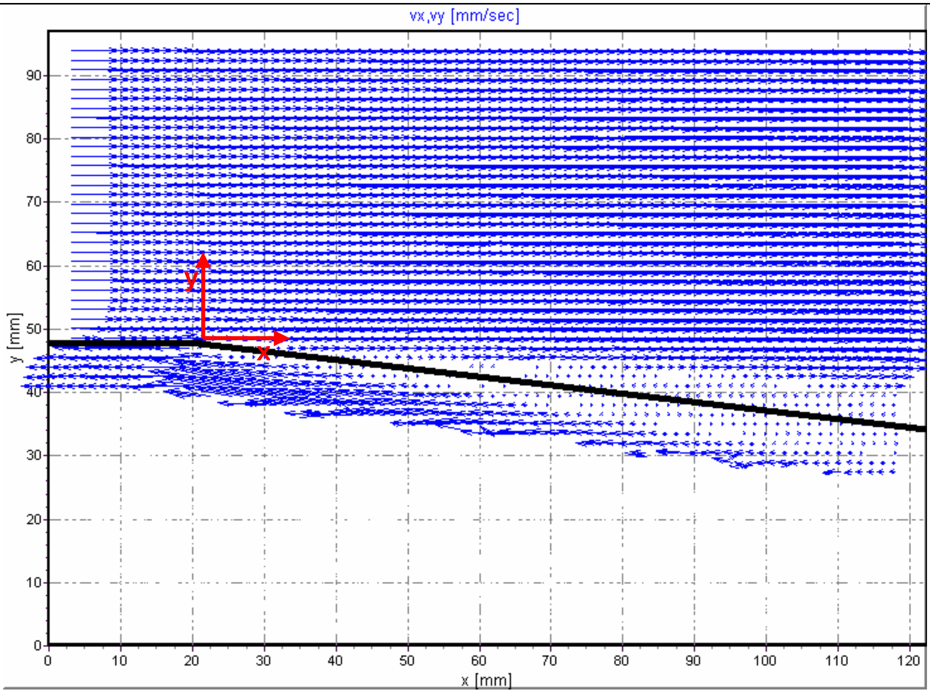

Average velocity vector map at 7.5° of base slant angle. U_∞= 6.4±0.4 cm/s. Δt = 1.5 s corresponding to 10 consecutive image pairs. The red axis indicates the coordinate axis of the profiles.

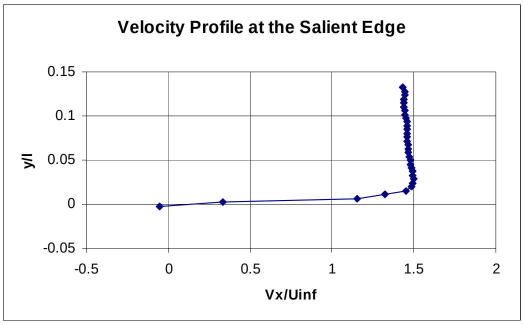

$\overline{Vx}$ component at x = *0.571 l* from the leading edge.

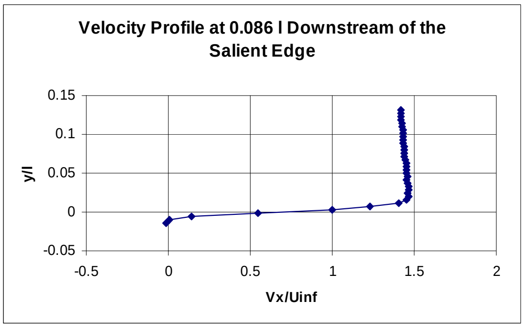

$\overline{Vx}$ component at x = *0.657 l* from the leading edge.

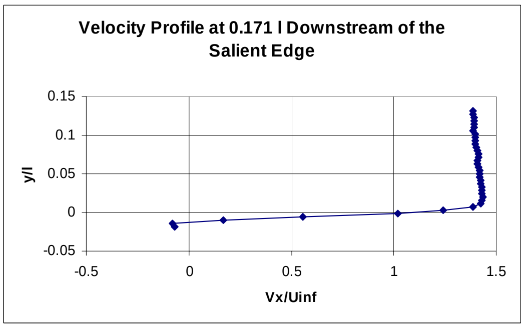

$\overline{Vx}$ component at x = *0.743 l* from the leading edge.

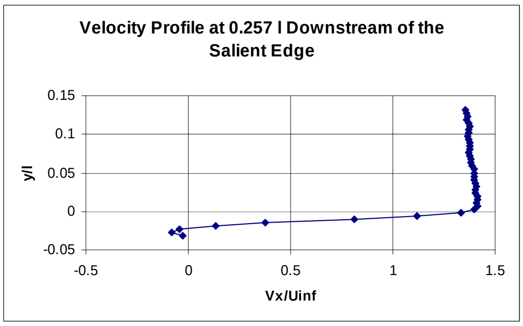

$\overline{Vx}$ component at x = *0.828 l* from the leading edge.

Figure 7.6: Average velocity vector map and velocity profiles of x-component of velocity at various streamwise positions. Base slant angle is 7.5° degrees. U_∞ = 6.4±0.4 cm/s. The time average is taken during 1.5 s corresponding to 10 consecutive image pairs. The coordinate axis of the velocity profiles start from the salient edge.

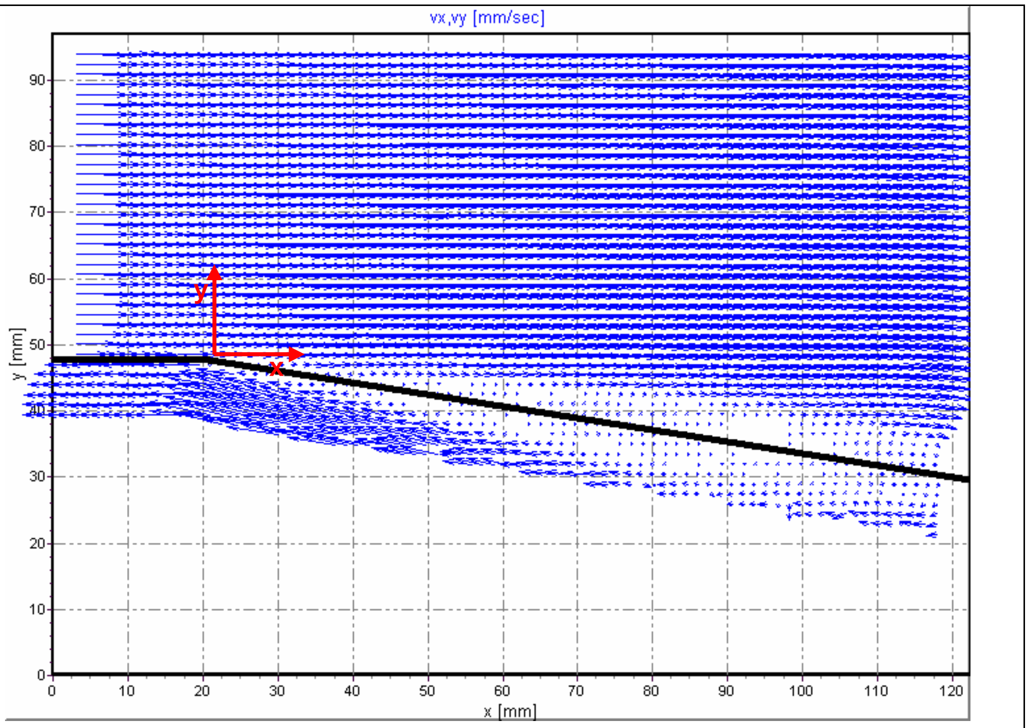

Average velocity vector map at 10^{o} of base slant angle. U_{∞}= 6.4±0.4 cm/s. Δt = 1.5 s corresponding to 10 consecutive image pairs. The red axis indicates the coordinate axis of the profiles.

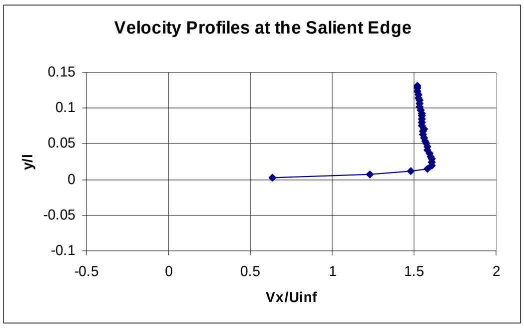

$\overline{Vx}$ component at x = *0.571 l* from the leading edge.

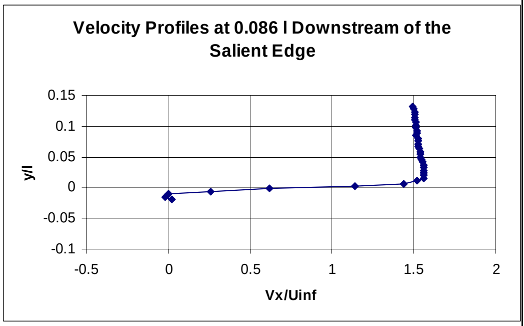

$\overline{Vx}$ component at x = *0.657 l* from the leading edge.

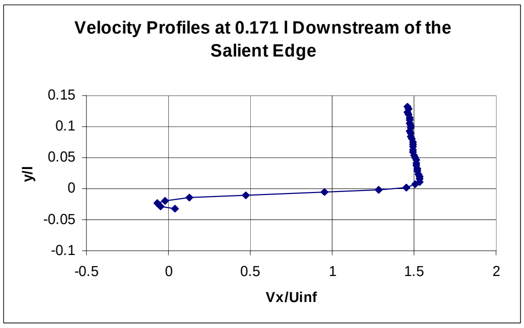

$\overline{Vx}$ component at x = *0.743 l* from the leading edge.

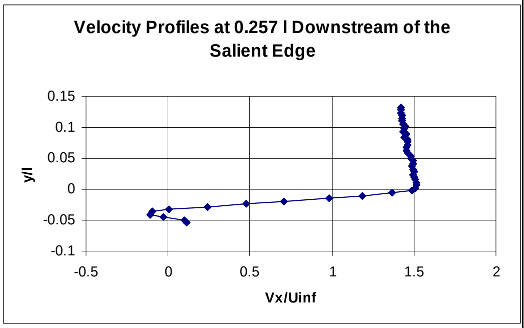

$\overline{Vx}$ component at x = *0.828 l* from the leading edge.

Figure 7.7: Average velocity vector map and velocity profiles of x-component of velocity at various streamwise positions. Base slant angle is 10^{o} degrees. U_{∞} = 6.4±0.4 cm/s. The time average is taken during 1.5 s corresponding to 10 consecutive image pairs. The coordinate axis of the velocity profiles start from the salient edge.

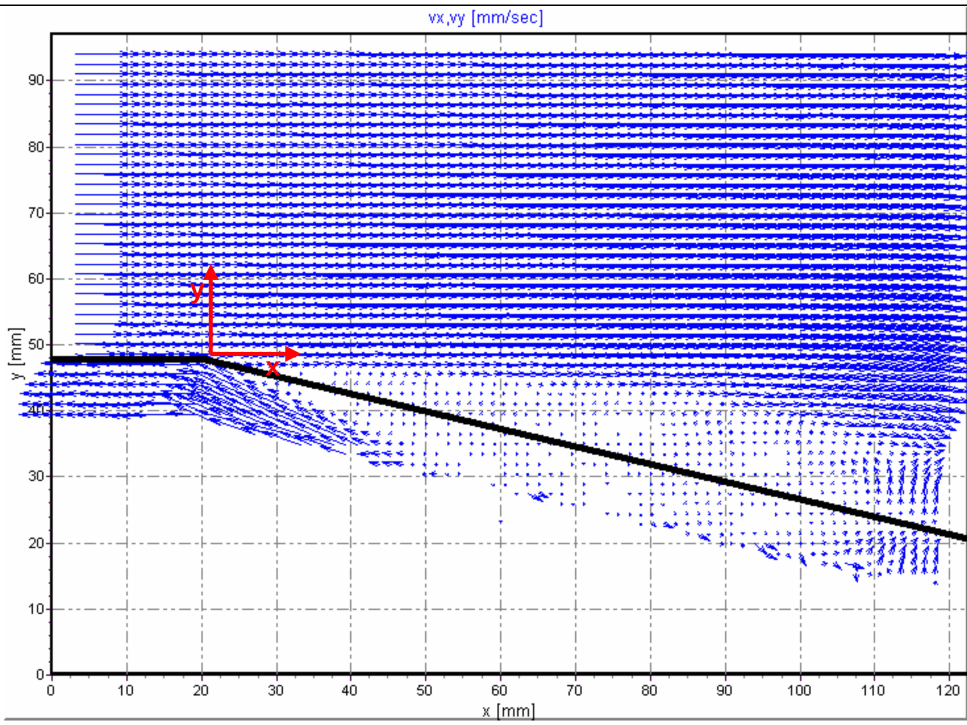

Average velocity vector map at 15° of base slant angle. U_∞= 6.4±0.4 cm/s. Δt = 1.5 s corresponding to 10 consecutive image pairs. The red axis indicates the coordinate axis of the profiles.

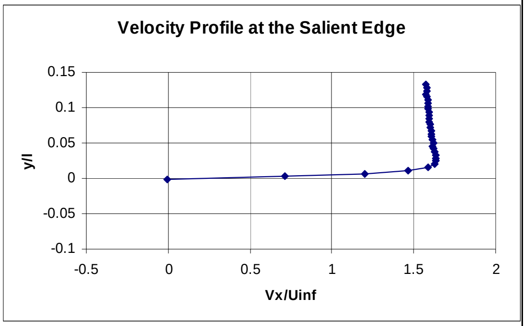

$\overline{Vx}$ component at *x = 0.571 l* from the leading edge.

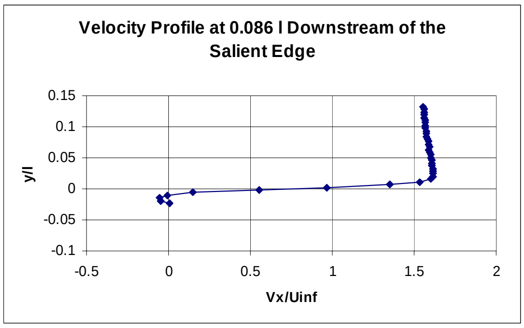

$\overline{Vx}$ component at *x = 0.657 l* from the leading edge.

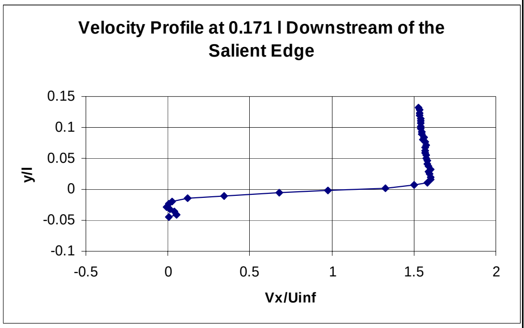

$\overline{Vx}$ component at *x = 0.743 l* from the leading edge.

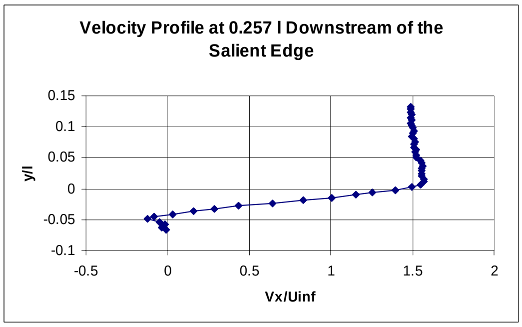

$\overline{Vx}$ component at *x = 0.828 l* from the leading edge.

Figure 7.8: Average velocity vector map and velocity profiles of x-component of velocity at various streamwise positions. Base slant angle is 15° degrees. U_∞ = 6.4±0.4 cm/s. The time average is taken during 1.5 s corresponding to 10 consecutive image pairs. The coordinate axis of the velocity profiles start from the salient edge.

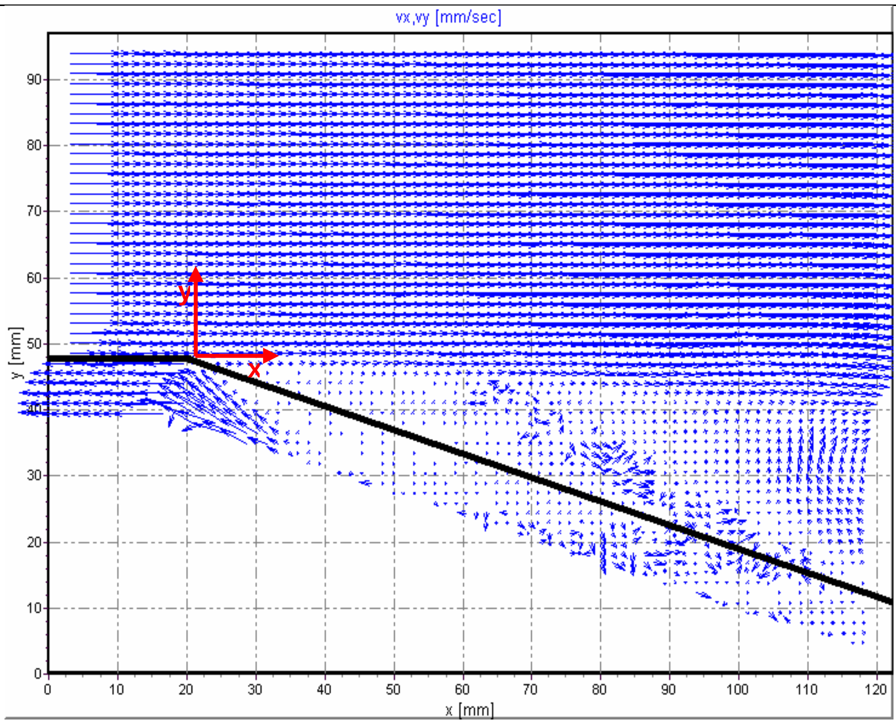

Average velocity vector map at 20^{o} of base slant angle. U_{∞}= 6.4±0.4 cm/s. Δt = 1.5 s corresponding to 10 consecutive image pairs. The red axis indicates the coordinate axis of the profiles.

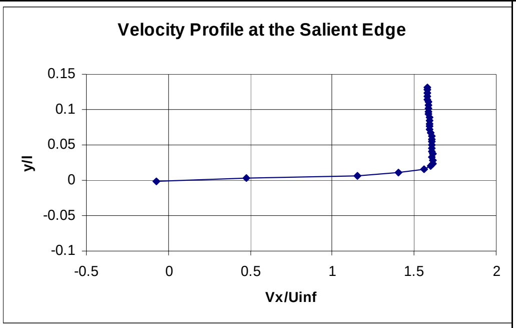

$\overline{Vx}$ component at x = *0.571 l* from the leading edge.

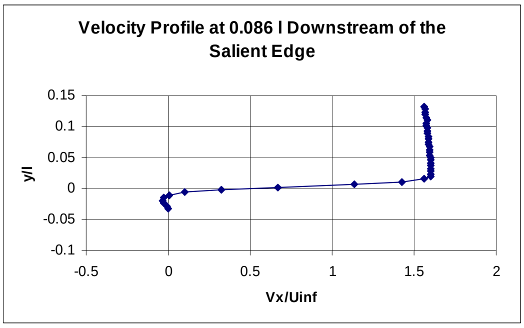

$\overline{Vx}$ component at x = *0.657 l* from the leading edge.

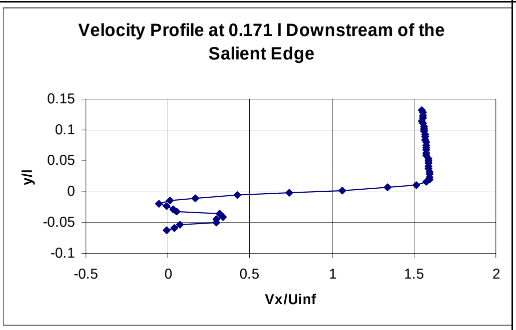

$\overline{Vx}$ component at x = *0.743 l* from the leading edge.

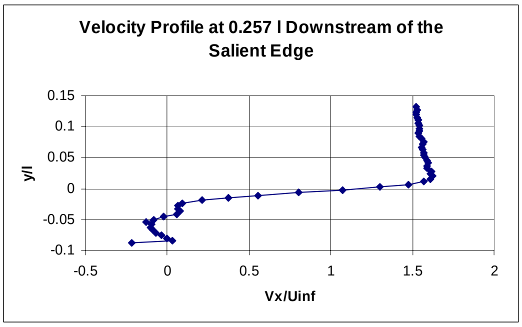

$\overline{Vx}$ component at x = *0.828 l* from the leading edge.

Figure 7.9: Average velocity vector map and velocity profiles of x-component of velocity at various streamwise positions. Base slant angle is 20^{o} degrees. U_{∞} = 6.4±0.4 cm/s. The time average is taken during 1.5 s corresponding to 10 consecutive image pairs. The coordinate axis of the velocity profiles start from the salient edge.

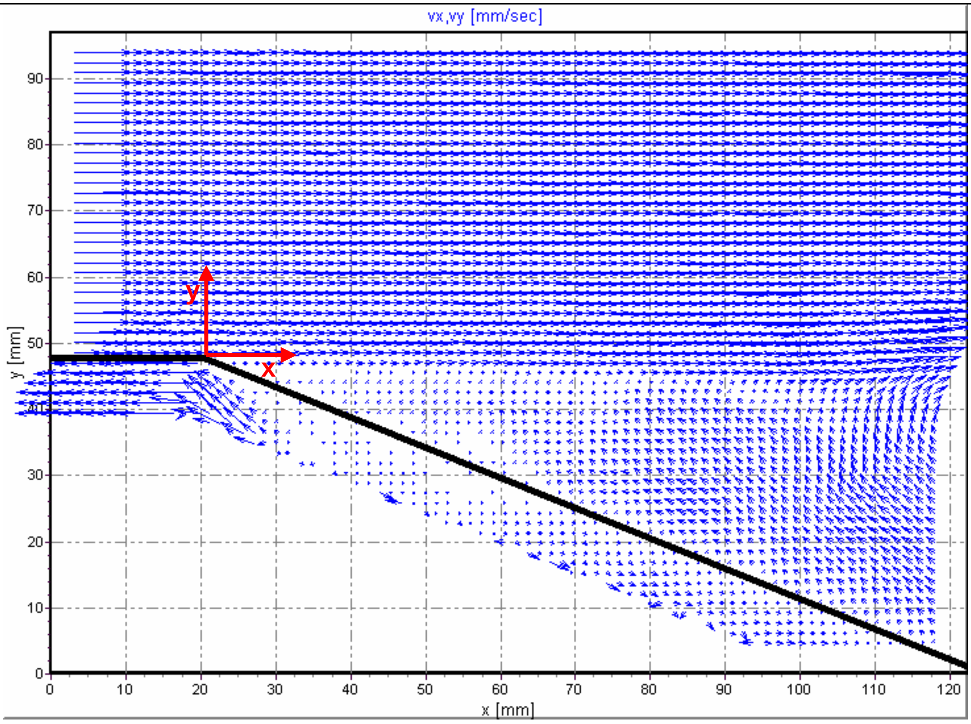

Average velocity vector map at 25° of base slant angle. U_∞= 6.4±0.4 cm/s. Δt = 1.5 s corresponding to 10 consecutive image pairs. The red axis indicates the coordinate axis of the profiles.

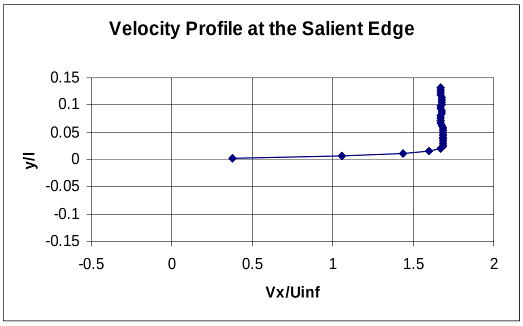

$\overline{Vx}$ component at x = *0.571 l* from the leading edge.

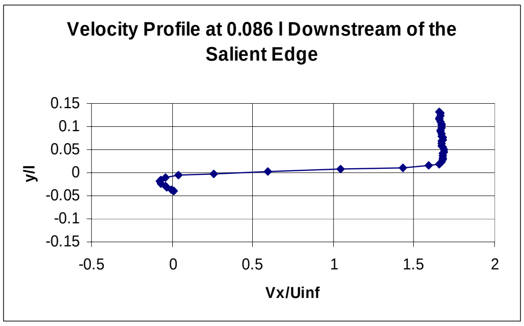

$\overline{Vx}$ component at x = *0.657 l* from the leading edge.

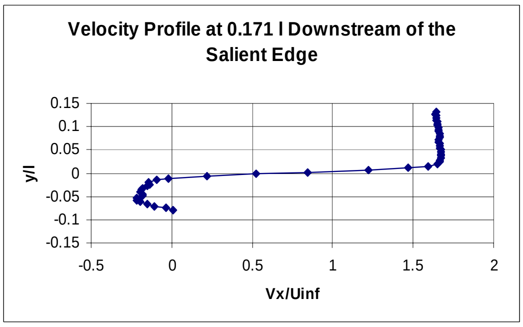

$\overline{Vx}$ component at x = *0.743 l* from the leading edge.

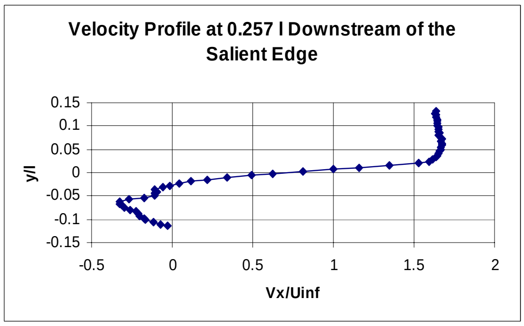

$\overline{Vx}$ component at x = *0.828 l* from the leading edge.

Figure 7.10: Average velocity vector map and velocity profiles of x-component of velocity at various streamwise positions. Base slant angle is 25° degrees. U_∞ = 6.4±0.4 cm/s. The time average is taken during 1.5 s corresponding to 10 consecutive image pairs. The coordinate axis of the velocity profiles start from the salient edge.

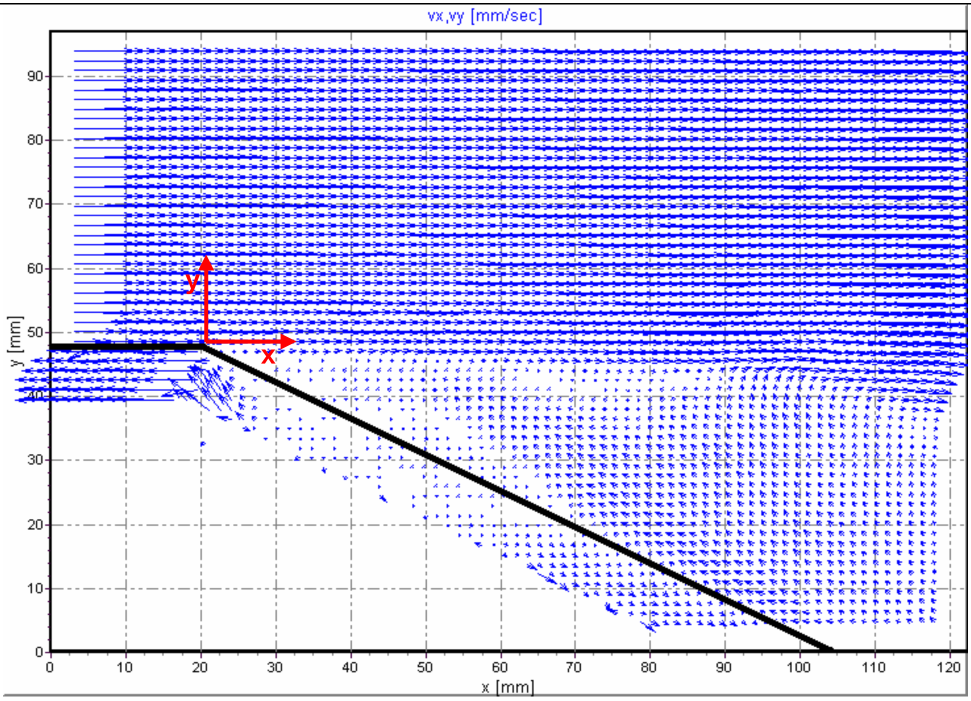

Average velocity vector map at 30° of base slant angle. U_∞= 6.4±0.4 cm/s. Δt = 1.5 s corresponding to 10 consecutive image pairs. The red axis indicates the coordinate axis of the profiles.

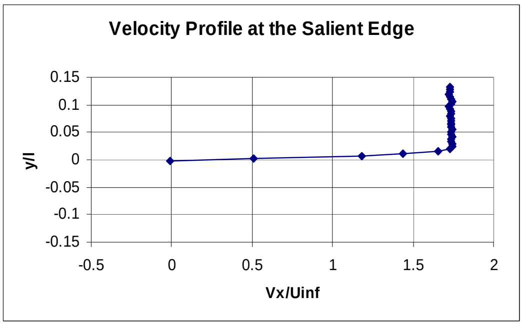

$\overline{Vx}$ component at x = *0.571 l* from the leading edge.

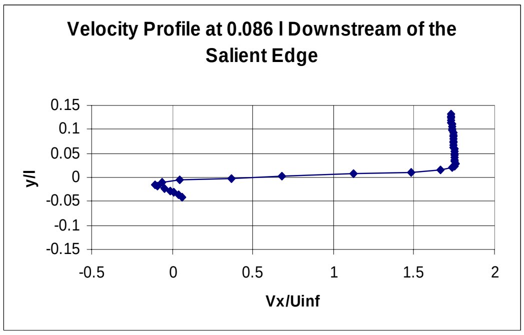

$\overline{Vx}$ component at x = *0.657 l* from the leading edge.

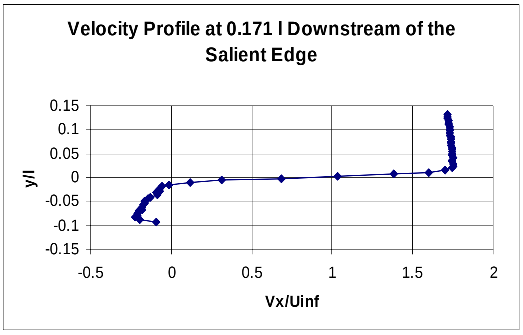

$\overline{Vx}$ component at x = *0.743 l* from the leading edge.

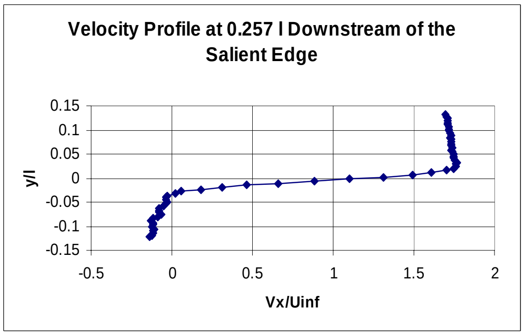

$\overline{Vx}$ component at x = *0.828 l* from the leading edge.

Figure 7.11: Average velocity vector map and velocity profiles of x-component of velocity at various streamwise positions. Base slant angle is 30° degrees. U_∞ = 6.4±0.4 cm/s. The time average is taken during 1.5 s corresponding to 10 consecutive image pairs. The coordinate axis of the velocity profiles start from the salient edge.

Qualitatively, the vector maps are in good agreement with the flow visualizations presented before. Boundary layer separation starts between 5^o and 7.5^o, while inertial separation is clearly developed at 20^o. The reduction of the suction rate didn't change the evolution of the flow separation with increasing slant angle. Besides this, the measurements clearly show the big velocity difference between the flow inside and outside the region with separated flow. The velocities inside the recirculation region near the separation line are about 10 to 100 times smaller than the free-stream velocity. Only in the downstream direction the velocity inside the recirculation zone increases indicating the increasing effect of mixing in the shear layer.

The velocity profiles of the axial velocity component *Vx* at different axial positions downstream of the salient edge also clearly illustrate this behavior. In every configuration with separation the reversed flow appears after the separation point. Further downstream, multiple inflection points appear which indicate the presence of vortices due to viscous entrainment and instability of the shear flow. Since these profiles are time averaged, a direct physical interpretation by using these vortical structures is not possible.

If we consider the instantaneous measurements instead of time averaging, we observe qualitatively the same results. Figure 7.12-14 illustrate sample instantaneous measurements at 5^o, 7.5^o and 30^o degrees respectively. In the velocity profile plots, the distances are non-dimensionalized by the model length ($l = 350\ mm$) and the velocities are non-dimensionalized by the channel velocity ($U_\infty = 6.4 \pm 0.4\ cm/s$). The origin of the coordinate axis is placed at the salient edge as before.

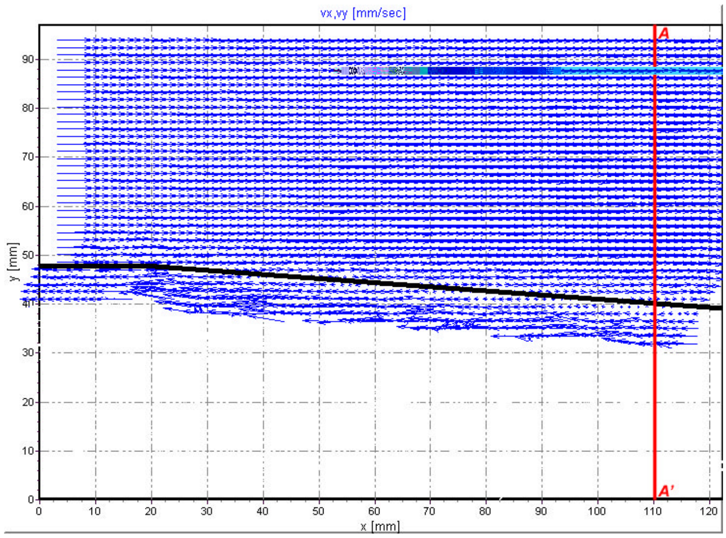

Instantaneous velocity vector map for 5° of base slant angle. U_∞= 6.4±0.4 cm/s.

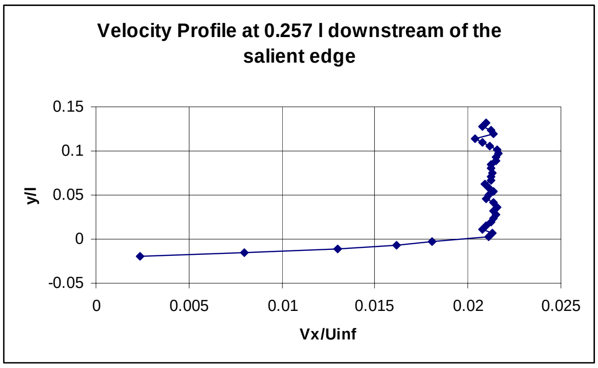

V_x at $x = 0.828\ l$ from the leading edge (Section *AA'*).

Figure 7.12: Instantaneous velocity vector map and velocity profile of x-component of velocity at $x = 0.828\ l$ from the leading edge. Base slant angle is 5° degrees. U_∞ = 6.4±0.4 cm/s. The coordinate axis of the velocity profiles start from the salient edge.

Both the electrolytic precipitation visualizations and PIV measurements show that flow does not separate at 5° of base slant angle.

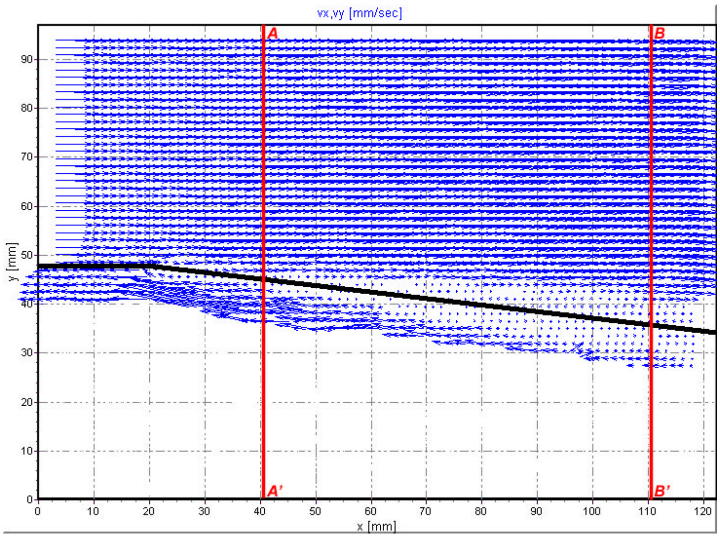

Instantaneous velocity vector map for 5^o of base slant angle. U_∞= 6.4±0.4 cm/s.

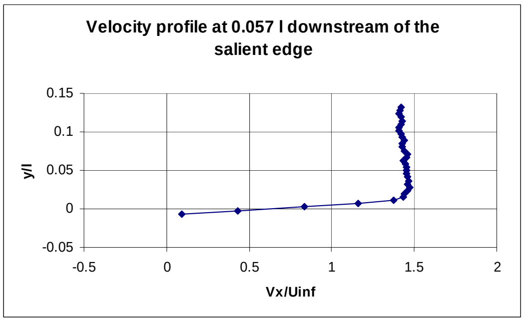

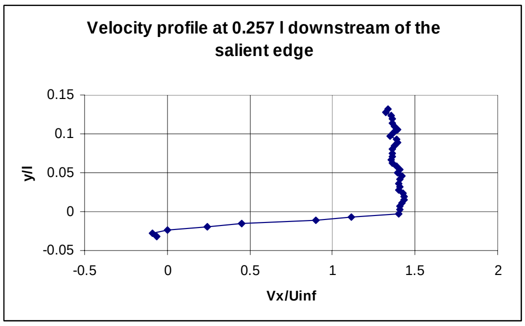

V_x at $x = 0.628\ l$ from the leading edge (Section *AA'*).

V_x at $x = 0.828\ l$ from the leading edge (Section *BB'*).

Figure 7.13: Instantaneous velocity vector map and velocity profile of x-component of velocity at points upstream and downstream of separation. Base slant angle is 7.5^o degrees. U_∞ = 6.4±0.4 cm/s. The coordinate axis of the velocity profiles start from the salient edge.

At a base slant angle of 7.5^o, visualizations show that separation starts over the rear plate of the model. In the velocity profile at $x = 0.057\ l$ downstream of the salient edge, no indications of flow separation are visible. Further downstream, at $x = 0.257\ l$ from the salient edge, the velocity profile shows reversed flow with separation. Since the separation starts downstream of the salient edge, this is a boundary layer separation in agreement with the observations in section 7.2.

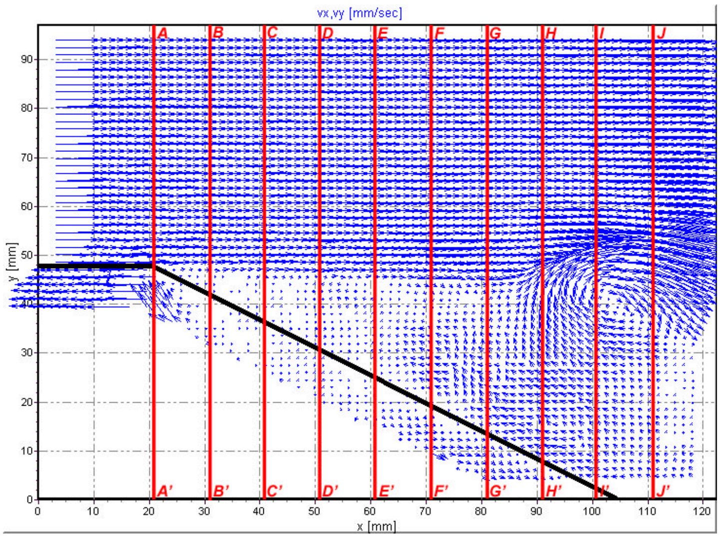

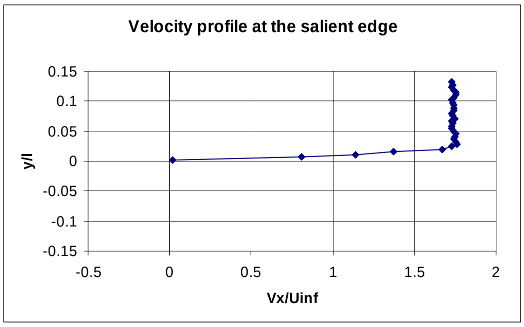

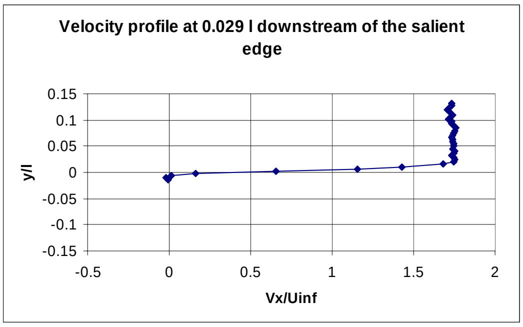

V_x at $x = 0.571\ l$ from the leading edge (Section *AA'*).

V_x at $x = 0.600\ l$ from the leading edge (Section *BB'*).

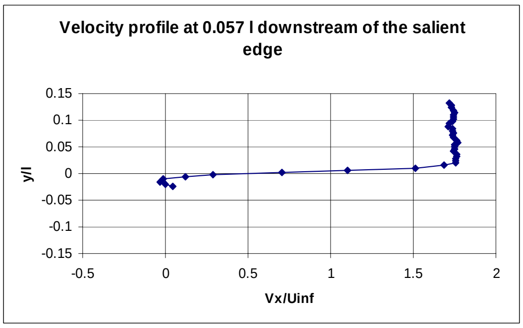

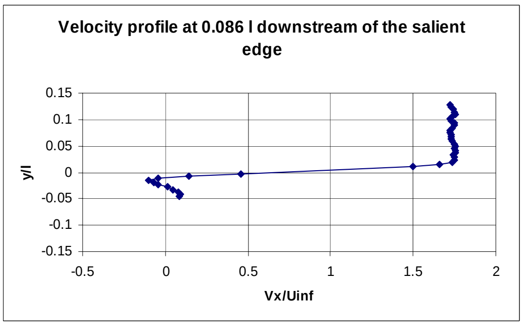

V_x at $x = 0628.\ l$ from the leading edge (Section *CC'*).

V_x at $x = 0.657\ l$ from the leading edge (Section *DD'*).

Figure 7.14: Instantaneous velocity vector map and velocity profile of x-component of velocity at various streamwise positions. Base slant angle is 30^o degrees. U_∞ = 6.4±0.4 cm/s. The coordinate axis of the velocity profiles start from the salient edge.

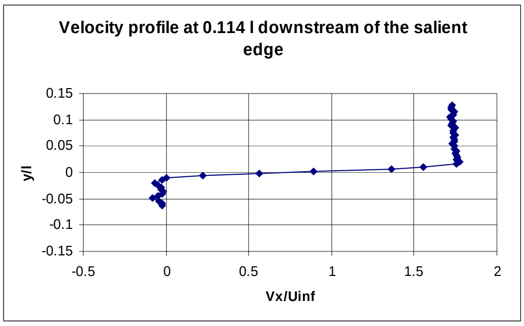

V_x at $x = 0.685\ l$ from the leading edge (Section *EE'*).

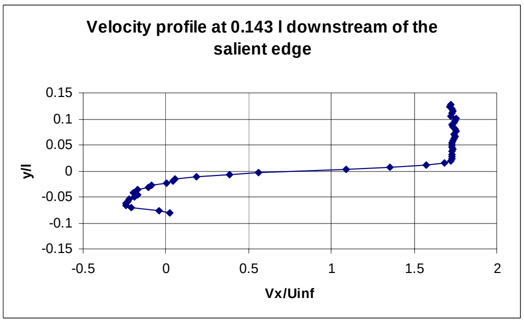

V_x at $x = 0.714\ l$ from the leading edge (Section *FF'*).

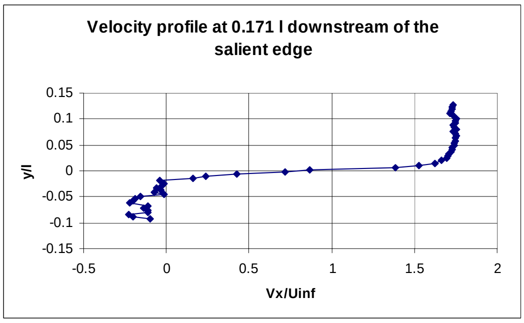

V_x at $x = 0.742\ l$ from the leading edge (Section *GG'*).

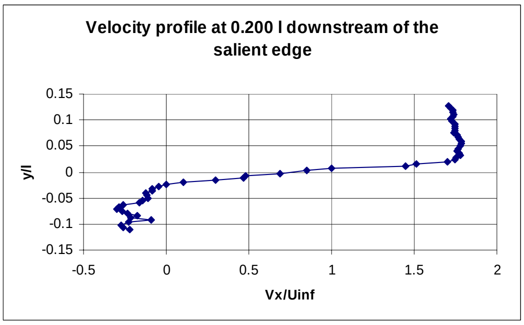

V_x at $x = 0.771\ l$ from the leading edge (Section *HH'*).

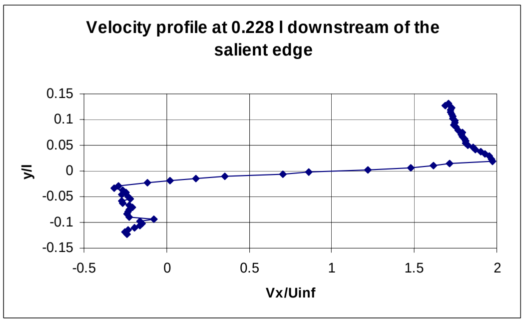

V_x at $x = 0.799\ l$ from the leading edge (Section *II'*).

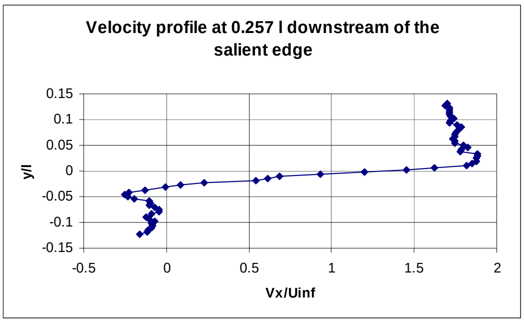

V_x at $x = 0.828\ l$ from the leading edge (Section *JJ'*).

Figure 7.14 (continued): Instantaneous velocity vector map and velocity profile of x-component of velocity at various streamwise positions. Base slant angle is 30^o degrees. U_∞ = 6.4±0.4 cm/s. The coordinate axis of the velocity profiles start from the salient edge.

At a base slant angle of 30^o with inertial separation, the velocity profiles are presented in Figure 7.14. Negative velocity components start just after the salient edge and increase in every streamwise position. In particular, for the profiles at downstream positions, several inflection points are visible in the profiles. These inflection points are inside the separation region and they indicate the presence of vortices due to viscous entrainment and instability of the shear flow. They highlight the complex dynamics of the separated region and illustrate in particular the difficulty to get useful signals for control devices in this region. However, in order to simplify the analysis, we used as a first approach, the time averaged velocity field to get information on the flow behavior inside the separation region. In the next section we present the results of this approach.

7.4 Investigation of boundary layer flow separation with the Falkner-Skan model

The potential flow analysis presented in section 2.4.2, shows that the pressure varies in the radial direction with the salient edge as the origin. Therefore we used the variation of the radial velocity component along the outer edge of the boundary layer to estimate the imposed pressure gradient. The velocity gradients are evaluated from time averaged PIV measurements along the line *AA'*, as shown in Figure 7.15.

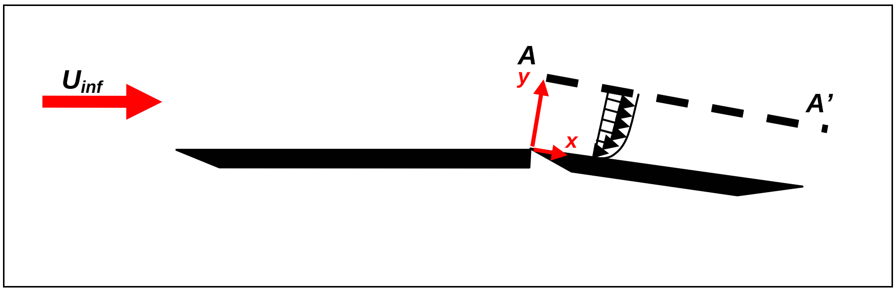

Figure 7.15: To evaluate the velocity gradient parameter *m* the external velocity is measured from PIV vector maps along the line *AA'*.

Figure 7.16 shows the results of the velocity measurements along the section AA' for small base slant angles.

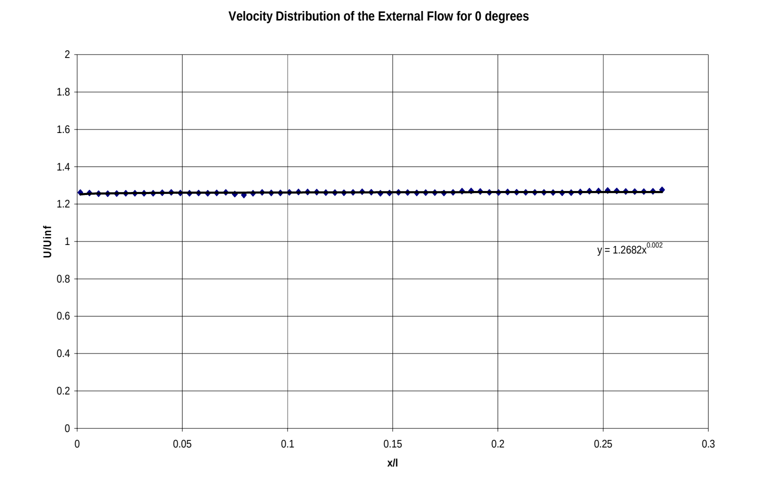

$$u_e(x) = 1.2682x^{0.002}$$
$$m = 0.002$$
$$\beta = 0.004\,rad$$

(a) 0^o degrees of base slant angle. m=0.002, β=0.004. Flow is not separated.

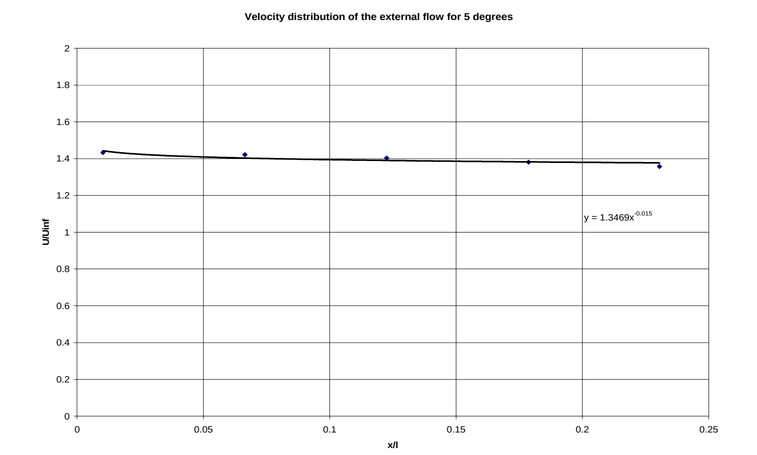

$$u_e(x) = 1.3469x^{-0.015}$$
$$m = -0.015$$
$$\beta = -0.031rad$$

(b) 5^o degrees of base slant angle. m=-0.015, β=-0.031. Flow is not separated.

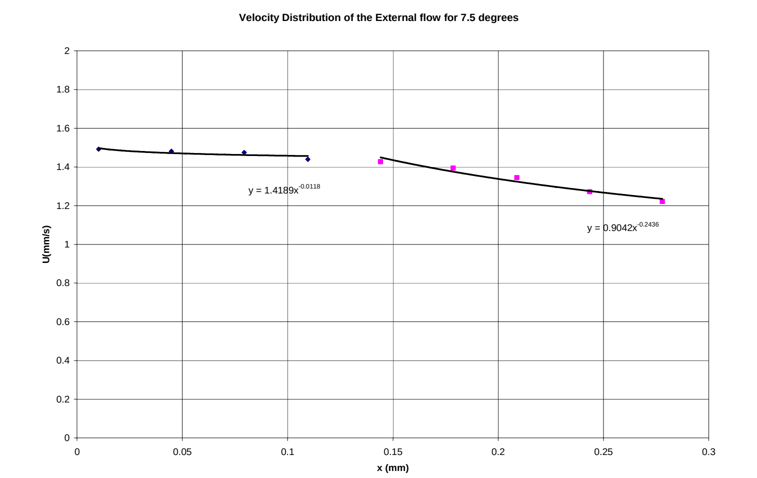

$$u_e(x) = 1.3994x^{-0.0154}$$
$$m = -0.0154$$
$$\beta = -0.0312rad$$

$$u_e(x) = 0.9042x^{-0.2436}$$
$$m = -0.2436$$
$$\beta = -0.6441rad$$

(c) 7.5^o degrees of base slant angle. m=-0.0154, β=-0.0312 before separation and m = -0.2436, β = -0.6441 after separation.

Figure 7.16: Potential flows, outside the boundary layer for various slant angles.

At slant angles, smaller than 7.5^{o}, without separation, the velocity law of the flow adjacent to the edge of the boundary layer, parallel to the wall can be represented in the form of equation 2.8. However, at a base slant angle of 7.5 degrees the velocity law changes for $x/l \geq 0.11$. Due to flow separation and additional adverse pressure gradients imposed by circulation around the model, the simple corner flow model can no more represent the flow with slant angles greater than 7.5^{o}. In Figure 7.17*c* two distinct branches appear due to flow separation indicating the limitations of the model. Hence, modeling the flow with potential corner flow to estimate the pressure gradient parameter is only valid up to separation point.

Using equation 2.15, the local pressure gradient parameter for different slant angles can be estimated up to the point of separation for small base slant angles. The corresponding results are plotted in Figure 7.17. In all plots, the axial position is non-dimensionalized with the length of the model ($l = 350\ mm$).

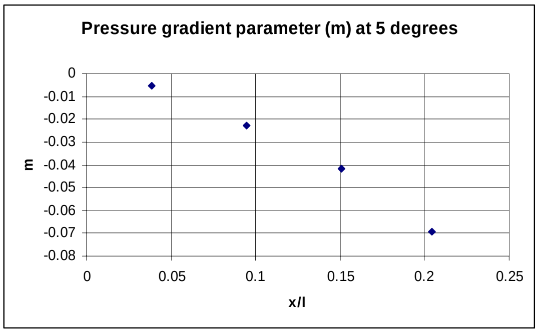

5° of base slant angle, without separation.

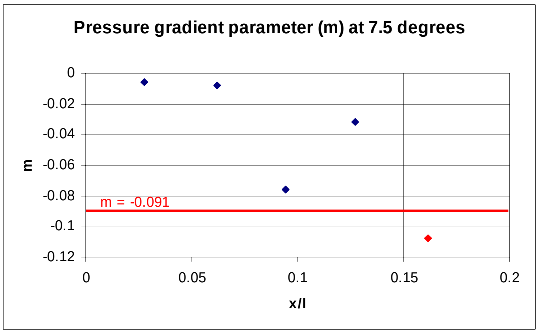

7.5° of slant angle. Separation appears between $x = 0.13\, l$ and $x = 0.16\, l$ (~44 and 56 mm)

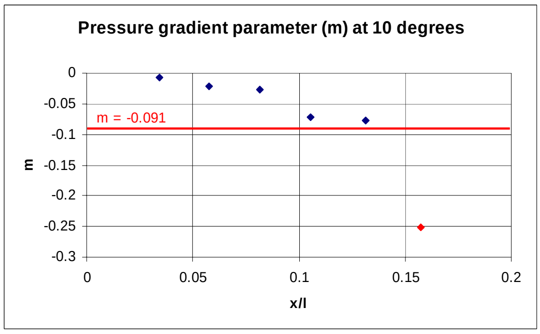

10° of slant angle. Separation appears between $x = 0.13\, l$ and $x = 0.16\, l$ (~46 and 55 mm)

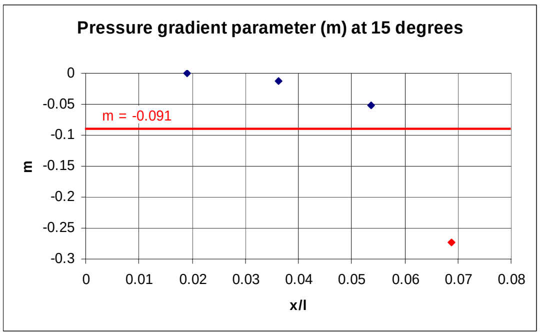

15° of slant angle. Separation appears between $x = 0.07\, l$ and $x = 0.08\, l$ (~18 and 24 mm)

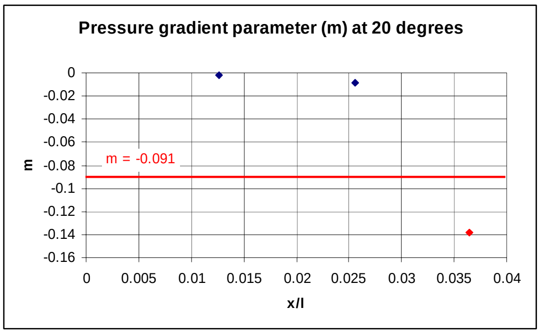

20° of slant angle. Separation appears between $x = 0.03\, l$ and $x = 0.04\, l$ (~9 and 13 mm).

Figure 7.17: Local pressure gradient parameter m for various base slant angles. The red line indicates the pressure gradient parameter value for which separation starts ($m = -0.091$) according to the solution of Falkner-Skan equation.

Qualitatively the calculated values of the pressure gradient parameter *m* are in good agreement with the flow visualizations presented in Figure 7.4. As the slant angle increases, the separation line moves gradually towards the salient edge. At 15^o degrees, the separation point lies very close to the salient edge (less than 10% of the chord length). However, as discussed in chapter 2, the Falkner-Skan solution is not applicable near the salient edge, since the velocity tends to infinity if *r* tends to zero.

For slant angles greater than about 15^o, the separation point remains fixed on the salient edge. In summary this confrontation seems to indicate the validity of the critical angle of 18^o given by the Falkner-Skan theory. In the case of our model the flow is unfortunately more complex. Results of the visualizations with increased Reynolds number are presented in the next section to show this complexity.

7.5 Evolution of flow separation with increasing Reynolds number

In this section, we study the influence of increasing Reynolds number on the structure of flow separations. As in the case of the visualizations presented in section 7.2, the hydrogen bubble technique was used in combination with the electrolytic precipitation technique. The hydrogen bubbles were generated at 5 Hz and with 50% duty cycle. The positions of the solder wires were the same as in Figure 7.1. The suction rate was adjusted to 1.21 ± 0.06 l/s to guarantee attached flow over the model up to a maximum slant angle of 40^o. The kinematic viscosity of the water inside the channel was 0.99×10^{-6} m^2/s at a temperature of 20 ± 0.2^o C [Weast, 1962]. The corresponding Reynolds number, based on the chord length is 50500.

Figure 7.18 illustrates the evolution of the flow structure inside the separated flow region with increasing slant angle, using the solder wire downstream of the salient edge.

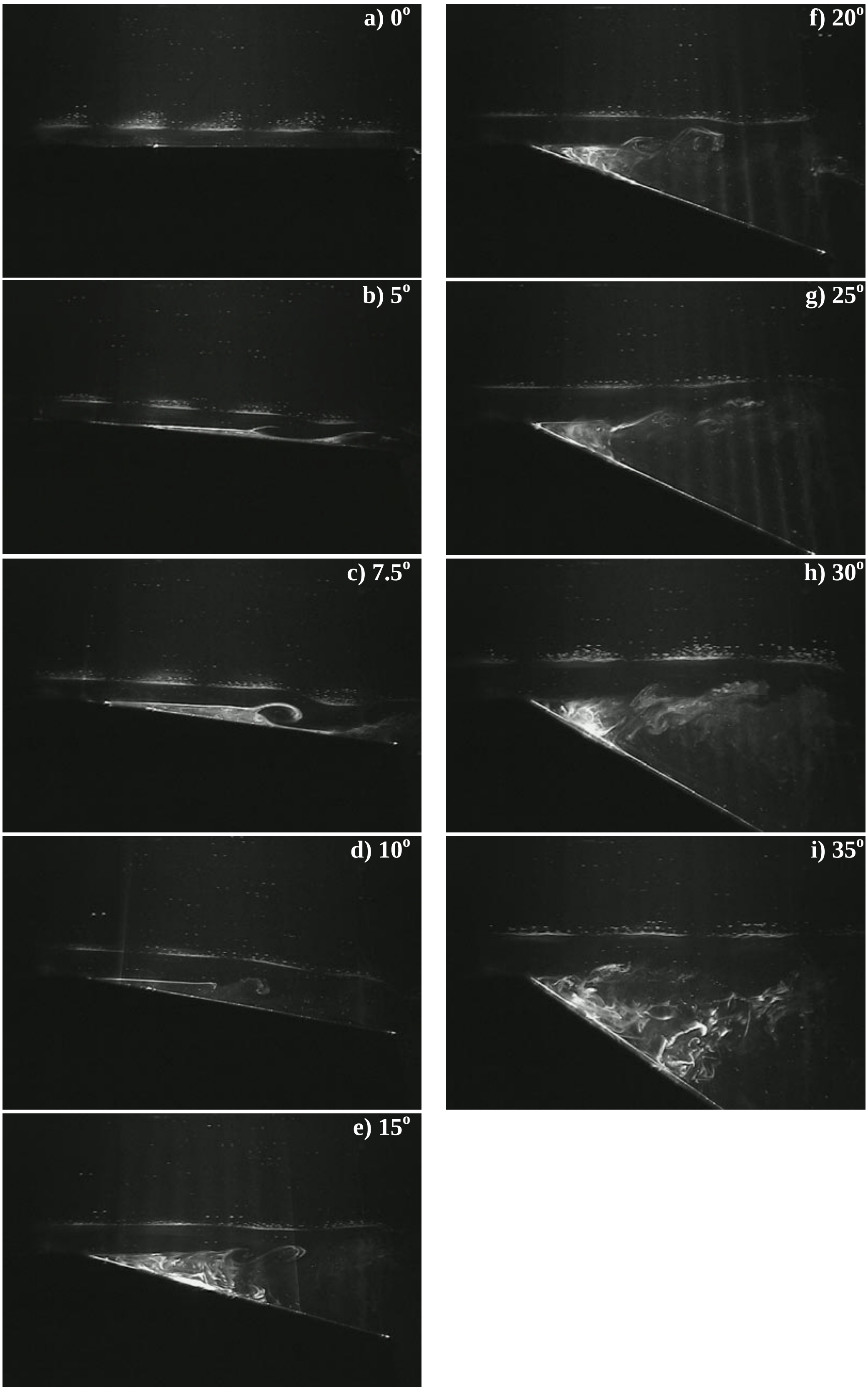

Figure 7.18: Visualization of flow separation from the salient edge by hydrogen bubbles and electrolytic precipitation techniques for increasing slant angles. Velocity is 14.3 ± 0.9 cm/s, the applied suction rate at the leading edge is 1.21 ± 0.06 l/s. The electrolytic precipitation wire is positioned 20mm downstream of the salient edge.

At 0^o in Figure 7.18*a*, the white tracer does not penetrate into the flow and the hydrogen bubble lines are parallel to the surface. This shows that the flow is attached to the surface of the model.

Beginning from 5^o of slant angle, in Figure 7.18*b*, the white tracer becomes visible. At this angle, the flow is just separated from the surface. However, hydrogen bubble lines are still following the surface. This indicates that only boundary layer separation exists at this angle. According to the steps of the slant angles used in our experiments, the beginning of the boundary layer separation lies between 0^o and 5^o for the free stream velocity of 14.3 ± 0.9 cm/s. (More precisely, no flow separation was observed at 4^o of base slant angle as shown in Figure 7.19. As a result, separation starts between 4^o and 5^o)

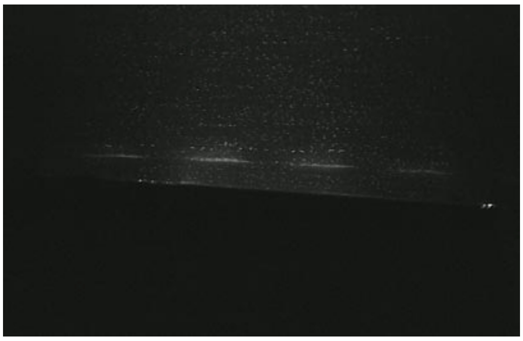

Figure 7.19: Visualization by using hydrogen bubble and electrolytic precipitation techniques at 4^o of slant angle. $U_\infty = 14.3 \pm 0.9$ *cm/s*. Suction rate at the leading edge is 1.21 ± 0.06 l/s. The solder wire is positioned 20mm downstream of the salient edge.

Increasing slant angles in the Figures 7.18*c,d,e* indicate that the boundary layer separation moves upstream towards the salient edge up to 15^o of slant angle. For slant angles greater than 15^o, both the white streak surfaces with tracer powder and the hydrogen bubble tracers become parallel to the upstream plate of the model. This is the indication of the onset of inertial separation. This onset lies between 10^o and 15^o degrees of base slant.

At a slant angle of 5^o in Figure 7.1*e*, co-rotating vortices begin to appear. These vortices indicate the existence of a Kelvin-Helmholtz instability as in the experiments with *Re = 24800*. However, now the growth rate is more important leading more rapidly to the unsteadiness of separated flow. For further increasing angles, the shear layer instability growth is so strong that the white tracer rapidly begin to merge with external flow (Figure 7.18*f,g,h,i*).

The most important difference between the high and low Reynolds number cases is the critical angle for separation. Both boundary layer and inertial separation started earlier in the high Reynolds number case. At *Re = 24800* boundary layer separation and the inertial separation started at ~7.5^o and ~18^o respectively, whereas at *Re=50500*, the corresponding angles are ~4.5^o and ~13^o. The variation of the flow rate of suction does not seem to be at the origin of this important difference since several tests at constant Reynolds number with different suction rate did not show such a significant change of flow behavior. A major reason for this observation might be the increase of the adverse pressure gradient due to the increase in circulation with Reynolds number. According to the tests with different flow rates of suction this parameter does not have much influence on the flow separation in this configuration. In order to find out the Reynolds number dependency of the critical angles for both types of separation, a more exhaustive study of the behavior of the flow around a salient edge as a function of circulation should be carried out. One simple possible way to do this would be to increase the Reynolds number. Unfortunately, the current experimental setup does not allow studying with higher Reynolds numbers, since the model is tested with a free-surface flow and surface waves disturb the flow around the model. By using a rigid surface over the model and by reducing the height of the model above the floor of the test section, studies with higher Reynolds numbers might become possible in future.

CHAPTER 8

SUMMARY AND CONCLUSION

8.1 Introduction

The results obtained during this investigation on the formation of flow separation from a salient edge are important in the context of flows with geometrical singularities and their control. In the following, after summarizing the experimental work, we first resume the physical mechanisms involved in flow separations of this type, and then we give some guidelines and formulate suggestions for future work.

8.2 Summary

Investigation of the flow separation from a rigid wall with salient edge is an interesting subject since the drag characteristics of bodies such as automotive vehicles are highly dependent on the separated wake flows. Studies of Ahmed et al. (1984) have shown that the flow separation from the rear side of a simplified automotive vehicle body is strongly influenced by the rear slant angle.

During this study, after investigation of the previous works on this subject, we started our work by improving the setup to obtain better measurements. The most significant improvement to increase the efficiency of the suction system was improving the suction slit as discussed in chapter 5. Hydrogen bubble measurements were used to validate the improvements on the suction system. Next, we have measured the boundary layer thickness by using hydrogen bubble measurements and compared this thickness with Blasius boundary layer to evaluate the pressure gradient over the upstream plate indirectly. Although Blasius layer was only a first order approximation, the results showed that the pressure gradient over the upstream plate is favorable without creating flow separation. The evaluated pressure gradient is shown in chapter 6. Next, we investigated the flow structure over the rear plate at various slant angles, first qualitatively by using combination of hydrogen bubbles with electrolytic precipitation technique and then quantitatively by using PIV measurements at a Reynolds number of 24800. The results of both qualitative and quantitative measurements showed two types of flow separations: boundary layer separation and inertial separation. This separation phenomenon was explained by using the solution of Falkner-Skan equation. Experiments at a Reynolds number of 50500 by using the combination of hydrogen bubbles with electrolytic precipitation technique at the end of chapter 7 showed that critical angle for separation is dependent on Reynolds number, and it decreases at higher Reynolds numbers.

In the following, physical interpretations of the results are presented.

8.3 Physical mechanisms of flow separation at salient edges

The results with variable slant angle, shown in chapter 7 clearly indicate the existence of two different physical mechanisms which lead to flow separation. First the boundary layer on the rear panel separates under the action of an adverse pressure gradient. The result is a classical boundary layer separation similar to those observed, for example in the adverse pressure gradient region of wing profiles at high incidence. This type of flow separation is only limited to small slant angles. When increasing the slant angle, the flow separates directly from the salient edge tangentially. This kind of separation corresponds to the so-called inertial separation [Batchelor, 1980]. Under similarity conditions with the velocity law of the form, $U_\infty \propto x^m$, the Falkner-Skan equation gives an angle of about 18^o degrees for the occurrence of inertial separation. However, our experiments show that the assumption of similarity is only valid for small slant angles up to separation. They also show in addition the influence of Reynolds number on the critical slant angle for separation.

From a more practical point of view, dependence of the critical angle on Reynolds number and slant angle has important consequences for experimental studies of models in wind and water tunnels. In contrast to models of original scale with higher Reynolds number, the flow on scaled models at lower Reynolds number doesn’t separate, leading to attached flow. As a result, measurements of aerodynamic forces on scaled models must be considered with caution.

In contrast to the Ahmed model, our investigation suppressed the influence of trailing vortices. Since inertial flow separation already appeared at slant angles much lower than 30^o degrees (which is the inertial separation angle found by Ahmed), it is confirmed that the effect of trailing vortices in three dimensional case is to delay inertial separation by attaching the flow to the centerline of the body.

8.4 Suggested improvements and further investigations

During the experiments, we have faced with some problems due to the model. Moreover, some measurements were effected by some short falls of the model. To avoid these difficulties and effects, the model should be improved.

The experimental arrangement used in this study allows to minimize the blockage effects but guarantees at the same time a high degree of flexibility concerning the suction arrangement and the slant angle variations. While as shown in chapter 6, the control of the flow conditions upstream of separation turned out to be quite satisfactory, the control of the flow above the rear panel can be improved in several ways. First to increase the possible Reynolds number range, surface waves should be suppressed by using a rigid cover instead of a free-surface. As shown by the experiments, the maximum slant angle can be reduced to angles, smaller than 25^o since inertial separation appears for smaller angles at all Reynolds numbers we investigated. This would also allow to reduce the height of the model in the test section thus reducing the interference effects with the tunnel wall. A remaining problem which has to be controlled is the occasional formation of flow separation on the free surface above the rear part of hatch panel. Such a separation could be better controlled by suction to avoid flow separation near the free surface.

Mechanically the greatest difficulty was to keep the salient edge as sharp as possible. Due to the properties of the adhesive film, used as the hinge between the two plates, the corner between the two plates becomes rounded in time. To avoid errors due to this, the adhesive film need to be changed very often. Although the hinge functions very successfully when it is first produced, changing the hinge is a very tedious process. A more permanent solution for connecting two plates might avoid time losses due to this problem.

The vertical position of the model inside the test section is also a problem. In section 3.2.2, the effect of image vortices due to channel wall interference was investigated. Although the model is positioned suitably for the current requirements if the geometrical constraints are re-considered, decreasing the height might help to reduce the channel wall interferences. Moreover, reducing the height might reduce as well the effects of free surface such as convection waves due to heat and free surface boundary layer separation.

The main result of this study is evidently the clear distinction put foreward between the flow regimes with classical boundary layer separation and the flow regimes with inertial type of flow separation. To our best knowledge a complete theoretical description of the transition criteria between both types of separation does not exist yet. Our experiments clearly indicate that the influence of the Reynolds number might be an important parameter for this transition. Studies of Stewartson (1970) concerning flow separation at trailing edges showed indeed a Reynolds number dependence of $\alpha_{critical} \sim Re^{-1/4}$. This suggests that application of asymptotic theories might be used to obtain some improved criteria for critical angles at salient edges.

The study also shows that for both types of flow separation very different control strategies should be applied. While for the delay of boundary layer separation devices downstream of the salient edge might lead to efficient control, this is not the case for the inertial type of separation. Appendix B shows some preliminary results with vortex generators fixed upstream of the salient edge which allowed to delay inertial separation. However, the benefit of such arrangement has to be investigated carefully since the complete drag balance should also include the additional drag due to the vortex generators.

REFERENCES

AHMED S. R., Ramm R. & Faltin G. "Same Salient Features of the Time-averaged ground Vehicle Wake", SAE Technical Paper Series 840300, 1984

MOREL T. "The Effect of Base Slant on the Flow Pattern and Drag of Three-Dimensional Bodies with Blunt Ends", Aerodynamic Drag Mechanisms of Bluff Bodies and Road Vehicles Symposium Held at the General Motors Research Laboratories, Plenum Press, 1978

SPOHN A. & Gilliéron P., "Flow Separations Generated by a Simplified Geometry of an Automotive Vehicle", IUTAM Symp. Unsteady Separated Flows, Toulouse, France, 2002

HUCHO W., "Aerodynamics of Road Vehicles", Annual Review of Fluid Mechanics, 1993.25, 1993

LIENHART H., Stoots C. & Becker S. "Flow and Turbulence Structures in the wake of a simplified car model (Ahmed Model)", Proc. DGLR Fach. Symp. Der AG STAB, Stutgart Univ., 2002

GILLIERON P. & Chometon F., "Modelling of stationary three-dimensional separated air flows around an Ahmed reference model. *Proc. Third International Workshop on Vortex, ESAIM*, volume 7, pages 173–182, 1999

McEWAN W. T., "Experimental study of the Influence in Base Slant Variations at the Rear Side of Bluff Bodies", ENSMA/ERASMUS Report, 2001

STUDER G., " Etude des décollements provoqués par des aretes vives", ENSMA D.E.A. Report, 2002

SCHLICHTING H., "Boundary Layer Theory, 6th Edition", Mc-Graw-Hill, 1968

BATCHELOR G. K., "An Introduction to Fluid Mechanics", Cambridge University Press, 1980

COUSTEIX J., “Aerodynamique, Couche Limite Laminaire”, Editions Cepadues,1988

HARTREE D. R., "On an Equation Occuring in Falkner and Skan's Approximate Treatment of the Equations of the Boundary Layer", Proc.Cambr. Phil. Soc. 35, 388-340, 1937

MUNSON B. R., Young D. F., Okiishi T. H. "Fundamentals of Fluid Mechanics", John Wiley and Sons, 1998

POPE A., Barlow J. B., Rae W.H. Jr. "Low-Speed Wind Tunnel Testing", John Wiley and Sons, 1999

KATZ J.& Plotkin A., "Low-Speed Aerodynamics: From Wing Theory to Panel Methods", McGraw-Hill, 1991

UPP, E. L., "Fluid Flow Measurement, "A Practical Guide to Accurate Flow Measurement", Gulf Publishing, 1993

SCHRAUB, F. A., "Use of Hydrogen Bubbles for Quantitative Determination of Time-Dependant Velocity Fields in Low-Speed Water Flows", Journal of Basic Engineering, June 1965

TANEDE S., Honji H. & Tatsuno M., "Some Practical Details of the Electrolytic Precipitation Method of Flow Visualization" Reports of Research Institute for Applied Mechanics Vol. XXVIII, No. 89, 1980

RAFFEL M., Willert C. And Kompenhans J. "Particle Image Velocimetry, A Practical Guide", Springer, 1998

DANTEC Corp., "FlowMap PIV Installation & User's guide, General PIV References"

SPARROW E. M. & LIN S. H., " Flow Development in Hydrodynamic Entrance Region of Tubes and Ducts", The Physics of Fluids, Volume 7, Number 3, 1964

WHITE F. M. "Viscous Fluid Flows", McGraw-Hill, 1974

WEAST R.C., "Handbook of Chemistry and Physics, 49th Edition", The Chemical Rubber Co., 1962

STEWARTSON K., Brown S. N., "Trailing edge stall" Journal of Fluid Mechanics, vol 42, part 3, pp.561-584,1970

PIMPIN A. & Bunyajitradulya A., "On the performance of a straight-walled diffuser with delta-wing vortex generators" Fluid Mechanics Research Laboratory, Chulalongkorn University, 1999

APPENDIX A

Error Estimation

In chapter 4, quantitative measurement techniques such as the hydrogen bubble technique and the PIV method were presented. In this section we discuss possible error sources of these techniques and their effect on the experiments. In the first part, we present a general description of errors associated to velocity measurements. In the following parts, the errors related to the hydrogen bubble and PIV techniques are discussed in more detail.

General Description of Error Estimations for Velocity Measurements

In all velocity measurement techniques used in this study, velocity is found indirectly by dividing particle tracer displacements by a corresponding time interval:

$$\tilde{u} = \frac{distance}{time\ interval} \qquad \textbf{(A.1)}$$

where, $\tilde{u}$ is the average estimate of the x-component of the Eulerian field velocity, taken during a short time interval. However, there is always an uncertainty in the measurements. The uncertainty in a result *R*, can be expressed by

$$R = \frac{W_1}{V_1} + \frac{W_2}{V_2} + \ldots + \frac{W_n}{V_n} \qquad \textbf{(A.2)}$$

where W_1, $W_2 \ldots W_n$ are uncertainty intervals of the variables V_1, $V_2 \ldots V_n$.

Error Estimation in Hydrogen Bubbles Flow Measurement Technique

With the hydrogen bubble technique, the velocity is calculated by dividing the distance between two timelines by the time interval of the bubble generation, as explained in detail in chapter 4.

$$u = \frac{\Delta X}{S} . f \qquad \textbf{(A.3)}$$

Here, ΔX is the x-component of the bubble displacement during the known time interval ΔT deduced from the bubble generation frequency f. S is the scale factor converting displacement ΔX on the image from pixels to [mm].

The uncertainty of u is estimated by using equation A.2, where $u = u(\Delta X, S, f)$. The relative error is:

$$\frac{W_u}{u} = \left(\frac{W_{\Delta X}}{\Delta X}\right) + \left(\frac{W_S}{S}\right) + \left(\frac{W_f}{f}\right) \qquad \textbf{(A.4)}$$

Terms less than one fifth of any other term can be neglected without loss of significance [Schraub, 1965].

We can divide the source of the errors in the x-component of the velocity measurements, in three main groups:

1- Errors, due to pixel resolution:
   - Measurement of ΔX on the image.

2- Errors due to averaging the velocity:
   - Averaging effects of spatially varying velocity field.
   - Time resolution of image acquisition.

3- Errors due to bubbles:
   - Response of the bubbles to velocity fluctuations.

-Resolution problems due to finite bubble size and due to finite averaging intervals.

-Bubble-rise velocity.

-Velocity defect behind bubble-generating wire.

-Possible displacement of the bubble out of the xz-plane of the generating wire at the measurement station.

In what follows, we discuss these error sources independently.

1-Errors due to pixel resolution:

-Measurement uncertainty in ΔX exists as a result of personal errors, optical distortions, image resolution limits, and so on. The digital images required for data recording have a limited image resolution which results in a circle of confusion visible in the picture. The minimum distance that can be measured from a digital image is 1 pixel. This leads to a maximal error of 2 pixels for measured distances. The corresponding average error is:

$$\frac{W_{\Delta X meas}\,(pixels)}{\Delta X\,(pixels)} = \frac{2\,pix}{\Delta X\,(pixels)} = \frac{2\,pix}{u_{local}\,.\Delta T} \qquad \textbf{(A.5)}$$

A longer time interval or a higher local speed reduces uncertainties of this type.

2- Errors due to averaging the velocity*:*

<u>-Resolution power of the image processing:</u> The nominal accuracy of the image analysis is given in terms of the density of the pixels of the digital image and the sampling interval time.

If we denote the resolution power of the image processing by d,

$$d = \frac{L}{n} \qquad \textbf{(A.6)}$$

where n is the number of pixels and L is the actual size of the object to be pictured.

-Averaging uncertainties arise since with marker methods, the Eulerian velocity of the field at a point in time and space $u = u(x,y,z,t)$ is predicted by calculating Lagrangian time-averaged velocity of marker bubbles over a small time interval ΔT.

The error diminishes as ΔT increases and is proportional to $1/u$. Thus, the smaller the measured velocity is the bigger the relative error.

3-Errors due to bubbles:

-Response Uncertainties in ΔX arise since the bubbles do not react instantaneously on changes of the fluid velocity surrounding it. The time constant of such a system, defined by Schraub (1965) is:

$$\tau = \textit{time constant} = d^2/36\nu \qquad \textbf{(A.7)}$$

For a bubble subjected to a steep variation in the surrounding velocity, the bubble essentially attains local velocity in 5τ or ~ 3.5×10^{-4}s. Such small bubble response times are acceptable for low-speed, water-flow studies.

So the error coming from the response time of the bubbles can be neglected for our experiments.

-Resolution uncertainties arise from two sources. Firstly, the method's inability to detect fluctuations whose physical scale is small compared to the distance over which averaging takes place; and secondly, the bubble's inability to respond to fluctuations whose physical scale is small compared to its diameter.

The other factor which limits the observable frequency of fluctuations is the need for long averaging time intervals, in order to obtain more accurate results. Since the velocity is averaged over the time ΔT, fluctuations occurring in smaller times will not be observed even though the bubbles may follow the flow faithfully. For example, with a bubble pulse rate of 50 Hz or framing speed of 50 frames/sec, fluctuations above 50 Hz cannot be detected.

In our experiments, the vortex shedding is around several Hz. Therefore, we can neglect this error.

-Bubble-Rise-Rate Uncertainty: In cases where large velocity gradients exist in the direction of bubble rise, very large errors can be introduced. In this case, a geometry must be chosen in which the bubble rise does not act in the direction of steep velocity gradients.

However, where no such gradients exist, a reasonable criterion for maximum rise rate would be that it is less than about 1/50 of the mean velocity. According to the measured bubble rise rate, discussed in section 4.2.1, it is safe in our experiments to perform measurements, down to 1.7 cm/s velocity.

-Velocity Defect Behind bubble generating wire: The disturbance to the overall flow pattern because of the existence of the bubble-generating wires is very small. However, the local disturbance in the viscous wake of the bubble-generating wire is not negligible. The velocity, just behind the wire is less than the free-stream value owing to the momentum losses associated with the drag on the wire. This velocity defect may be approximated closely in the Reynolds number range from 1 to 5, by the asymptotic laminar-wake solution for an infinite circular cylinder. The defect is not negligible; even at 200 diameters downstream of the wire.

However, the bubble velocity reaches the free-stream velocity in less than 70 wire diameters. A sheet of hydrogen bubbles is seen to be formed around the wire and bubbles are lift off from this sheet apparently by hydrodynamic forces. The existence of this gas film apparently serves to reduce the drag force on the wire and thus reduce the velocity defects.

Data reduction procedures must account for this velocity defect phenomenon; whenever possible bubble displacement should be measured from points greater than 70 wire diameter downstream of the wire.

For the wire that we are using, this 70*d* distance corresponds to 3.5mm. Therefore, for our measurements we used distances greater than 3.5 mm.

-Displacement Uncertainties are those arising from the movement of bubbles out of xy-plane of the generating wire. These movements are caused by the z-component of velocity owing to convection or buoyant forces acting on the bubbles. If these z-displacements occur in a flow with large $\partial u/\partial z$, then errors may be introduced into the estimates of ΔX and u.

For highly two-dimensional experiments, this uncertainty can be neglected. However where the flow becomes three dimensional, significant errors can be expected.

Total Uncertainty in Hydrogen bubble measurements:

After defining all error sources for hydrogen bubble experiments, we can conclude that according to equation A.4, the total error in the measurements for our system is:

$$\frac{\Delta u}{u} = \frac{2d}{l} = 2\frac{L}{n.l} \qquad \textbf{(A.8)}$$

where l is the distance over which the measurements were taken. We don't need to take into account the errors, except for the errors due to the limited pixel resolution.

Error Estimation in PIV measurements:

The overall measurement accuracy in PIV is a combination of a variety of aspects extending from the recording process all the way to the methods of evaluation. The absolute measurement error in the estimation of a single displacement vector ϵ_{tot}, can be decomposed into a group of systematic errors, ϵ_{sys}, and a group of residual errors, $\epsilon_{res.}$

$$\epsilon_{tot} = \epsilon_{sys} + \epsilon_{resid} \qquad \textbf{(A.9)}$$

By choosing a different analysis method or modifying an existing one to suit the specific PIV recording, the systematic errors can be reduced or even removed. The second type of errors, the residual errors remain in the form of a measurement uncertainty even when all systematic errors have been removed. In practice, however, it is not always possible to completely separate the systematic errors, from the residual errors, such that we chose to express the total error as the sum of a bias error and a random error or measurement uncertainty, ϵ_{rms}:

$$\epsilon_{tot} = \epsilon_{bias} + \epsilon_{rms}$$

Each displacement vector is associated with a certain degree of over or under estimation, hence a bias error ϵ_{bias}, and some degree of random error or measurement uncertainty $\pm\ \epsilon_{rms}$.

One of the factors, affecting the measurement uncertainty is the particle image diameter. For the cross-correlation between two images, the optimum image diameter is slightly more than 2.0 pixel [Raffel, 1998].

Another factor is the optimization of particle image shift. For most of the displacements, the uncertainty is nearly constant except for displacements less than 0.5 pixel, where a linear dependency can be observed. This reduction in the measurement uncertainty for displacements, less than 0.5 pixel, may be exploited by offsetting the interrogation windows with respect to each other, according to the mean displacement vector within the interrogation window [Raffel, 1998]

Particle image density also affects the measurement uncertainty. It has two primary effects in the evaluation of PIV images. First, the probability of a valid displacement detection increases when more particle image pairs enter in the correlation calculation. The second effect of the particle image density is that, it can reduce the measurement uncertainty, substantially, which can be explained by the simple fact that more particle image pairs increase the signal strength of the correlation peak. Together the effects described above indicate that if a flow can be densely seeded then both a high valid detection rate as well as a low measurement uncertainty can be achieved using small interrogation windows, which in turn allows for a high spatial resolution [Raffel, 1998].

The image quantization (i.e. bits/pixel) is another source of error, although it has only little influence on the measurement uncertainty or displacement bias error. Increasing the quantization levels more than 4 bits/pixel does not improve the measurements considerably [Raffel, 1998].

Since PIV is based on statistical measurement of the displacement using the correlation between two interrogation windows, a displacement gradient across the window is likely to result in biased data since not all of the particle images present in the first interrogation window will also be present in the second interrogation window, even if the mean particle image displacement is accounted for. For interrogation windows, without an offset, the displacement will be biased to a lower value, since particle images with small displacements will be present more frequently than those with higher displacements [Raffel, 1998].

When PIV method has to be applied in highly three dimensional flows, or cases where the mean flow is normal to the light sheet, uncertainty increase because of the effect of out-of-plane motion. In those cases, out-of-plane loss of pairs is significant such that the correlation peak signal strength diminishes. As a result, the possibility of valid peak detection reduces [Raffel, 1998].

One last factor affecting the uncertainty level is the back-ground noise. Clearly, back-ground noise increases the uncertainty level [Raffel, 1998].

It is clear that specifying all of these errors quantitatively is not possible. The measurement uncertainty and systematic errors in digital PIV evaluation can be assessed in a variety of ways. One approach is to use actual PIV recordings for which the displacement data is known reliably. Although this approach is likely to provide the most realistic estimate for the measurement uncertainty, it only permits a limited study of how specific parameters, such as particle image diameter and background noise, influence the measurement precisions. An alternative approach to assessing the measurement precision in PIV evaluation is based in numerical simulation. The detailed quantitative results of this error analysis can be found in Raffel (1998).

APPENDIX B

Flow control

The possible devices for separation control are classified as active or passive. Active devices use the feedback information from the flow, whereas the passive devices are independent of the flow. Examples for active devices are suction and blowing controlled by a feed-back or feed-forward system, an example for passive devices are vortex generators. The effect of all control devices is to inject kinetic energy upstream of the separation point in order to delay separation. To examine the possibility of flow control by passive control devices, in particular by vortex generators, we performed a simple experiment. The design of the vortex generators is based on the study of Pimpin (1999), concerning the performance of the vortex generators on a straight walled diffuser. Schematic drawing of the vortex generators are given in Figure A.1.

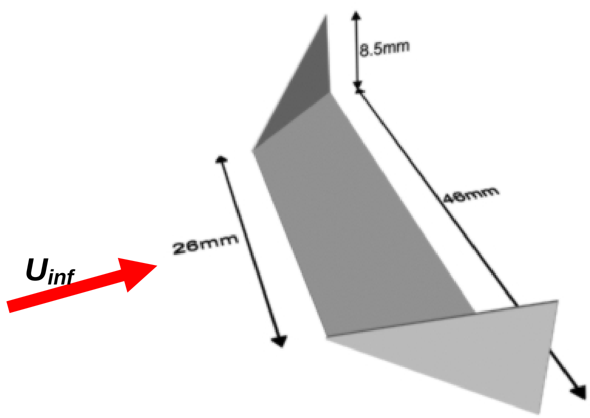

Figure A.1: Vortex generators used for investigation of flow separation.

The effect of five evenly spaced vortex generators, 1cm upstream of the salient edge, on the flow structure downstream of the salient edge is shown in Figure A.2. The base slant angle was 20^o. The PIV measurements are performed from behind in the upstream direction. The measurement plane lies 35 mm downstream of the salient edge. The measurement window is situated in the central part of the model with about 90 mm width.

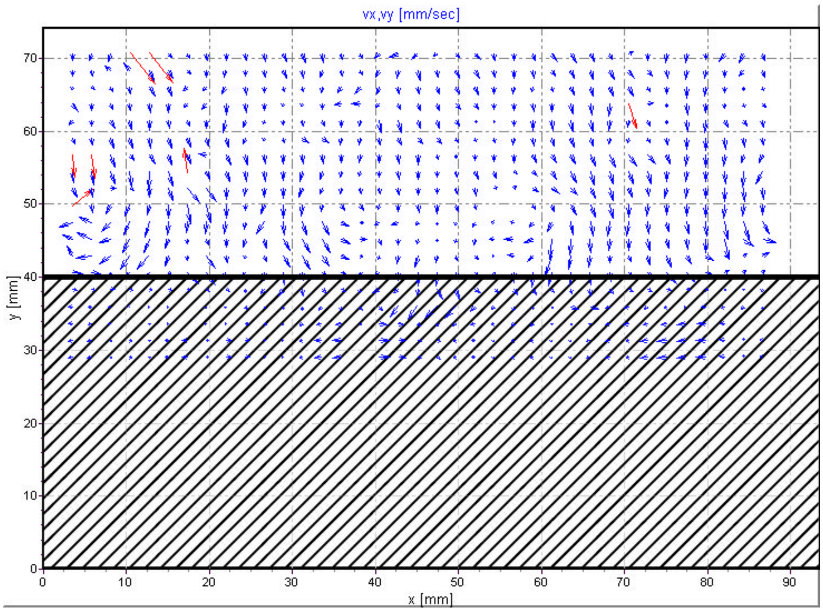

Figure A.2: Effect of vortex generators on flow structure downstream of the salient edge. The measurement plane lies 35 mm downstream of the salient edge with 20^o base slant angle. $U_\infty = 6.4 \pm 0.4$ cm/s. Suction rate is 0.87 ± 0.03 l/s.

The vortices, created by vortex generators are clearly visible in the figure. The vector map shows that the velocity induced along the middle plane of a vortex generator is principally downwards in the direction of the wall. Hence the vortex generators pump kinetic energy towards the wall and thus delay the formation of inertial separation. Figure A.3 shows the downward velocity component at the surface level, 3.5 mm downstream of the salient edge. The centre of the coordinate axis is located in the middle plane of the model at the same level with the upstream panel. Lengths are non-dimensionalized by the span of the model, $b = 450\ mm$ and the velocities are non-dimensionalized by $U_\infty = 6.4 \pm 0.4$ cm/s.

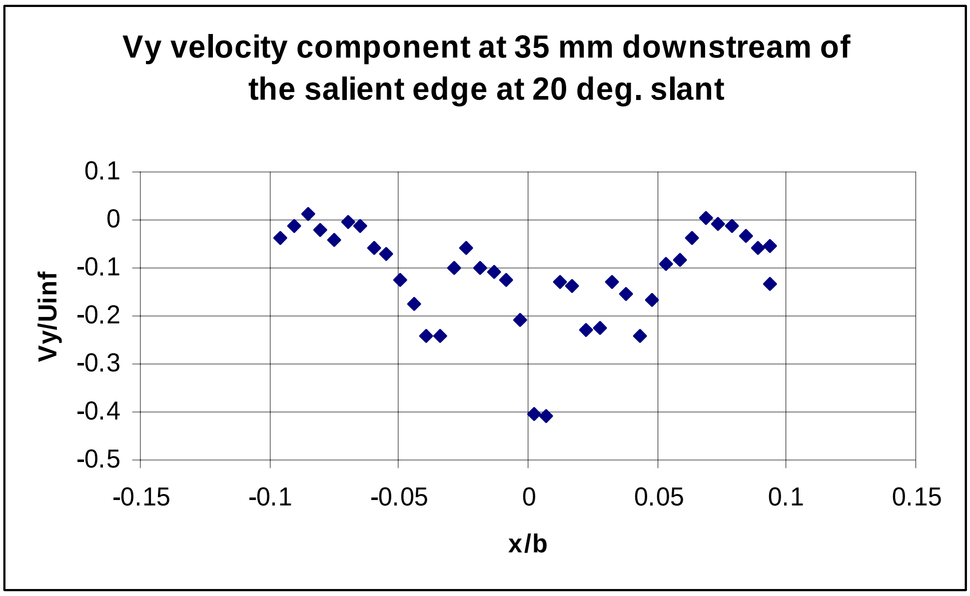

Figure A.3: Vy velocity component at 35 mm. downstream of the salient edge at 20^o of base slant angle. The measurement window is at the middle portion of the model and ~90 mm wide.

Figure A.3 also shows that the vortex generators induce a downward component to the flow, downstream of the salient edge. Without the vortex generators, the inertial separation occurs at this angle for 6.4 ± 0.4 cm/s channel velocity. However, the downward velocity component induced by vortex generators delay the inertial separation.

This result shows that it is possible to develop control strategies for delaying the flow separation from the salient edge. Vortex generators are a simple example for such a passive control.